Hanbury-Brown-Twiss Interferometry Within the UrQMD Transport Approach

Dissertation
zur Erlangung des Doktorgrades
der Naturwissenschaften

vorgelegt beim Fachbereich Physik
der Johann Wolfgang Goethe-Universität
in Frankfurt am Main

von
Gunnar Gräf
aus Frankfurt-Höchst

Frankfurt 2013
D 30

vom Fachbereich Physik der
Johann Wolfgang Goethe-Universität
als Dissertation angenommen.

Dekan: Prof. Dr. Joachim Stroth
Gutachter: Prof. Dr. Marcus Bleicher, Prof. Dr. Carsten Greiner
Datum der Disputation:

Contents

1. Introduction

In physics three different types of forces govern all known interactions. The weakest of these three is the gravitational interaction. Nevertheless, gravitational interaction governs the dynamics on big scales such as planetary sizes and above. The reason for this is that for gravitation there is only one charge carrier, the mass. No "anti-mass" that would lead to repulsive gravitational interactions exists. Thus, there is no such thing as a gravitational neutral massive object. Gravitation is not part of the standard model that describes state of the art particle physics.

The next stronger force is the electroweak interaction. Although it is much stronger than gravitation and, at least the electromagnetic interaction, has infinite range, it usually governs interactions only on small scales, such as the size of molecules. Since there exist positive and negative electric charges, most objects become neutral to a high degree if seen from far away. Nevertheless, the electro-weak force plays an important role in everyday life since it is the electromagnetic interaction between electron shells that makes objects solid or governs nearly all interactions we experience everyday.

The third of the fundamental forces is the strong interaction. Its nature is very different from the other two forces. While its range is in principle infinite it is only relevant on extremely small scales on the size of nucleons. The reason for that is the large coupling of the strong interaction and that the massless gluons that mediate the strong interaction are color-charged themselves. This allows them to interact between each other and leads to a very high potential energy when pulling apart charged particles. If this energy surpasses a certain threshold, new particles are produced in such a way that neutral objects are produced. This process is called string fragmentation or flux tube breakup. There are six possible charges in the strong interaction. They are denoted by three colors and three anticolors. Either three different colors, three different anticolors, or a color and its anticolor combine into a color-neutral object. Since color-charge is a conserved quantum number, only color-neutral objects are produced during the string fragmentation. This behaviour prevents us from observing color-charged objects and is called confinement.

The strong interaction is described by the theory of quantum chromo dynamics (QCD). However, so far it is not possible to solve the equations of QCD. Thus, it is important for the understanding of QCD to probe it experimentally. This proves very challenging. To probe color-charged objects despite confinement, one tries to compress nuclear matter to such densities that the nucleons overlap and quarks and gluons, the color-charged objects of QCD, become the dominant degrees of freedom. Such a state of matter is

named Quark Gluon Plasma (QGP) and is widely believed to have existed shortly after the big bang. Nowadays, it is tried to recreate the QGP in the laboratory. The only means to do so is via the collision of heavy-ions at very high energies. To accelerate the particles to these high energies, particle accelerators are used. The are currently several prominent facilities with different heavy-ion accelerators.

First, the SIS 18 [Agak07, Andr05, Seng93] (Schwerionen Synchrotron) at the GSI (GSI Helmholtzzentrum für Schwerionenforschung GmbH) close to Darmstadt which provides energies up to $E_{lab} = 2$ AGeV. Within the next years the GSI will be expanded to FAIR (Facility for Antiprotons and Ion Research) and will be able to reach up to $E_{lab} = 30$ AGeV at very high interaction rates.

Second, the BNL (Brookhaven National Laboratory) with the AGS (Alternating Gradient Synchrotron) [Ahle00, Elli03, Pink99] that is used as pre-accelerator for RHIC (Relativistic Heavy Ion Collider) [Adam05c, Adco05, Arse05, Back05]. RHIC is able to accelerate ions to center of mass energies of up to $\sqrt{s_{NN}} = 200$ GeV. In the course of the RHIC-BES (RHIC Beam Energy Scan) [Blei11, Cain09, Moha11] that is currently running, it operates at a number of lower energies down to $\sqrt{s} = 7.7$ GeV.

Third, the SPS (Super Proton Synchrotron) [Adam03b, Alt06, Arna06] at CERN (Conseil Européen pour la Recherche Nucléaire) that delivered lead ions up to $E_{lab} = 160$ AGeV and is now operating as pre-accelerator for the LHC (Large Hadron Collider). The LHC provides proton-proton (p+p) collisions at an energy of $\sqrt{s} = 7$ TeV and lead-lead (Pb+Pb) collisions at $\sqrt{s_{NN}} = 2.76$ TeV. So far these are the highest collisions energies ever reached in a particle accelerator experiment. In an upgrade of the LHC it is planned to double these energies in the years to come.

In the study of the strong interaction the QCD equation of state (EOS), quantifying the relationships between intrinsic quantities such as energy density and temperature, is of particular interest. The nature of these relationships depends on the thermodynamic phase. Much may be learned by focusing on the transitions between phases.

In nuclear collisions with center-of-mass energy $\sqrt{s_{NN}} \approx 100$ GeV, there is considerable evidence that the matter passes into a deconfined phase during some part of its evolution [Adam05c, Adco05, Arse05, Back05, Tann06]. Data do not show evidence of a latent heat associated with the transition (e.g. prolonged lifetime [Prat86, Risc96] or zero-pressure mixed phase), and there is general agreement that the transition is a smooth cross-over at $T \approx 150$ MeV and $\mu_B \approx 30$ MeV. Generic considerations [Step04] lead to the expectation that a critical point and first-order phase transition will be found elsewhere – at lower temperatures and larger chemical potentials – on the $T - \mu_B$ plane. Figure 1.1 shows a schematic of the QCD phase diagram [Agga10].

Locating and studying these landmarks on the landscape of the QCD phase diagram would reveal much about the interaction, including fundamental quantities such as la-

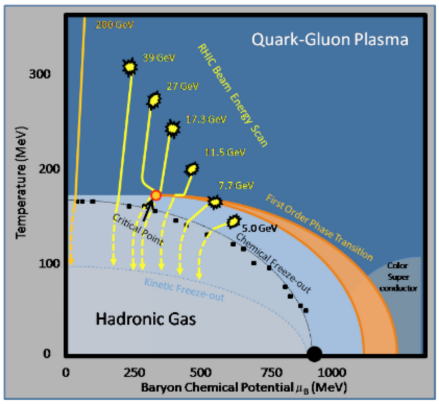

Figure 1.1.: Sketch of the QCD phase diagram in the $T - \mu_B$ plane. An estimate of the critical point and first-order transition line is indicated, as are possible trajectories of systems created in collisions with the indicated center of mass energy. From [Agga10].

tent heats, critical exponents and universality class. Creating a system that samples these more interesting conditions requires lowering the collision energy. For this reason, experiments at RHIC have embarked on a major program to map out the energy dependence of experimental observables, under fixed detector and analysis conditions [Agga10]. Ideally, this exercise parallels that of a condensed matter physicist, precisely controlling the temperature of a material and measuring its resistance, a precipitous drop clearly marking the transition to a superconductor.

However, unlike the condensed matter lab sample, the system created in RHIC collisions is highly dynamic and far from infinite; phase transition signals in heavy-ion collisions will be more subtle. The dynamics of any thermalized bulk system are dictated by its EoS, which encodes the non-trivial landmarks on the phase diagram discussed above. Thus, it is particularly interesting to identify bulk observables sensitive to the dynamics and EoS.

All of the heavy-ion experiments share one common problem. The timescale on the order of 10^{-23} s and the spatial scale on the order of 10^{-15} m prevents all direct observations of the dynamics in heavy-ion collisions. Only the fragments of the collisions can be observed in the detectors of the experiments.

This results in two problems. First, the collision is already over when the observation starts and all parts of the QGP that we want to observe have already recombined into color neutral objects. Second, the only direct observables are energy, charge, momentum and abundance. There is no possibility to directly observe the space-time dynamics of these collisions whatsoever. Fortunately, the second problem can be circumvented to

some degree by using Hanbury-Brown-Twiss (HBT) interferometry. HBT interferometry uses quantum effects to relate two-particle correlations to the space-time structure of the particle emitting source in heavy-ion collisions. Useful though it is, HBT does not allow to disentangle spatial and time dimensions completely. Therefore, it is necessary to employ theoretical models to model heavy-ion collisions and compare their results with experimental observations.

The focus of this thesis is on the exploration of the space-time structure of heavy-ion collisions with the use of HBT correlations. For this purpose, the Ultrarelativistic Quantum Molecular Dynamics (UrQMD) is employed to simulate heavy-ion collisions.

Chapter 2 briefly describes the various types of models that are currently used to describe the results or dynamics of heavy-ion collisions. There is an emphasis put on the UrQMD model since it is used for all the results in this thesis. In chapter 3 a short overview on the theory behind HBT correlations and on the physical interpretation of HBT results is given. The chapters 4-11 present and discuss the results obtained in the context of this thesis.

In chapter 4 (based on [Mitr09]) results for final state charged particle (pseudo-)rapidity distributions in p+$\bar{\text{p}}$/p+p and Pb+Pb/Au+Au at ultra high energies (17.3 GeV $\leq \sqrt{s_{\text{NN}}}$ $\leq$ 14 TeV) from UrQMD are presented. In addition, excitation functions of produced charged particle multiplicities (N_{ch}) and pseudorapidity spectra are investigated up to LHC energies. Good agreement is observed between UrQMD and measured pseudorapidity distributions of charged particles up to the highest Tevatron and Sp$\bar{\text{p}}$S energies.

In chapter 5 (based on [Grae12b]) the dependence of $\pi\pi$ correlations on the charged particle multiplicity and formation time in p+p collisions at $\sqrt{s}$= 7 TeV is explored and compared to present ALICE data. The data allows to constrain the formation time in the string fragmentation to $\tau_f \leq 0.8$ fm/c.

Chapter 6 (based on [Li12]) contains results of two-pion HBT correlations for central Pb-Pb collisions at the LHC energy of $\sqrt{s_{NN}} = 2.76$ TeV. The transverse momentum dependence of the Pratt-Bertsch HBT radii is extracted from a three dimensional Gaussian fit to the correlator in the longitudinal co-moving system (LCMS). Qualitative agreement with the ALICE data is obtained, however R_{out} is overpredicted by nearly 50%. The LHC results are also compared to data from the STAR experiment at RHIC. For both energies we find that the calculated R_{out}/R_{side} ratio is always larger than data, indicating that the emission in the model is less explosive than observed in the data.

In chapter 7 (based on [Grae12a]) the multiplicity scaling of HBT radii in relativistic nuclei and particle interactions is examined. Within UrQMD a large variety of system sizes at different beam energies is studied and the HBT radii are extracted. In the calculation, a good scaling of the radii as a function of charged particle multiplicity is found if the change in multiplicity is caused by a change of centrality at the same energy.

However, the scaling is only approximate when the energy, $\sqrt{s}$, is changed and breaks down when comparing p+p to A+A reactions.

In chapter 8 the isothermal compressibility κ_T of hot and dense matter is explored. κ_T is related to the volume fluctuation in heavy-ion collisions. At LHC energies the multiplicity is high enough to allow an event-by-event HBT analysis for the first time. UrQMD is used to make a prediction of the isothermal compressibility at LHC. Although the value comes with big errors it would still be very valuable to measure it experimentally to constrain at least the order of magnitude of κ_T.

Chapter 9 (based on [Moun11]) deals with non-central heavy-ion collisions that show a tilt in the freeze-out distribution away from the beam axis. The shape and orientation of this distribution are particularly interesting, as they provide a snapshot of the evolving source and reflect the space-time aspect of anisotropic flow. Experimentally, this information is extracted by measuring pion HBT radii as a function of angle with respect to the reaction plane. Existing formulae relating the oscillations of the radii and the freeze-out anisotropy are in principle only valid for Gaussian sources with no collective flow. With UrQMD, which generates flow and non-Gaussian sources, it is found that these formulae approximately reflect the anisotropy of the freeze-out distribution also in this case.

In chapter 10 (based on [Lisa11]) parallels are drawn between the matter evolution in ultra-relativistic heavy-ion collisions, the expansion of ultra-cold atomic gas from a magnetic trap and laser generated micro-explosions in crystals. Shape studies of the created systems are performed in all three cases. The evolution of the system shape depends sensitively on the equation of state of the created matter. Azimuthally sensitive HBT is used to map out the approximate final eccentricity and the tilt of the system when pions decouple at various energies.

In chapter 11 (based on [Grae13]) the substructure of the freeze-out distribution seen in chapter 9 is discussed. It is found that the freeze-out distribution is twisted in such a way that the tilt angle changes from the inside to the outside of the freeze-out zone. The twist is parametrized to quantify it and it is proposed to measure it experimentally via azimuthal sensitive HBT correlations. Additionally, a connection between the twist and the emission of particles from different times during the evolution of the source is established. A systematic comparison between the theoretically observed twist in the freeze-out position distribution and a “quasi experimental” analysis of the model calculations via HBT correlations is shown.

2. Models for heavy-ion collisions

In this chapter various classes of models that are used to describe heavy-ion collisions are presented. They model various degrees of freedom and complexity to describe the dynamics or just the spectra resulting from heavy-ion collisions.

2.1. Thermal models

One of the simplest classes of models compromises the thermal model [Beca02, Brau95, Cley99, Kisi06, Torr05]. The basic assumptions of the thermal model are that the volume in heavy-ion collisions is thermalized and is the same for every particle species. These assumptions allow to describe the system by macroscopic variables, e.g. temperature T and baryochemical potential μ. The fundamental equation for thermal models is the equilibrium phase-space distribution

$$\frac{dN_i}{d^3pd^3x} = \frac{g_i}{(2\pi)^3}\frac{1}{e^{(E_i-\mu_i)/T}+\alpha} \quad . \tag{2.1}$$

g_i is the degeneracy factor and μ_i is the baryochemical potential of particle species i. E is the energy in the system and T is the temperature. α is 1 for the Fermi-Dirac distribution, -1 for the Bose-Einstein distribution and 0 for the Boltzmann distribution. Closely following [Blei05], many observables can be computed analytically in the Boltzmann case.

The transverse momentum distribution can be derived by integrating over the spatial volume and variable transformation.

$$\frac{1}{p_\perp}\frac{d^3N_i}{dp_\perp dy} = \frac{gV}{(2\pi)^2}E_i e^{-(E_i-\mu_i)/T} \tag{2.2}$$

By integrating equation 2.2 over the transverse momentum $p_\perp$ one calculates the rapidity distribution

$$\frac{dN_i}{dy} = \frac{g_i V T^3 e^{\mu_i/T}}{(2\pi)^2}\left(\frac{m_i^2}{T^2}+\frac{m_i}{T}\frac{2}{\cosh y}+\frac{2}{\cosh^2 y}\right)e^{-m_i\cosh y/T} \quad . \tag{2.3}$$

The total number of particles N_i of species i

$$N_i = \frac{g_i V T^3 e^{\mu_i/T}}{2\pi^2}\frac{m_i^2}{T^2}K_2\left(\frac{m_i}{T}\right) \ , \tag{2.4}$$

comes out after integration over y. Here K_2 is the modified Bessel function of the second kind.

It is noteworthy that there is no dynamics included in the thermal model. In principle, it only describes the spectra of a static thermalized medium. These are two idealizations. The medium in heavy-ion collisions is for sure not static and the debate whether it is thermalized or not is still ongoing.

2.2. Blast Wave

A more sophisticated version of the thermal model is the so called blast wave model [Reti04]. The blast wave model incorporates more parameters that enable it to describe a more complex geometry and in addition flow and a finite emission time.
The emission function

$$S(x,K) = m_\perp \cosh(\eta - Y)\Omega(\bar{r})e^{-\frac{(\tau-\tau_0)^2}{2\Delta\tau^2}} \frac{1}{e^{K\cdot u/T} \pm 1} \tag{2.5}$$

of the blast wave model consists of the following parts: $\cosh(\eta - Y)$ describes the distribution of particles in rapidity. $\Omega(\bar{r})$ is a function that describes an ellipse with fuzzy edges that corresponds to the source density distribution in the case of no flow. The gaussian with the exponent $-\frac{(\tau-\tau_0)^2}{2\Delta\tau^2}$ describes the time emission characteristic of the particle-emitting source. The last part describes the probability to emit a particle moving with four momentum K from a source element moving with four-velocity u. In this part, the amount of longitudinal and transverse flow can be parametrized by rewriting $K \cdot u$ in cylindrical coordinates.

The big success of the blast wave model is that it is able to fit the shape of different particle spectra, their elliptic flow v_2 and pion HBT radii simultaneously [Adam05a, Reti04]. This shows that this model captures the essential features at freeze-out without even attempting to describe the dynamics of the collision. For this reason it is valuable as a reference for more fundamental dynamical models.

2.3. Hydrodynamic models

Hydrodynamic models [Hama05, Hira02, Koda01, Kolb03, Paec03, Risc95a, Risc95b, Sche10, Stoe80] provide a dynamic framework to describe heavy-ion collisions. Hydrodynamic models assume a local thermal equilibrium. This allows them to describe the hot and dense medium in terms of macroscopic variables such as temperature, baryochemical potential, and energy density. For this purpose, time and space are subdivided into so-called hydrodynamic cells. The medium within each cell is in equilibrium and is described by its own set of macroscopic quantities. The evolution of these quantities is determined by the hydrodynamic equations of motion. These equations follow directly from the conservation of energy and momentum

$$\partial_\mu T^{\mu\nu} = 0 \ , \tag{2.6}$$

where $T^{\mu\nu}$ is the energy momentum tensor, and the conservation of other quantum numbers

$$\partial_\mu j_i^\mu = 0 \quad . \tag{2.7}$$

The different j_i^μ are the four-currents associated to conserved quantities i, such as baryon number and net strangeness. In ideal hydrodynamics, the energy momentum tensor and the conserved current are defined as

$$T_{ideal}^{\mu\nu} = (\epsilon + p)u^\mu u^\nu - pg^{\mu\nu} \ , \tag{2.8}$$

$$j^\mu = nu^\mu \quad . \tag{2.9}$$

Here ϵ is the energy density, p is the pressure, $g^{\mu\nu}$ the metric tensor, n the density of the corresponding conserved quantity and u^μ are the components of the four-velocity of the hydrodynamic cell.

However equations 2.6-2.9 do not build a closed set of equations. To close the set the so-called equation of state (EoS) is used. The EoS describes the properties of the fluid by describing the relations between the intensive quantities of the thermodynamic system. The nice thing about the EoS is that it is easy to change the properties of the matter by changing the EoS. This allows to probe different states of matter within the same framework.

In recent years also viscous hydrodynamics was studied [Sche11, Song08, Luzu08]. In first-order viscous hydrodynamics a viscous part $S^{\mu\nu}$ is added to the energy momentum tensor

$$T^{\mu\nu} = T_{ideal}^{\mu\nu} + S^{\mu\nu} \quad . \tag{2.10}$$

This leads to the well known Navier-Stokes equations that are, however, known to introduce superluminal signals. Going to the second-order Israel-Stewart formalism [Baie08] resolves this problem. Explaining the elliptical flow at RHIC was one of the big successes of hydrodynamics [Adam05a].

2.4. Microscopic models

Microscopic models, as the name says, describe the microscopic degrees of freedom, e.g. quarks, gluons or hadrons. This is a contrast to thermal models (see sections 2.1 and 2.2) and hydrodynamic models (see section 2.3) that describe only in macroscopic quantities of the medium.

The microscopic models discussed in this section can be divided into two categories. EPOS, HIJING and PYTHIA fall in the category of Glauber-type models. They describe particle production, but do not treat rescattering or medium interactions explicitly, although some might have them included in an effective way, such as parton energy loss in the HIJING model. For nucleus collisions they use the Glauber model to scale up the elementary interactions. All the other models in this section fall in the category

of microscopic transport models. In these models the phase-space information of each individual particle is known through the whole evolution and each individual interaction between particles is described. They differ in the included particle species and in their treatment of interactions. Here is a (incomplete) list with some of the models on the market including a short description of their main features:

- **A**MPT [Lin05] (A Multi-phase transport model)
  - Creates partonic initial state via HIJING [Gyul94].
  - Performs partonic scatterings using Zhang's Parton Cascade [Zhan98].
  - Creates Hadrons via the Lund String Model [Ande83b, Ande83a] or coalescence.
- **B**AMPS [Xu05] (Boltzmann approach of multiparton scatterings)
  - Describes partonic degrees of freedom.
  - Interaction via transition rates.
  - Evolution of Test particles instead of real particles.
  - Treatment of gluon radiation and three-gluon interactions as their back reaction.
- **E**POS [Wern06, Wern07]
  - Multiple Scattering approach with pQCD partonic cross-sections.
  - Scattering partons treated via parton ladders, producing particles close to midrapidity.
  - Phenomenological fragmentation of parton ladders into hadrons.
  - Treatment of remnants as colorless excited off-shell objects producing particles at large rapidities.
- **G**iBUU [Buss12] (The Giessen BUU Project)
  - Boltzmann-Uehling-Uhlenbeck (BUU) framework for energy regimes from 10 MeV to more than 10 GeV.
  - Includes 61 baryonic and 31 mesonic states with properties from [Beri12, Manl92].
  - Propagation of test-particles in mean-fields.
  - Off-shell transport of resonances.
  - Includes the three-body reaction channels $\pi NN \rightarrow NN$ and $NNN \leftrightarrow \Delta NN$.
- **H**IJING [Gyul94] Heavy-Ion Jet INteraction Generator
  - pQCD-inspired minijet model combined together with a Lund-type model for soft interactions.
  - Uses a Glauber-type geometry for pA and AA collisions.

  - Jet quenching modeled by an assumed dE/dz energy loss of partons in matter.
  - Treats nuclear shadowing of parton distribution functions.
  - Hadronization via the Lund String Model [Ande83b, Ande83a].

- **H**SD [Eheh96] (Hadron String dynamics)
  - Contains hadronic and string degrees of freedom.
  - Models collisions via a test-particle approach.
  - Takes into account off-shell properties of hadrons.
  - Treats high energy binary collisions via FRITIOF [Nils87].

- **p**HSD [Cass08] (parton Hadron String dynamics)
  - Includes quarks and gluons with widths and masses defined by the Dynamical Quasi-Particle Model (DQPM) [Cass09].
  - Hadronization of massive off-shell quarks and gluons to off-shell hadrons.
  - Off-shell hadron propagation.

- **P**YTHIA [Sjos06], [Sjos08]
  - Event generator for interactions between elementary particles at high energies.
  - Treats interactions at the parton level.
  - Includes also non Standard Model particles and interactions.
  - Hadronization via the Lund String Model [Ande83b, Ande83a].

- **U**rQMD [Bass98] (Ultrarelativistic Quantum Molecular Dynamics)
  - Hadronic model with extensive resonance dynamics.
  - Particle production via resonance decay, string excitation and fragmentation
  - High energy elementary reactions via PYTHIA [Sjos06].

Since the UrQMD model was used extensively in the research done for this thesis it is described in more detail in section 2.5.

2.5. UrQMD

Ultrarelativistic Quantum Molecular Dynamics (UrQMD) [Bass98, Blei99, Pete08b] is a microscopic transport model that describes heavy-ion collisions. It can be used to model collisions between hadrons or nuclei. During a simulated event UrQMD computes the dynamics over the whole duration of the collision, from the initial state of the nuclei until the final state that could be measured as hadrons in an experimental detector. UrQMD is a Boltzmann approach to heavy-ion collisions, described by the Boltzmann equation

$$\frac{\partial x}{\partial t}\frac{\partial f(x,p)}{\partial x} + \frac{\partial p}{\partial t}\frac{\partial f(x,p)}{\partial p} + \frac{\partial f(x,p)}{\partial t} = I \quad . \tag{2.11}$$

The left side of equation 2.11 describes the change of the phase-space distribution $f(x,p)$ of a specific particle species in momentum, position, and over time. The right side of the equation is often referred to as the interaction term. It contains all kind of gain and loss terms that dictate the rates at which particles described by $f(x,p)$ move backward and forward between different particle species and are redistributed in phase space. Through this interaction term, equations for all particle species are connected. UrQMD does not compute its results by solving the differential equation 2.11. It rather simulates the processes described by it, thus effectively solving the Boltzmann equation. All the particle species included in UrQMD are listed in table 2.1 and table 2.2.

nucleon	**delta**	**lambda**	**sigma**	**xi**	**omega**
N_{938}	Δ_{1232}	Λ_{1116}	Σ_{1192}	Ξ_{1317}	Ω_{1672}
N_{1440}	Δ_{1600}	Λ_{1405}	Σ_{1385}	Ξ_{1530}	
N_{1520}	Δ_{1620}	Λ_{1520}	Σ_{1660}	Ξ_{1690}	
N_{1535}	Δ_{1700}	Λ_{1600}	Σ_{1670}	Ξ_{1820}	
N_{1650}	Δ_{1900}	Λ_{1670}	Σ_{1775}	Ξ_{1950}	
N_{1675}	Δ_{1905}	Λ_{1690}	Σ_{1790}	Ξ_{2025}	
N_{1680}	Δ_{1910}	Λ_{1800}	Σ_{1915}		
N_{1700}	Δ_{1920}	Λ_{1810}	Σ_{1940}		
N_{1710}	Δ_{1930}	Λ_{1820}	Σ_{2030}		
N_{1720}	Δ_{1950}	Λ_{1830}			
N_{1900}		Λ_{1890}			
N_{1990}		Λ_{2100}			
N_{2080}		Λ_{2110}			
N_{2190}					
N_{2200}					
N_{2250}					

Table 2.1.: List of baryon resonances included in the UrQMD model. From the UrQMD manual [UrQM09].

The initial state of two nuclei is given by the distribution of nucleons within these nuclei. Positions of nuclei are randomized according to Wood-Saxon distributions. The initial momenta for each nucleon are composed of a fixed part that is dependent on the collision energy and a part that is randomized according to the Fermi distribution of the nucleons in the nucleus. However, the Fermi momentum is only added once a nucleon interacts. This is called frozen Fermi approximation and avoids that a nucleus dissolves before colliding with the other nucleus.

0^{-+}	1^{--}	0^{++}	1^{++}
π	ρ	a_0	a_1
K	K^*	K_0^*	K_1^*
η	ω	f_0	f_1
η'	ϕ	f_0^*	f_1'
1^{+-}	2^{++}	$(1^{--})^*$	$(1^{--})^{**}$
b_1	a_2	ρ_{1450}	ρ_{1700}
K_1	K_2^*	K_{1410}^*	K_{1680}^*
h_1	f_2	ω_{1420}	ω_{1662}
h_1'	f_2'	ϕ_{1680}	ϕ_{1900}

Table 2.2.: List of mesons included in the UrQMD model. From the UrQMD manual [UrQM09].

After the initialization, all the nucleons are propagated on straight lines until the next interaction. An interaction can be either elastic scattering, resonance decay, soft resonance production or string excitation and fragmentation. All the probabilities for these processes are weighted according to their PDG branching ratios. The criterion for a collision is defined via the geometrical interpretation of the cross-section. A collision happens if

$$\pi d^2 \leq \sigma_{tot} C_{\sigma,tot} \ , \tag{2.12}$$

where d is the distance of closest approach between two particles, σ_{tot} is the total cross-section for a collision to happen between these particles at this energy and $C_{\sigma,tot}$ is the so called cross-section reduction factor. $C_{\sigma,tot}$ is a number between zero and one that turns up for particles produced in string fragmentation (see section 2.5.3 for details).

2.5.1. Cross-sections

The most important ingredient for transport models are the cross-sections. The ideal way would be to get them from experiment. However, most of the elementary cross-sections have not been measured in experiment. For this reason, UrQMD uses other ways to estimate unknown cross-sections. They are determined either from the additive quark model or determined via detailed balance calculations.

Additive quark model The additive quark model is based on the assumption that the hadronic cross-section at high energies is just given by the sum of the quark cross-sections:

$$\sigma_{total} = 40 \left(\frac{2}{3}\right)^{n_M} (1 - 0.4 n_1^s)(1 - 0.4 n_2^s) \text{ m}b \ . \tag{2.13}$$

Here n_M is the number of mesons in the ingoing channel, $\frac{2}{3}$ is the ratio of the number of quarks in mesons to quarks in baryons, n_1^s and n_2^s are the ratios of strange quarks to up and down quarks in particle one and two, and 40 mb is essentially the proton + proton cross-section over a broad energy range. Since the additive quark model is very simple, equation 2.14 is often used to scale the known cross-section σ_{CD} to the unknown cross-section σ_{AB} to achieve better results.

$$\sigma_{AB}(\sqrt{s}) = \sigma_{CD}(\sqrt{s})\frac{\sigma_{AB}^{aqm}}{\sigma_{CD}^{aqm}} \quad . \tag{2.14}$$

σ_{AB}^{aqm} and σ_{CD}^{aqm} are the cross-sections from the additive quark model corresponding to the real σ_{AB} and σ_{CD}

Detailed balance The principle of detailed balance derives from the time-reversal invariance. Meaning that the matrix elements $M_{AB\to CD}$ and $M_{CD\to AB}$ fulfill

$$|M_{AB\to CD}|^2 = |M_{CD\to AB}|^2 \quad . \tag{2.15}$$

The transition probability $P_{A+B\to C+D}$ to go from state AB to state CD is connected to the matrix elements via Fermi's golden rule

$$\frac{dP_{A+B\to C+D}}{dt} = \frac{2\pi}{\hbar}|M_{CD\to AB}|^2 \cdot \rho_{CD} \quad . \tag{2.16}$$

Here ρ_{CD} is the phase-space density of the final state CD in the volume V. At the same time $P_{A+B\to C+D}$ is also defined via the cross-section as

$$\frac{dP_{A+B\to C+D}}{dt} = \frac{\sigma_{A+B\to C+D}\cdot\vec{v}}{V} \ , \tag{2.17}$$

where $\sigma_{A+B\to C+D}\cdot\vec{v}$ is the volume per time unit probed by a particle with cross-section $\sigma_{A+B\to C+D}$. From equations 2.15-2.17 one can derive

$$\sigma_{A+B\to C+D} = \frac{\langle p_{CD}^2\rangle}{\langle p_{AB}^2\rangle}\frac{g_C g_D}{g_A g_B}\sigma_{C+D\to A+B} \quad . \tag{2.18}$$

where g_i are degeneracy factors and $\langle p_{ij}\rangle$ are the mean squared momenta in the center of mass system of the particles. Equation 2.18 allows to calculate the unknown $\sigma_{A+B\to C+D}$ if $\sigma_{C+D\to A+B}$ is known.

2.5.2. String fragmentation

Particles in UrQMD are produced either via soft resonance production, resonance decay or string excitation and fragmentation. Due to the nature of QCD, the energy needed to pull two quarks apart increases with increasing distance of the quarks. At some point, it requires less energy to produce a quark-antiquark or even a diquark-antidiquark pair

than to pull the original partons further apart (see figure 2.1). Due to flavor conservation, only quark-antiquark pairs of the same flavor are produced. The flavor composition of the produced particles is distributed according to a Schwinger-like [Schw51] distribution

$$P(m_\perp) \sim \exp\left(-\frac{\pi m_\perp^2}{\kappa}\right) \quad . \tag{2.19}$$

Here P is the probability to produce a quark pair with transverse mass $m_\perp$. κ is the string tension and has a value of $\kappa \approx 1$ GeV/fm. This leads to a suppression of strange and diquarks since they are more massive than up or down quarks.

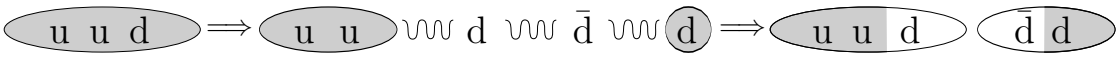

Figure 2.1.: String fragmentation of a neutron like state into a neutron and a π_0. The shaded regions denote leading quarks, the white regions indicate newly produced quarks.

2.5.3. Formation time

After a binary collision, it takes some time for the string to break into quarks and for new hadrons to be formed from these quarks. Since UrQMD has only hadronic degrees of freedom implemented, this behaviour is treated in an effective way via the formation time. Each hadron produced from a string gets assigned a formation time. The formation time in UrQMD is the sum of both processes, i.e. the time for the fragmentation plus the time for the formation of hadrons. During the formation time, the cross-section of the hadrons is reduced by a factor

$$C_{\sigma,tot} = C_{\sigma,tot}^{lead} \frac{n_l}{n_q} \quad , \tag{2.20}$$

where n_q is the number of quarks in the hadron, n_l is the number of leading quarks (quarks that originate from a hadron, not from the string break up) and $C_{\sigma,tot}^{lead}$ is the factor $C_{\sigma,tot}$ of the particle the leading quark stems from. The idea behind equation 2.20 is that partons currently being formed are not allowed to interact and propagating an already reduced $C_{\sigma,tot}$ to a new particle is a probabilistic way to treat the inheritance of unformed quarks to hadrons. Note the special case where n_l is zero. In that case the new hadron is made up only of new quarks and its cross-section is zero during the formation time. This means that it is not allowed to interact at all during that time.

2.6. Hybrid approaches

Hybrid approaches in the sense used here are a combination of hydrodynamic and microscopic transport approaches. There are several good reasons to combine both approaches.

First of all, RHIC data [Adam05c] is described well within hydro models. However, particles and not a fluid are measured in the detectors. Thus, at some point one needs a prescription how to transfer the fluid description into a particle-based description. Usually, a Monte Carlo based implementation of the Cooper-Frye equation [Coop74]

$$E\frac{dN}{d^3p} = \int_\sigma f(x,p)p^\mu d\sigma_\mu \tag{2.21}$$

is used for this transition, where $f(x,p)$ is the boosted particle distribution, p^μ the particle momentum and $d\sigma_\mu$ the particle-emitting hypersurface. This transition is no physical transition in any way. It is only a transition from one description to another description in a technical way. However, there is a reason to change descriptions. In the very early stage the medium is most probably not thermalized, that is why hydrodynamic models that assume thermodynamic equilibrium are not applicable at the very beginning of a collision. Shortly after that, the application of microscopic transport models becomes problematic. It is conceptually difficult to treat more than two particles in the ingoing channel of elementary interactions within such a model. However, the densities become so high that binary collisions alone might not be sufficient to describe the interactions correctly anymore. At this point, hybrid models that use microscopic models for their initial conditions switch to the hydrodynamic description. The hydrodynamic description is assumed to be valid as long as the rate of interactions within the fluid is high. Once the density of the medium becomes low, the description is switched to the particle description again via the Cooper-Frye formalism. In this late stage the particles are evolved via microscopic transport until they decouple and decay in the final state. The beauty of these models is that they include event-by-event fluctuations and a portion of off-equilibrium dynamics and at the same time are able to describe different states of matter, even with phase-transitions, via the used EoS in the hydrodynamic phase. Although hybrid models are a relatively new approach there are already several hybrid models on the market [Hira06, Pete08b, Ryu12].

2.6.1. UrQMD hybrid approach

From version 3.3 on UrQMD, has the capability to do a hybrid, Cascade+Hydro, calculation. This is the hybrid model explained and tested in [Pete08b]. In the initial phase, the particle evolution takes place in the microscopic cascade of UrQMD. Once the two colliding nuclei have passed through each other, the hydrodynamic evolution starts at a time of $t_{start} = 2R/\sqrt{\gamma^2 - 1}$. At this time the spectators continue to propagate in the cascade, while all other particles are mapped to the hydrodynamic grid. Mapping the particles to the hydro grid means they are no longer described as individual particles, but as a medium by their bulk properties. For this, both baryon and energy densities of the particle ensemble are computed and are distributed among the cells of the hydro grid. The particles in UrQMD are point particles. However, their positions are smeared out with a gaussian shape of width 1.5 fm for the mapping. Once on the grid, the evolution is performed by the SHASTA code [Risc95a] in ideal hydrodynamics. For the evolution several EoS are available. Amongst those are a hadron resonance gas EoS [Zsch02] that

reproduces the degrees of freedom present in the cascade of UrQMD, a bag model EoS [Risc95b] with a strong first order phase transition, and the chiral EoS featuring a first order phase transition and a critical endpoint [Stei08]. The space is subdivided into transverse slices of 0.2 fm thickness. Once the energy density in all cells of a transverse slice drops below five times nuclear ground state density, this slice is particlized. This is done via Monte Carlo sampling of the thermal particle distributions as given by equation 2.21. The particles sampled from this procedure are then propagated in the cascade mode of UrQMD until chemical and kinetic freeze-out.

3. Hanbury-Brown-Twiss correlations

The term Hanbury-Brown-Twiss or HBT correlations describes an interferometry technique suggested in 1954 [Hanb54] and first applied in 1956 [Hanb56a, Hanb56b] by Robert Hanbury-Brown and Richard Q. Twiss. They proved that there is an excess of photons from a chaotic light source detected in coincidence if the detectors are nearby and the effect vanishes if the detectors are further apart. It is explained by quantum interference of bosonic particles and the distance of the detectors at which the effect vanishes depends on the angular size of the light source. After they measured that the effect indeed exists, they used it to measure the angular size of Sirius.

Later Goldhaber, Goldhaber, Lee, and Pais (GGLP) [Gold60] could explain the experimental results for angular correlations of pion pairs in proton-antiproton collisions [Gold59] by symmetrizing the wavefunctions of the pions. Their results were dependent on the size of the source they assumed. This opened up the field of HBT analyses in heavy-ion collisions and so far provides the only tool to probe the spatial size and structure of the interaction region. Nevertheless, it is still not possible to fully disentangle the information gained from HBT into a complete space and time picture of the particle-emitting source without the results becoming model dependent.

3.1. The correlation function

To quantify the effect of Bose-Einstein enhancement in heavy-ion collisions one defines the correlation function

$$C(p_1, p_2) = \frac{P_2(p_1, p_2)}{P_1(p_1) P_1(p_2)} \ , \tag{3.1}$$

where $P_1(p_i)$ is the probability to emit a particle with momentum p_i in an event and $P_2(p_i, p_j)$ is the probability to emit both, a particle with momentum p_i and a particle with p_j in the same event. In other words, it is defined as the probability to emit particles with momentum p_1 and p_2 including correlations divided by the same quantity without correlations present.

Since bosons are identical particles, they obey the Bose-Einstein statistics and thus it can be quite tricky to generate a reference sample without quantum interference. The two techniques used in experiment are the opposite-sign method and the mixed-events method. In the opposite-sign method particles with opposite charge are used to construct the reference sample. Since they are obviously not identical particles, they do not exhibit Bose-Einstein enhancement. However, they are subject to the Coulomb force, as

well as same charged particles, but with opposite sign. Depending on the particles and the system, this can have a substantial influence on the correlation function and needs to be corrected for [Lisa05].

Using the mixed-events method circumvents the problem that same sign and opposite sign pairs are influenced differently by Coulomb interactions. In the mixed-events method, the pairs used for the correlation function are formed of same sign particles but from different events. This allows to create a denominator in absence of symmetrization effects. However, it also excludes correlations induced due to energy and momentum conservation [Chaj08]. These will no longer cancel and will show up in the correlation function. While this is not a problem in big systems, it becomes important when observing small systems such as proton-proton or e^+-e^- collisions and is usually corrected for [Abel12].

3.1.1. Correlation function from microscopic models

To connect experiment and theory, one needs to construct the correlation function also from the results of Monte Carlo event generators. However, here the problem is opposite to the problem in experiment. In experiment, it is complicated to generate a particle sample without quantum interference. In theory, it is complicated to create a final state with quantum interference.

The correct way to generate the correlation function would be to have a model that propagates properly anti-/symmetrized wavefunctions and calculates the probability to find particles only at the end of the propagation. And then take the same model without wavefunction symmetrization and create the correlation function from combining these samples. However, there is no transport code in existence that propagates wavefunctions. Usually either particles or test particles are propagated in these models, which is the equivalent of propagating single particle probabilities and not wavefunctions.

The approach taken in theory is to introduce quantum correlations a posteriori. For this, one takes an event generator and generates the four dimensional phase-space distribution of particles without quantum correlations at freeze-out. Then one assumes the freeze-out points of the particles under question are sources of wavefunctions and not particles. These wavefunctions can now be symmetrized for every emitted pair. In principle not only the wavefunction for two particles needs to be symmetrized, but the wavefunction of the whole system. Studies concerning multi-particle symmetrization [Prat93] show that they become important for sources with high phase-space density and enhance the particle occupation at low momentum and broaden the width of the correlation function [Wied99]. Usually, only two-particle symmetrization is used in practice. For two-particle symmetrization, the correlation function has the form

$$C(q,K) = \frac{\int d^4x_1 d^4x_2 S(p_1,x_1) S(p_2,x_2) |\psi_{12}|^2}{\int d^4x_1 d^4x_2 S(p_1,x_1) S(p_2,x_2)} \ , \tag{3.2}$$

where ψ_{12} is the two-particle wavefunction and $S(p_i, x_i)$ are the particle phase-space distributions, taken e.g. from UrQMD. Assuming the particles to be identical bosons and be described by plane waves, as is usually done for pions, one finds

$$C(q, K) = 1 + \langle \cos(\Delta x \cdot q) \rangle_{dist} \ , \tag{3.3}$$

where $\langle \dots \rangle_{dist}$ is the average with respect to the separation distribution, Δx and q are the separation of the particles in four-position and four-momentum space, and $K = \frac{1}{2}(p_1 + p_2)$. Equations 3.3 and 3.5 are the central formulae needed in the theoretical analysis of pion-pion HBT correlations. They are sufficient to go from the freeze-out phase-space distribution through the 3D correlation function to the HBT radii. For more mathematical details, see Appendix A.2.3. In principle, it is no problem to include also coulomb and strong interactions by using other wavefunctions [Lisa05] in equation 3.2. This leads to a different form of equation 3.3.

The exact form of the correlation function depends on the binning and is not necessarily three dimensional. To make the construction of a theoretical correlation function intuitively accessible let us go step by step through the calculation in the case of a freeze-out distribution consisting of N pions. This set of particles can, and in practice usually will, consist of pions from several events. From this set it is possible to generate a number of $N!$ different pairs. For each pair

$$1 + \cos(\Delta t \Delta E - \Delta x \Delta p_x - \Delta y \Delta p_y - \Delta z \Delta p_z) \tag{3.4}$$

is calculated according to equation 3.3. This gives the contribution of the current pion pair to the correlation function. At which point this pair contributes to the correlation function depends on the choice of the coordinate system and on q. The q vector is decomposed into its components and this gives the bin position of the contribution in the correlation function. This procedure is repeated for all possible combinations of pion pairs or until sufficient precision is reached. All the contributions to the correlation function that fall into the same q-bin are averaged.

3.2. Gaussian Source

So far we have only discussed how to get the correlation function. What we are truly interested in is not the correlation function but the time and space structure in the heavy-ion collision. However, it is not possible to extract the whole structure from the correlation function without additional assumptions. The reason for that is the mass-shell constraint (see Appendix A.2.2). The mass-shell constraint arises from the property that the mass difference of the correlated particles is fixed. This effectively reduces the dimension of the correlation function by one compared to the space-time preventing us from retrieving this information.

One of the easier model assumptions to extract the spatial information from the correlation function is to assume a gaussian shape for the particle-emitting source. There

are more involved methods such as source imaging [Brow97, Brow98]. While the large number of parameters extracted from source imaging allows a more detailed description than the gaussian parametrization, it suffers from a need for higher statistics and it is getting harder to get an intuitive picture of the source with increasing number of parameters.

Assuming a gaussian shape for the emission region leads to the form (see Appendix A.2.4)

$$C(q,K) = 1 + \lambda \exp\left(- \sum_{i,j=o,s,l} q_i q_j R_{ij}^2 \right) , \tag{3.5}$$

where λ is the so called chaoticity parameter that decreases with increasing coherence of the particle emission, q_i is component i of q and R_{ij} are the HBT radii. The subscripts o, s and l refer to the different directions in the Out-Side-Long system (see section 3.3) which is often used in the construction of the correlation function.

To extract the R_{ij}^2, equation 3.5 is fitted to the correlation function calculated by equation 3.2. The K dependence indicated in these two equations can be explored by calculation several correlation functions, using only pion pairs within a specific K interval for each function. The different functions are then fitted separately to get the K dependence. The same goes for azimuthal sensitive analyses. In theses analyses, several correlation functions, using only pairs within a specific Φ interval (Φ is the azimuthal angle between impact parameter vector and $\vec{K}$) are are calculated and fitted.

3.3. Out-Side-Long system

When computing the correlation function, there are several possible choices for the coordinate system. One popular choice is the Out-Side-Long system (OSL system) [Prat86, Bert89, Csor90]. The long direction is oriented along the beam axis. The out direction is oriented along the transverse component of the pair momentum and the side direction is oriented perpendicular to these directions (see figure 3.1).

The main difference between individual coordinate system choices is in the interpretation of the resulting parameters. For the OSL system, the interpretation is as follows [Wied99] (see Appendix A.2.5).

$$R_o^2 = \left\langle (\Delta x_o - \beta_o \Delta t)^2 \right\rangle \tag{3.6a}$$
$$R_s^2 = \left\langle \Delta x_s^2 \right\rangle \tag{3.6b}$$
$$R_l^2 = \left\langle (\Delta x_l - \beta_l \Delta t)^2 \right\rangle \tag{3.6c}$$
$$R_{os}^2 = \langle (\Delta x_o - \beta_o \Delta t) \Delta x_s \rangle \tag{3.6d}$$
$$R_{ol}^2 = \langle (\Delta x_o - \beta_o \Delta t)(\Delta x_l - \beta_l \Delta t) \rangle \tag{3.6e}$$
$$R_{sl}^2 = \langle (\Delta x_l - \beta_l \Delta t) \Delta x_s \rangle \tag{3.6f}$$

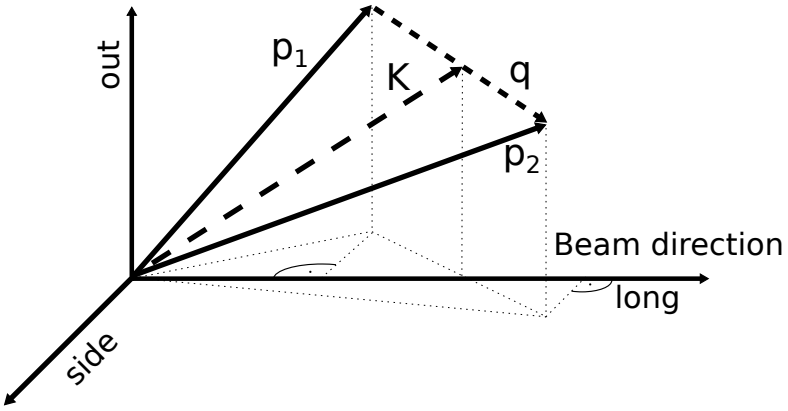

Figure 3.1.: Sketch of the OSL system. The long direction is along the beam axis, the out direction along the pair transverse momentum direction and the side direction is perpendicular to the other directions. (Slightly modified from [Wied99]).

Where the R_{ij} are the HBT radii as obtained from equation 3.5. The Δx_i are the particle separations in the respective direction and the β_i are the components of the pair velocity. Although written as a square, the cross-terms R^2_{os}, R^2_{ol} and R^2_{sl} can be negative. In this form these equations provide only an average source size in the case of non-central collisions since the azimuthal orientation of the out and side directions changes for each pair but the source is not azimuthal symmetric. Only in the case of central collisions is the source symmetric around the beam axis.

Both R_{out} and R_{side} represent the transverse extension of the source. However from equation 3.6a it is obvious that there is also a dependence on the emission duration included in R_{out}. For a more intuitive picture see a sketch of a particle-emitting source in figure 3.2. We are looking down the beam axis. The orange bubble represents the source while the grey dots depict the emitted pion cloud and the blue arrows their momentum. The big black arrows show the measured radii parameters. R_{out} is bigger than the actual transverse size of the source. Due to the finite lifetime of the source, pions produced early have time to travel while the source is still emitting pions. Thus, after all particles are produced, the pion cloud is more extended in the out direction than the actual region emitting pions and the measured region is the extension of the pion cloud. One might wonder why only a spread in the out direction happens and no spread in the side direction. The reason for this is that the HBT parameters are only sensitive to pairs close in momentum. How close, depends a bit on the source size. Pairs close in momentum fly essentially all in the same direction. Thus next to no spread happens in the side direction.

There is a common misconception between the source lifetime and the collision duration in heavy-ion collisions. Δt in equations 3.6a to 3.6f is related to the source lifetime. In case of a Gaussian emission pattern, this would be the width of the Gaussian. On the

other hand, the collision duration is the time the collision takes from the first to the last elementary collision. To make a clear distinction between the two different timespans, let us take a look at several extreme scenarios. Assuming a static source with zero lifetime R_O and R_S are the same. Adding a finite lifetime R_S stays the same while R_O increases with increasing lifetime. The other interesting case is an expanding source. In this case even the radii without and explicit lifetime dependence (see equations 3.6a-3.6f) increase with increasing collision duration. This is due to the implicit time dependence in the Δx_i terms, since the source volume increases over time.

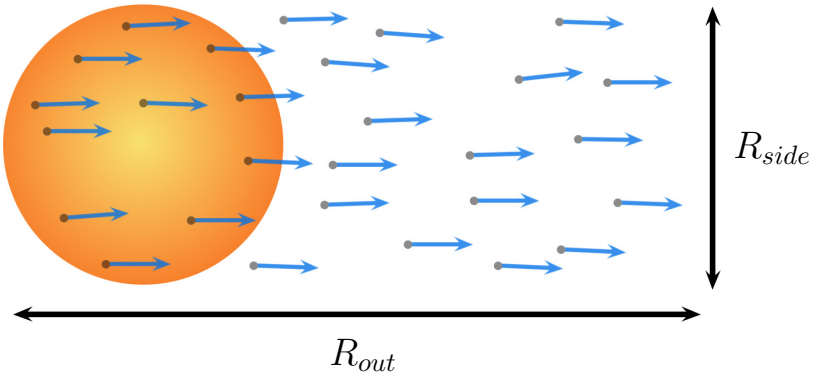

Figure 3.2.: Sketch to illustrate the difference between out and side directions. The sphere is the particle-emitting source, the dots denote the positions of particles and the arrows their momentum.

Another popular choice for the coordinate system that can be combined with the OSL system is the longitudinal comoving system (LCMS). The longitudinal comoving system is the system where the particle pair is at rest in beam direction. So to calculate the correlation function in the LCMS frame one has to Lorentz boost every pair with the respective β_l. The advantage of the LCMS is that equations 3.6a-3.6f simplify as $\beta_l = 0$.

3.4. Region of homogeneity

In the case of expanding sources or in the presence of flow, the HBT radii measure not the extension of the whole source. Rather they probe only a "region of homogeneity" from which particles close in momentum space are emitted [Akke95]. The reason is that the width of the particle-pair separation in space is inversely proportional to the momentum difference probing it. In the presence of flow, for pions to be emitted close in momentum space means they are also likely to be emitted close in position space. The same goes for expanding sources. Turning the argument around, this also means that particles far away in position space are likely to be far apart in momentum space. Thus the region probed by HBT correlations decreases with increasing pair momentum. See figure 3.3 for an intuitive picture.

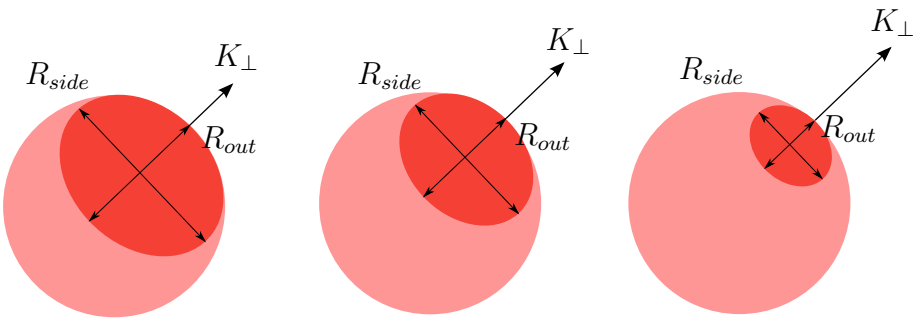

Figure 3.3.: Schematic picture of the region in heavy-ion collisions probed by HBT. The light red region is the particle-emitting region while the dark red region depicts the size of the probed region. Taken from [Nori04].

Due to the reasons above, the decrease of the HBT radii with increasing pair momentum is interpreted as a sign of collective flow in heavy-ion collisions. Thus it is popular to plot the HBT radii versus $K_\perp$. However at high energies a non-flat $K_\perp$ dependence turns up also in proton proton collisions which were believed to be too small to exhibit collective behaviour. For further discussion of collective behaviour in p+p collisions see chapter 5.

3.5. Non-central collisions

In contrast to central collisions, non-central heavy-ion collisions are no longer azimuthally symmetric. Thus the magnitude of the measured HBT radii depends on the measurement angle with respect to the impact parameter vector. The equations 3.6a through 3.6f for central collisions change to the more general case [Fili96, Lisa00c] (see Appendix A.3)

$$\begin{aligned}
R_o^2 &= \frac{1}{2}\left(\langle\Delta x^2\rangle + \langle\Delta y^2\rangle\right) + \frac{1}{2}\left(\langle\Delta y^2\rangle - \langle\Delta x^2\rangle\right)\cos 2\Phi + \beta_o^2\langle\Delta t^2\rangle \\
R_s^2 &= \frac{1}{2}\left(\langle\Delta x^2\rangle + \langle\Delta y^2\rangle\right) + \frac{1}{2}\left(\langle\Delta y^2\rangle - \langle\Delta x^2\rangle\right)\cos 2\Phi \\
R_l^2 &= \langle\Delta z^2\rangle + \beta_l^2\langle\Delta t^2\rangle \\
R_{os}^2 &= \frac{1}{2}\sin 2\Phi\left(\langle\Delta y^2\rangle - \langle\Delta x^2\rangle\right) \\
R_{ol}^2 &= \langle\Delta x\Delta z\rangle\cos\Phi \\
R_{sl}^2 &= -\langle\Delta x\Delta z\rangle\sin\Phi \quad .
\end{aligned} \tag{3.7}$$

Here Φ is the angle between pair momentum vector and impact parameter vector. Note that $\langle\Delta x^2\rangle$, $\langle\Delta y^2\rangle$ and $\langle\Delta z^2\rangle$ are the variances of the source in the impact parameter-fixed frame in contrast to the variances in equations 3.6a-3.6f, which are in the pairwise rotated OSL system.

Equations 3.7 consist of a explicitly Φ dependent part and a Φ independent part. However, this is strictly only true in the case of a non-flowing source. Due to azimuthal momentum anisotropies in a source with flow, Δx, Δy, Δz, and Δt can in principle become implicitly Φ dependent themselves. Thus it is useful to use only low-momentum

pions, for which the implicit Φ dependence is usually small, if a clean measurement of the explicit Φ dependence is important.

3.5.1. Eccentricity

In non-central collisions, the overlap region of two nuclei is elliptic in the plane transverse to the beam axis. This shape is often referred to as almond shape and is connected to two observables, elliptic flow v_2 and the eccentricity ϵ. v_2 is the second Fourier component of the particle momentum distribution and is defined as

$$v_2 = \left\langle \frac{p_x^2 - p_y^2}{p_x^2 + p_y^2} \right\rangle \quad . \tag{3.8}$$

It is a measure for the momentum anisotropy in the transverse plane. v_2 is one of the most discussed observables in the heavy-ion community and bears all kind of information about initial conditions, equation of state, and transport coefficients of the matter created in heavy-ion collisions. Closely related to v_2 is the spatial eccentricity that is defined in a similar fashion as

$$\epsilon = \left\langle \frac{y^2 - x^2}{x^2 + y^2} \right\rangle \ , \tag{3.9}$$

that bears equally rich information about these quantities.

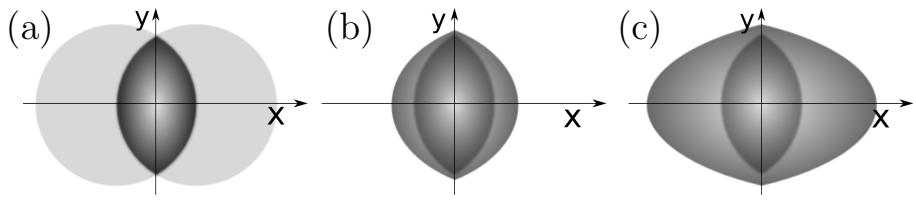

Figure 3.4.: Comic of the time evolution of the eccentricity. (a) Initial almond shape created in the collision of two nuclei. The distribution of colliding matter is extended out of the reaction plane. (b) Early freeze-out or soft expansion. The frozen-out matter (outer, light grey region) is still extended out-of-plane but has become more spherical. (c) Later freeze-out or violent expansion. The frozen-out matter (outer, light grey region) has evolved past a spherical shape and is now in-plane extended.

Due to the presence of positive v_2, the initial shape with a large eccentricity (see figure 3.4a) grows faster in the reaction plane than out of the reaction plane. The initial eccentricity cannot be measured in experiment. It can only be estimated by using a model like the Glauber model [Bial76] or Color Glass Condensate [Geli10]. The final shape depends on how long the system lives and how fast it expands. In the case of a soft equation of state and/or a short lifetime of the system, the particle emitting source is still extended out-of-plane in the final state (see figure 3.4b). For a stiff equation of state and/or a long lifetime, the source becomes spherical or even in-plane extended in

the final state (see figure 3.4c).

Contrary to the initial state eccentricity, the final state eccentricity can be measured in experiment using azimuthally sensitive HBT correlations. The final eccentricity is given by [Reti04] (see Appendix A.3.2)

$$\epsilon = 2\frac{R_{s,2}^2}{R_{s,0}^2} \ , \tag{3.10}$$

where $R_{s,2}$ and $R_{s,0}$ are the second-order and zeroth-order Fourier coefficients of R_s measured in azimuth.

3.5.2. The Tilt

Also related to the freeze-out geometry in non-central collisions is the tilt. If heavy-ions collide in non-central collisions, there are less colliding nucleons in the peripheral regions of the nucleus than in the more central region. Thus there is a momentum asymmetry in the impact parameter direction leading to half the matter moving in positive z-direction and one half in negative z-direction. Over time, the momentum asymmetry turns into a spatial anisotropy. If one assumes an elliptical shape for the emission region, it gets tilted in the x-z plane. This tilt can be characterized by the tilt angle θ_s. It is connected to a tilted Gaussian emission region by

$$f\left(x,y,z\right) \sim \exp\left(-\frac{\left(x\cos\theta_s - z\sin\theta_s\right)^2}{2\sigma_{x'}^2} - \frac{y^2}{2\sigma_y^2} - \frac{\left(x\sin\theta_s + z\cos\theta_s\right)^2}{2\sigma_{z'}^2} - \frac{t^2}{2\sigma_t^2}\right) \ , \tag{3.11}$$

where the prime on the σ_i denotes that these are the widths along the principal axis of the ellipsoid. Figure 3.5 shows a schematic sketch of the tilt angle and the emission geometry.

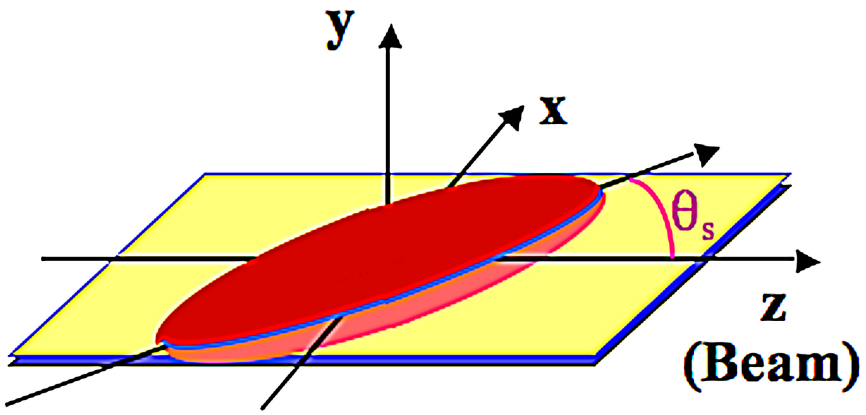

Figure 3.5.: Sketch of the spatial emission geometry tilted by θ_s in the event plane. This kind of geometry is assumed to be present in non-central collisions.

Using azimuthally sensitive HBT, it is possible to measure θ_s [Lisa00c] (Appendix A.3.1) as

$$\theta_s = \frac{1}{2}\tan^{-1}\left(\frac{-4R^2_{sl,1}}{R^2_{l,0} - R^2_{s,0} + 2R^2_{s,2}}\right) , \tag{3.12}$$

where the $R_{i,j}$ are the j-th Fourier component of R_i.

The step by step procedure to extract the Fourier coefficients and then θ_s is as follows. First, the transverse momentum space is subdivided into several sections around the beam-axis. In the case of this thesis always eight 45° wide sections. Second, a correlation function is calculated for each of the sections via equation 3.3 and the R^2_{ij} for each Φ-bin are determined via fits of equation 3.5 to each correlation function. This leads to R^2_{ij} oscillating with Φ. From this the Fourier series in equations A.31 allow to determine the coefficients needed for equation 3.12.

4. Charged Multiplicities from UrQMD

This chapter is based on [Mitr09]. The abundance of charged particles in elementary (anti-)proton-proton collisions and in heavy-ion collisions directly reflects how much of the initial beam energy can be converted to new particles and is therefore directly linked to the stopping mechanism of the initial protons and nucleons.

4.1. pp and $p\bar{p}$ pseudorapidity distributions

Figure 4.1 (a) shows the pseudorapidity distribution of charged particles $dN_{ch}/d\eta$ in inelastic minimum bias p+p collisions from top SPS to top RHIC energies predicted from UrQMD. Figure 4.1 (b) presents measurements performed by the UA1 collaboration [Arni83] for inelastic minimum bias p+$\bar{p}$ collisions at 540 GeV. The closed points show the measured region in η, whereas the open points are the reflected points at $\eta = 0$. With increasing energy the leading hadron effect becomes more visible and from the gap between the humps the strength of the stopping effect is visible. The system is becoming more transparent at higher energies, which is reflected in the change of the pseudorapidity distribution from a Gaussian to a double Gaussian shape [Bjor83, Land53]. The same structure is also visible for the charged particle pseudorapidity distribution in inelastic minimum bias p+$\bar{p}$ collisions at $\sqrt{s} = 53$, 200, 546 and 900 GeV measured by the UA5 collaboration [Alne87] (see figure 4.2 (a)) and the P238 [Harr97] and CDF [Abe90] collaboration in inelastic minimum bias p+$\bar{p}$ collisions at 630 GeV and 1.8 TeV collision energy (see figure 4.2 (b)). A difference is observed between the experiments P238 and CDF at 630 GeV collision energy. At first glance it seems that a discrepancy between the measurements of UA1 and UA5 at 540 GeV and 546 GeV exists. However, in [Arni83] the authors assure the reader that both experiments agree within the error, therefore we refrain from discussing possible reasons for the apparent discrepancies.

The solid lines in figures 4.1 and 4.2 represent calculations from UrQMD in inelastic minimum bias p+$\bar{p}$ collisions. Unfortunately, no measurements of charged particle pseudorapidity distributions were performed for inelastic minimum bias p+p collisions at SPS (17.3 GeV) and RHIC energies to complete the overall picture (note however that pion distributions at SPS and RHIC are well described by the present model [Pete08a]). Comparing UrQMD to the measurements from UA1 (see figure 4.1 (b)) and UA5 (see figure 4.2 (a)), one sees that the model describes the UA1 data on a level of $\approx 20\%$ and the UA5 data within 5% accuracy. Moving to higher energies, UrQMD describes the measured peseudorapidity distribution from P238 at 630 GeV (see figure 4.2 (b)) quite well. Comparing UrQMD to the measurements from CDF at 630 GeV it agrees on a level of $\approx 25\%$. Also here, the reader should notice the difference in the measurements

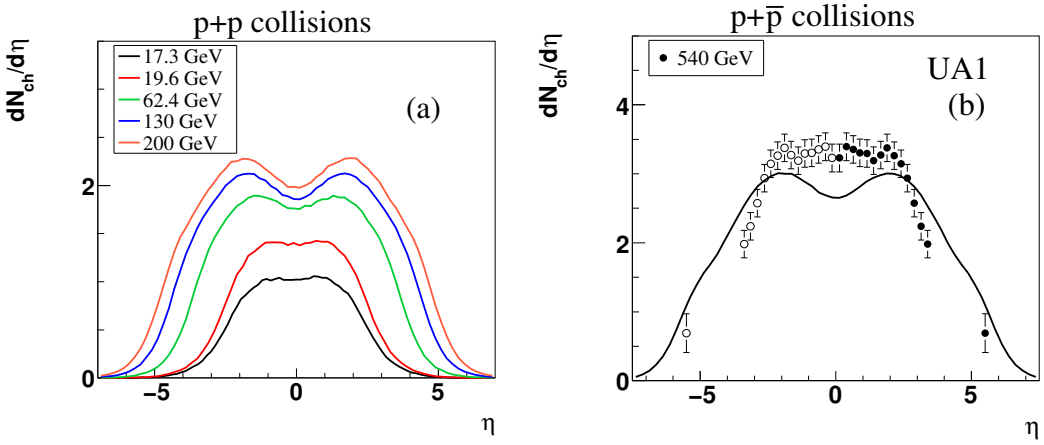

Figure 4.1.: Pseudorapidity distribution of charged particles in inelastic minimum bias p+p collisions from top SPS energies to the highest RHIC energies predicted by UrQMD (a). The pseudorapidity distribution of charged particles in inelastic minimum bias p+$\bar{\text{p}}$ collisions measured by the UA1 collaboration [Arni83] (b). The closed symbols indicate measured points, whereas the open points are reflected with respect to midrapidity. The solid line represents calculations from UrQMD, in inelastic minimum bias p+$\bar{\text{p}}$.

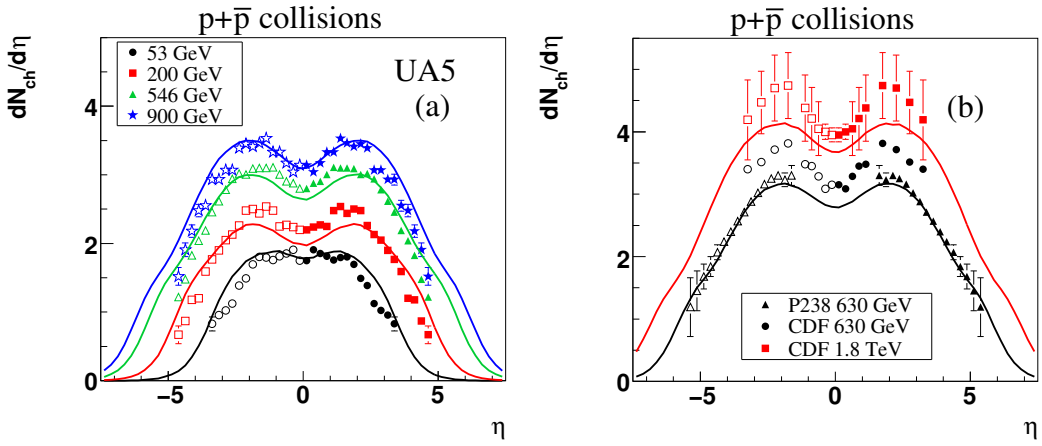

Figure 4.2.: Pseudorapidity distribution of charged particles in inelastic minimum bias p+$\bar{\text{p}}$ collisions for different energies measured by the UA5 [Alne87] (a), CDF [Abe90] and P238 [Harr97] (b). The closed symbols indicate measured points, whereas the open points are reflected with respect to midrapidity. The solid line represent calculations from UrQMD, in inelastic minimum bias p+$\bar{\text{p}}$.

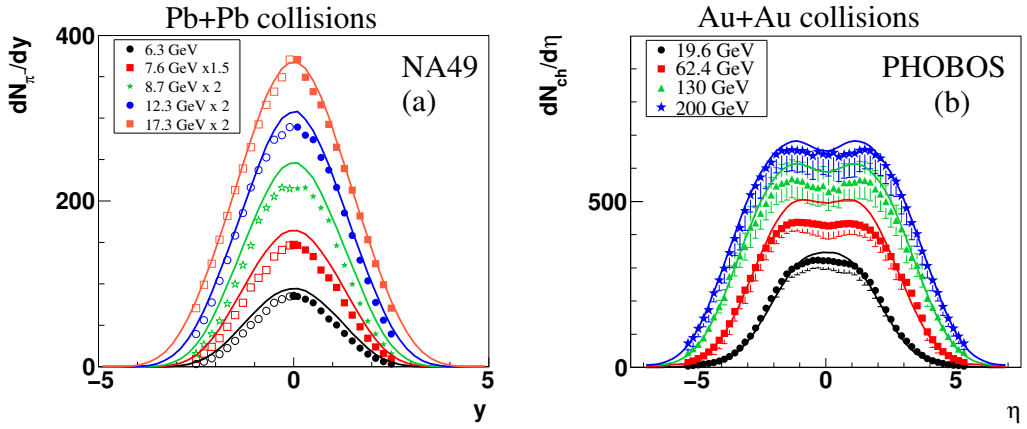

Figure 4.3.: (a): Rapidity distribution of π^- in Pb+Pb collisions at SPS energies from $\sqrt{s_{NN}}$ = 6.3 to 17.3 GeV (7% most central collisions for $\sqrt{s_{NN}}$ = 6.3 - 12.3 GeV, 5% most central collisions for $\sqrt{s_{NN}}$ = 17.3 GeV) measured by the NA49 collaboration [Afan02, Alt08b]. (b): The pseudorapidity distribution of charged particles in Au+Au collisions (6% most central collisions, $b \leq 3.55$ fm for the data from $\sqrt{s_{NN}}$ = 19.6 - 130 GeV and $b \leq 3.65$ fm for the $\sqrt{s_{NN}}$ = 200 GeV dataset) at RHIC energies from $\sqrt{s_{NN}}$ = 19.6 to 200 GeV performed by the PHOBOS collaboration [Abre02, Alve09, Back06a, Back03a]. The solid line represent calculations from UrQMD ($b \leq 3.9$ fm for 7% most central Pb+Pb collisions from $\sqrt{s_{NN}}$ = 6.3 - 12.3 GeV, $b \leq 3.4$ fm for 5% most central Pb+Pb collisions at $\sqrt{s_{NN}}$ = 17.3 GeV, $b \leq 3.6$ fm for 6% most central Au+Au collisions from $\sqrt{s_{NN}}$ = 19.6 - 130 GeV and $b \leq 3.7$ fm for 6% most central Au+Au collisions at $\sqrt{s_{NN}}$ = 200 GeV).

between P238 and CDF at 630 GeV. For the measurements at 1.8 TeV, the deviation is on the level of less than 10 %.

4.2. Nucleus-Nucleus rapidity distributions

Moving on to nucleus-nucleus reactions, figure 4.3 shows the dN_{π^-}/dy and $dN_{ch}/d\eta$ distribution in Pb+Pb and Au+Au collisions for different experiments and energies from SPS to RHIC energies. Figure 4.3 (a) presents the dN/dy distribution of negatively charged pions measured by the NA49 collaboration [Afan02, Alt08b] from $\sqrt{s_{NN}}$ = 6.3 to 17.3 GeV (7% most central collisions for $\sqrt{s_{NN}}$ = 6.3 - 12.3 GeV, 5% most central collisions for $\sqrt{s_{NN}}$ = 17.3 GeV). It is visible that UrQMD overpredicts the measurements at midrapidity by $\approx$ 5% except for the ones at 17.3 GeV collision energy. Going to the higher RHIC energies (figure 4.3 (b)) we compare to the measurements from the PHOBOS collaboration [Alve09, Back06a, Back03a]. It is visible that the multi-

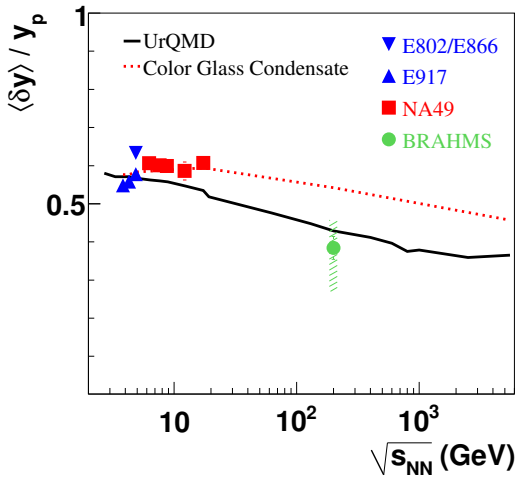

Figure 4.4.: Relative rapidity shift $\langle \delta y \rangle / y_p$ as a function of the center-of-mass energy in relativistic heavy-ion collisions from AGS to RHIC energies [Vide95, Back01, Appe99, Bear04, Blum07]. The black line represents the prediction made by UrQMD from low AGS to LHC energies. The dotted line represents calculations from a color glass condensate model [Meht09].

plicity increases with collision energy from $\sqrt{s_{NN}} = 19.6$ to 200 GeV (6% most central collisions). Furthermore the shape of the spectra is also changing as already seen for p+p collisions due to the fact that the colliding nuclei become increasingly transparent [Bjor83, Land53]. This is reflected in the UrQMD prediction where the shape of the spectra is also changing with energy. UrQMD slightly (20%) overpredicts the measurements around midrapidity at $\sqrt{s_{NN}} = 62.4$ GeV and 130 GeV.

A crucial point for particle production in A+A reactions is how much of the initial longitudinal motion is transformed to particles and transverse expansion. This is best characterized by an investigation of the energy (rapidity) loss of the initial nucleons. New measurements at SPS energies (20 - 80 AGeV) [Blum07] combined with previously published results from AGS to RHIC energies [Vide95, Back01, Appe99, Bear04] are available to test the predictions performed by the UrQMD model. Figure 4.4 depicts the energy evolution of the relative rapidity loss of the incoming nucleons in Au+Au/Pb+Pb reactions up to LHC energies. The net-baryon distribution ($\mathrm{d}N_{B-\bar{B}}/\mathrm{d}y$) is made by using the calculated rapidity spectra for p, $\bar{p}$, n, $\bar{n}$, Λ, $\Sigma^{\pm}$, Σ^0, Ξ^-, Ξ^0 and Ω^- and their anti-particles respectively. From the net-baryon distribution an average rapidity shift $\langle \delta y \rangle$ can be calculated as follows:

$$\langle \delta y \rangle = y_p - \frac{2}{\langle N_{\mathrm{part}} \rangle} \int_0^{\infty} y \frac{dN_{B-\bar{B}}}{dy} dy, \tag{4.1}$$

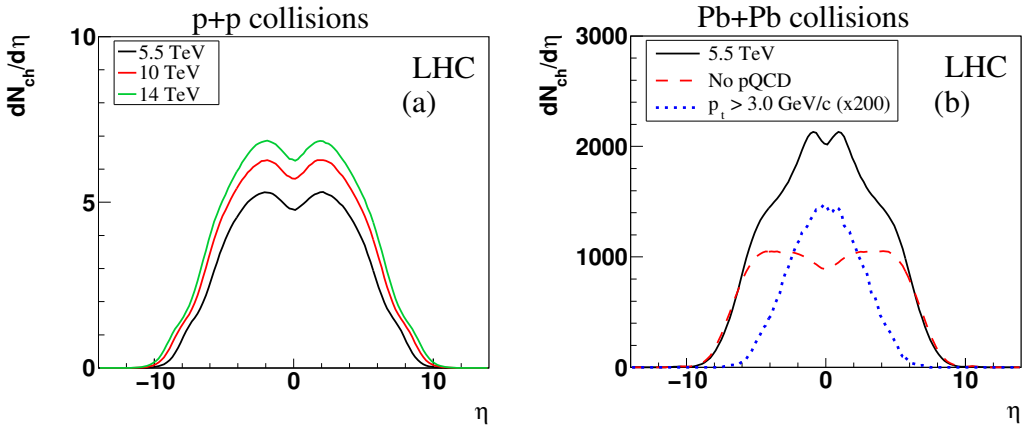

Figure 4.5.: Prediction of the charged multiplicity pseudorapidity distribution for inelastic minimum bias p+p collisions from $\sqrt{s_{\mathrm{NN}}} = 5.5$ to 14 TeV (a) and Pb+Pb collisions (5% most central collisions, $b \leq 3.35$ fm) at 5.5 TeV (b) collision energy from UrQMD, with PYTHIA (solid line), without pQCD contributions (PYTHIA) (dashed line) and for hard produced particles (dotted line) ($b \leq 3.4$ fm for 5% most central Pb+Pb collisions at 5.5 TeV).

where y_p is the projectile rapidity and $\langle N_{\mathrm{part}} \rangle$ the number of participating nucleons. It is clearly visible in the data that $\langle \delta y \rangle / y_p$ decreases from approximately 0.6 at AGS energies to 0.4 at top RHIC energies which indicates that the relative baryon stopping is slightly weaker at RHIC energies as compared to lower AGS and SPS energies. The same trend is also observed in UrQMD (black line in figure 4.4) where the absolute stopping follows the trend going from AGS to LHC energies. Another approach is also shown in figure 4.4 from a color glass condensate model [Meht09] (dotted line). In this model the authors are using the rapidity distribution of net protons ($p - \bar{p}$) in central heavy-ion collisions as a testing ground for saturation physics and that the valance quark parton distribution is well known at large x, which corresponds to the forward and backward rapidity region.

From these studies of the energy deposition (stopping) and particle production, we conclude that UrQMD has a valid basis for further extrapolations in energy and allows us to make predictions for LHC energies.

4.3. UrQMD at LHC energies

The predictions for the charged particle pseudorapidity distributions at LHC energies are shown in figure 4.5 (a) for inelastic minimum bias p+p collisions at $\sqrt{s} = 5.5$, 10 and 14 TeV and for the 5% most central ($\langle N_{\mathrm{part}} \rangle = 383$) Pb+Pb collisions at $\sqrt{s} = 5.5$ TeV (b) (solid line).

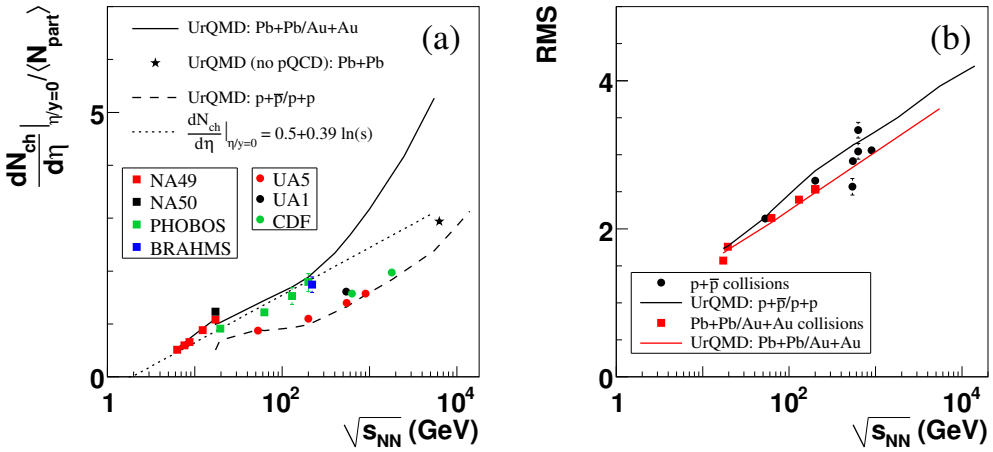

Figure 4.6.: (a): The energy dependence of the number of charged particles ($\frac{dN_{\mathrm{ch}}}{d\eta}$) at midrapidity divided by N_{part} for p+$\bar{\mathrm{p}}$ (circles) and Pb+Pb/Au+Au (squares) collisions. (b): RMS width of the pseudorapidity rapidity distributions as a function of the center-of-mass energy. The black solid line represents calculations from UrQMD for p+$\bar{\mathrm{p}}$/p+p and the red solid line for Pb+Pb/Au+Au collisions respectively.

There are two complementary particle production mechanisms at LHC energies: hard parton-parton scattering and soft processes. Particles produced in hard scatterings are usually created in primary collisions and are centered in a narrow region around midrapidity (seen in dotted line in figure 4.5 (b)), whereas softly produced particles are distributed over the full pseudorapidity range (see dashed line in figure 4.5 (b)). At LHC energies both mechanisms play an important role so that the pseudorapidity distribution of charged particles shown in figure 4.5 (b) (solid line) is the sum of both processes.

Figure 4.6 (a) shows the measured number of charged particles at midrapidity ($\frac{dN_{\mathrm{ch}}}{d\eta}|_{\eta=y=0}$) as a function of $\sqrt{s_{NN}}$ for p+$\bar{\mathrm{p}}$ (circles) [Arni83, Alne87, Abe90] and Pb+Pb/Au+Au (squares) [Afan02, Alt08b, Abre02, Alve09, Back03a, Back06a, Bear02] collisions [1]. It is clearly visible that in A+A collisions N_{ch} scales linearly with the center-of-mass energy. The difference in scaling with N_{part} between p+$\bar{\mathrm{p}}$/p+p and Pb+Pb/Au+Au collisions increases with increasing center-of-mass energy. A simple approach to extrapolate the number of charged particles in Pb+Pb collisions was suggested in [Abre08] by using a fit function ($\frac{dN_{\mathrm{ch}}}{d\eta}|_{\eta/y=0} = 0.5+0.39\cdot\ln(s)$). One can see that the fit function and UrQMD agree until top RHIC energies. At higher energies UrQMD predicts a higher multiplicity in central Pb+Pb collisions as compared to the simple extrapolation, especially for top LHC energies. The reason for the increasing multiplicity is the increase of hard collisions at LHC energies. When not taking hard collisions into account (see figure 4.6 (a))

[1] Note that the number of charged particles for NA49 is calculated by adding the midrapidity yields of π^-, π^+, K^- and K^+.

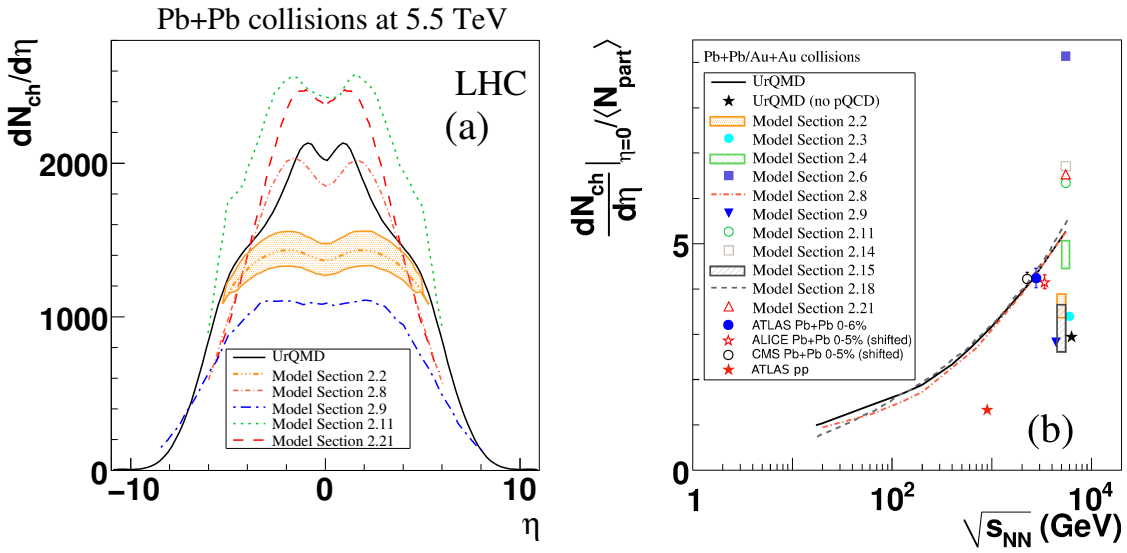

Figure 4.7.: Comparison of the predicted pseudorapidity distribution of charged particles (a) and the charged particle multiplicity at midrapidity (b) from UrQMD, predictions from various other models [Abre08], and data [Aad10, Aad12].

by switching off PYTHIA and just allowing UrQMD to have soft particle production, UrQMD would follow the simple linear fit function. If the LHC data fall on the dotted line, hard collisions are either absent at LHC or saturation effects do effectively suppress a large part of the particle production. UrQMD not only describes the multiplicity and trend in p+$\bar{\text{p}}$/p+p collisions (dashed line) but also in Pb+Pb/Au+Au collision (solid line). Furthermore in UrQMD, if going to LHC energies, the difference between p+p and Pb+Pb collisions becomes larger. The RMS-width [2] is calculated by fitting the measured pseudorapidity distribution of charged particles from UA1, UA5, P238 and CDF experiments for p+$\bar{\text{p}}$ NA50 and PHOBOS for Pb+Pb/AuAu collisions by a double Gaussian [3] (see figure 4.6 (b)). An increase of the RMS-width with the center-of-mass energy is observed for p+$\bar{\text{p}}$ and Pb+Pb/Au+Au collisions. The dependence is linear for p+$\bar{\text{p}}$ and Pb+Pb/Au+Au collisions. In the data, no difference between the RMS-width in p+$\bar{\text{p}}$ and Pb+Pb/Au+Au is seen. UrQMD shows a slight difference between the RMS-width for p+$\bar{\text{p}}$ and Pb+Pb/Au+Au collisions.

To get an overall picture how the presented prediction of UrQMD compares to other approaches, figure 4.7 depicts the compiled results from other model predictions. Fig-

[2] RMS $= \sqrt{\eta_0^2 + \sigma^2}$

[3] Where double Gaussian means that we parametrized the pseudorapidity distribution by the sum of two Gauss distributions placed symmetrically with respect to midrapidity and defined as follows: $\mathrm{dN/d}\eta = \mathrm{N}\ (e^{-\frac{(\eta-\eta_0)^2}{2\sigma^2}} + e^{-\frac{(\eta+\eta_0)^2}{2\sigma^2}})$, where η_0 is the shift from zero and σ^2 the variance of the distribution.

ure 4.7 (a) shows the predicted pseudorapidity distributions of charged particles from various models [Abre08] in comparison to UrQMD. All transport models (hadronic or partonic), including UrQMD, can be put together in one group by predicting a similar shape and multiplicity. The second group are saturation models which in general predict a lower multiplicity (also seen in [Arme00]). This is also visible in figure 4.7 (b) where the energy dependence of predicted charged particle multiplicity at midrapidity is shown. At first glance it seems that the data would rather follow the trend of a straight line, but the major part of the models including UrQMD do not favour this trend (also seen in [Sark06]).

5. Formation time via HBT from pp collisions at LHC

This chapter is based on [Grae12b]. With the start of the LHC physics program a tremendous amount of new data became available. Apart from the heavy-ion data, the proton-proton (pp) program allowed to explore collective features of the strong interaction in high multiplicity pp events.

It seems, same as in massive nucleus-nucleus collisions, a strongly interacting medium is created even in pp collisions that exhibits bulk properties similar to those found in heavy-ion collisions, such as space-momentum correlations and collective behaviour [Liu11b, Liu11a, Voge11, Wern11a]. The details of these correlations can be probed using Hanbury-Brown-Twiss (HBT) [Hanb56b] interferometry. While it is often argued that the particle-emitting system in p+p collisions is too small to create a medium that exhibits bulk properties, this is different at a center of mass energy of $\sqrt{s}$= 7 TeV [Wern11b]. Here, the particle multiplicity is about the same as in nucleus-nucleus collisions, studied at the Relativistic Heavy Ion Collider (RHIC) in Brookhaven. For previous studies of femtoscopic correlations in p+p collisions at RHIC and Tevatron see [Agga11, Alex93]. This data suggests that space-momentum correlations are developed even in pp collisions as soon as high particle multiplicities are achieved. Thus, it is worthwhile studying the dependence of HBT observables on the event multiplicity. As the system created in p+p collisions at LHC is still small, an essential quantity that influences the particle freeze-out radii is the formation time in flux tube fragmentation. Without going into the details of the specific implementation, it is clear that the formation time sets the scale for a minimum value of the source lifetime – of course followed by resonance decay and rescattering. We use recent LHC data on pp collisions to determine the formation time in the flux tube break-up. Results for Pb+Pb reactions and scaling studies at the LHC within the same model can be found in [Li12, Grae12a] and chapters 6 and 7.

5.1. Particle formation time

The formation time denotes the time it takes for a hadron to be produced from a fragmenting string (see also section 2.5.3). A very common model to describe such a flux tube fragmentation is the Lund string model [Ande83a]. In the Lund model the formation time consists of the time it takes to produce a quark-antiquark pair and the time it takes for that pair to form a hadron. For the Lund model both of these times are proportional to the transverse mass of the created hadron and inversely proportional to the

string tension. For simplicity, UrQMD uses a constant formation time of $\tau_f = 0.8$ fm/c for hard collisions. Only after the formation time, particles, e.g. ρ-mesons, can decay or perform subsequent scatterings with their full cross-section. During their formation time leading hadrons are allowed to interact with a reduced cross-section. Hadrons without leading quarks are not allowed to interact at all during their formation time. While a Heaviside function like behaviour of the cross-section is implemented in UrQMD, there are other model studies [Spie99, Gall08] that investigate the influence of several scenarios of continuous changes from zero to full cross-section during the formation time. The freeze-out space-time positions of hadrons are defined as either their point of formation or the point of last interaction, whatever occurs later in time. Since HBT probes the freeze-out distribution, the extracted radii are sensitive on the value of τ_f in small systems at high collision energies where the majority of particles is produced from flux tube fragmentation. Although there are many theoretical studies on the formation time [Cass04, Arle03, Kope07, Falt04, Bial99], few of them allow to put constraints on τ_f or the behaviour of the cross-section growth from experimental data.

5.2. Analysis in charged multiplicity classes

UrQMD (v3.3p1) is used to generate the freeze-out distributions of particles in proton-proton collisions at $\sqrt{s}$= 7 TeV. UrQMD is described in more detail in [Bass98, Pete08b, Li09a] and section 2.5. After the simulation run, a correlation afterburner using the basic equation 3.3 is applied to calculate the corresponding 3D correlation function C(q). In this analysis, as in ALICE data, particles within a pseudorapidity interval of $|\eta| < 1.2$ are taken into account. The analysis is done differentially for $K_\perp$-bins of 100 MeV (see section 3.4) in the region of $K_\perp = 0.1 - 1.0$ GeV and also for the different event multiplicities listed in table 5.1. Generally the average $dN_{ch}/d\eta$ from UrQMD is 15% smaller than the one measured by the ALICE collaboration, in the same charged multiplicity classes, because we did not employ specific PYTHIA tunes for the present analysis. All the correlation functions are computed for pairs in the longitudinal comoving system (LCMS). The HBT radii are extracted by fitting the gaussian shape of equation 3.5 to the 3-dimensional correlation functions over a range of $|q_i| < 800$ MeV.

5.3. Comparison to data

In this section the results on HBT radii from the UrQMD model are compared to ALICE data [Aamo11a]. In figure 5.1 the projections in out, side and long direction of the 3D correlation function together with a projection of the fit for $K_\perp$=0.3-0.4 GeV and $N_{charged}^{|\eta|<1.2}$= 23-29 are shown as an example. It can be seen that the calculated correlation function (shown as dots) is well-described by a Gaussian fit (lines). However, oscillations of the correlation function are present at larger q. This indicates that there is a non-gaussian component in the underlying separation distribution of the pion freeze-out points.

$N_{charged}^{\lvert\eta\rvert<1.2}$	UrQMD $\langle dN_{ch}/d\eta\rangle_{\lvert\eta\rvert<1.2}$	ALICE $\langle dN_{ch}/d\eta\rangle_{\lvert\eta\rvert<1.2}$
1-11	2.52	3.2
12-16	5.74	7.4
17-22	8.01	10.4
23-29	10.72	13.6
30-36	13.65	17.1
37-44	16.74	20.2
45-57	20.94	24.2
58-149	27.57	31.1

Table 5.1.: Table of the investigated multiplicity intervals. The first column shows the interval boundaries, the second column the mean charged particle multiplicity per unit of pseudorapidity ($dN_{ch}/d\eta$) from events with at least one charged particle in $|\eta| < 1.2$ from UrQMD. The third column shows the same quantity from ALICE data [Aamo11a].

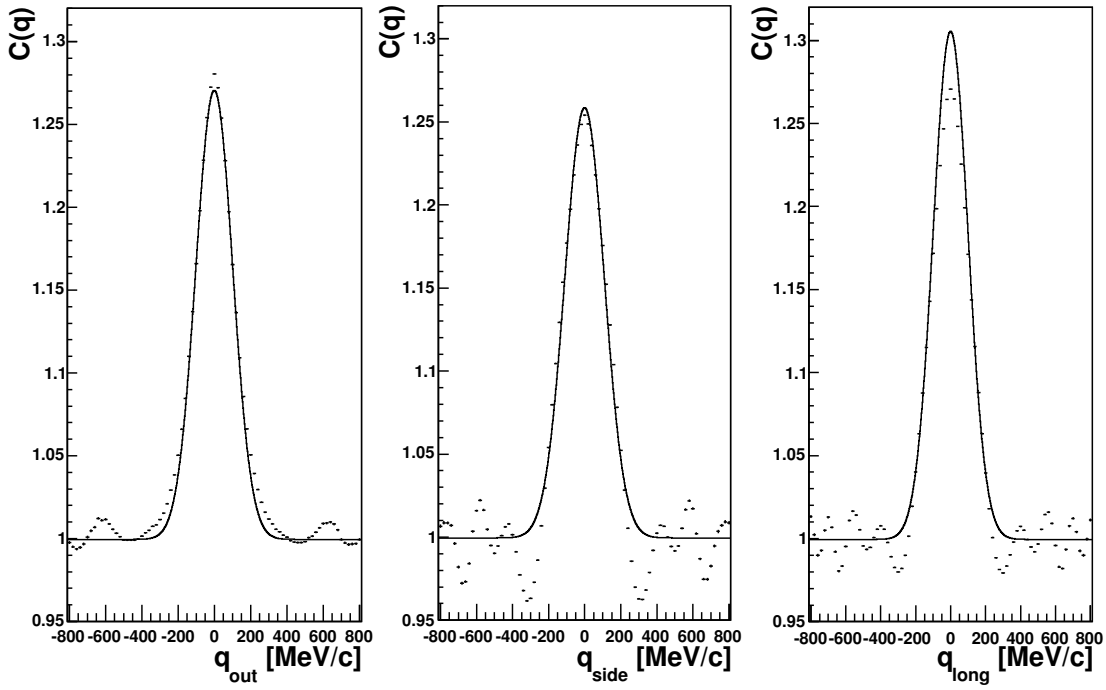

Figure 5.1.: The dots represent projections of the 3-dimensional correlation function for $K_\perp$=0.3-0.4 GeV and $N_{charged}^{\lvert\eta\rvert<1.2}$= 23-29. The lines represent a χ^2 fit of equation 3.5 to the correlation function. Both the result of the fit and the correlation function are integrated over a range of $q_i = \pm 0.17$ GeV in the other directions for the purpose of projection.

The $K_\perp$ dependence of the HBT radii extracted from the UrQMD freeze-out distribution is presented in figure 5.2 for the $dN_{ch}/d\eta$ classes defined in table 5.1 in the pseudorapidity interval $|\eta| < 1.2$ in comparison to the ALICE data. The UrQMD calculations are presented for different values of the formation time τ_f (τ_f= 0.3 fm/c, dashed lines; τ_f= 0.8 fm/c, full lines; τ_f=2 fm/c, dotted lines). For τ_f=0.3 fm/c, one obtains a good description for R_{out}, while R_{side} is slightly underpredicted and the values for R_{long} are in line with data from ALICE. The choice τ_f=0.8 fm/c leads to a slight overestimation of R_{out}, however it leads to a reasonable description of R_{side} data. Also the $K_\perp$ behaviour in R_{long} is much closer to the behaviour of the data. In contrast, a formation time of τ_f=2 fm/c, leads to a drastic overestimation of the data for all radii. Although there are discrepancies between model and data for all values of τ_f, the sensitivity on τ_f is much larger than those discrepancies. Therefore, the present ALICE data allows to constrain the formation time to values of $\tau_f \approx$ 0.3-0.8 fm/c.

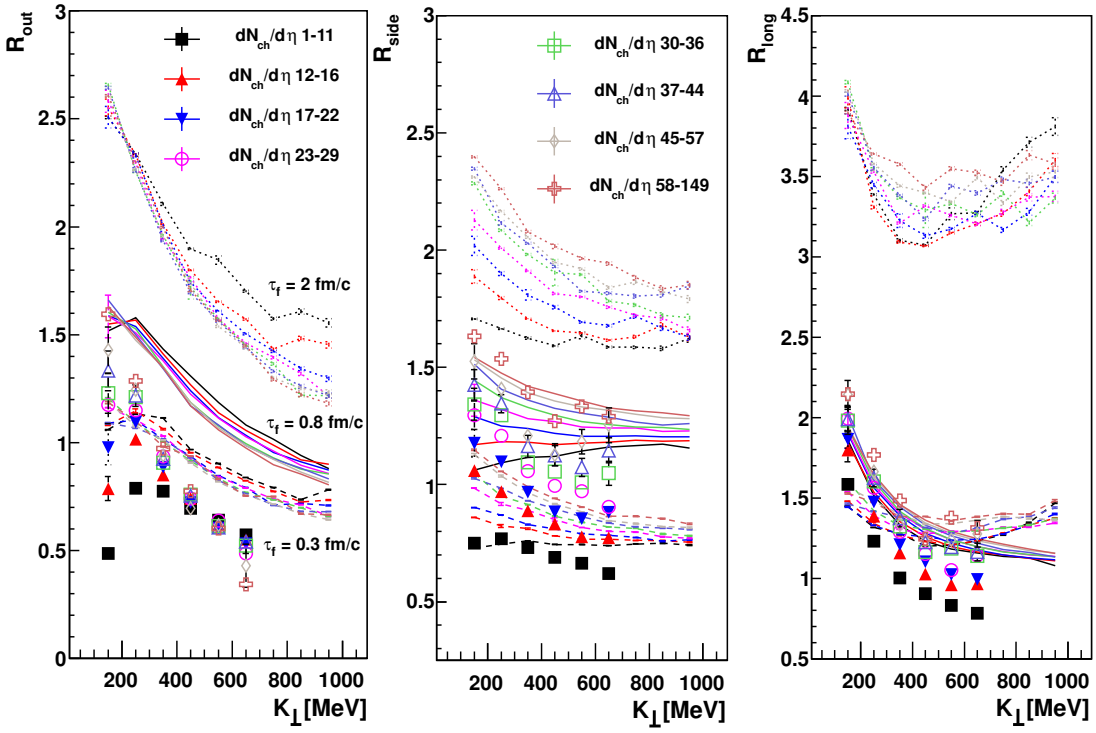

Figure 5.2.: The lines represent HBT radii in pp collisions at $\sqrt{s}$= 7 TeV from UrQMD for different multiplicities and formation times. The various line styles refer to results for τ_f = 0.3 fm/c (dashed), τ_f = 0.8 fm/c (default - full lines) and τ_f = 2 fm/c (dotted). The colors represent the multiplicity classes as defined in table 5.1. The points are data from the ALICE experiment [Aamo11a].

Let us finally discuss the overall shape of the radii as a function of multiplicity and $K_\perp$. The R_{side} radii (see figure 5.2, middle) from UrQMD and in the data are flat as a

function of $K_\perp$ for low multiplicity events. With increasing multiplicity the radii develop a decrease towards higher $K_\perp$. This is exactly the behavior one would expect for the development of space-momentum correlations with rising event multiplicity [Wern11b]. For R_{out} (figure 5.2, left) however, there is a $K_\perp$ dependence present in all multiplicity classes. Thus, only the development of radial flow with rising particle multiplicity seems not sufficient to explain the $K_\perp$ dependence. Since R_{out} and R_{long} contain lifetime contributions of the source and R_{side} does not, there seems to be an additional non-trivial $K_\perp$ and multiplicity dependence in the emission duration needed to explain the difference in the behaviour of R_{out}, R_{side} and R_{long}. This additional correlation might be due to an additional momentum dependence in τ_f apart from the trivial Lorentz boost. This would lead to a direct effect on the emission duration, because it changes the particles' production space-time points. It would also lead to an indirect change of the emission region, since the particle rescattering is influenced by τ_f. In the case of pp collisions the effect of rescattering should be negligible. Preformed hadron interactions become important in AA collisions [Arle03, Li08].

6. HBT analysis of Pb+Pb collisions at LHC energies

This chapter is based on [Li12]. In order to shed light on a large number of unsolved questions in fundamental physics [Balt08, Gian04, Weig06], the Large Hadron Collider (LHC) at CERN has been designed, installed, tested, and repaired in the past two decades and finally, started normal operation in the end of the year 2009. Since then, a tremendous amount of experimental data in various aspects of high energy physics has been obtained and received much attention by theoretical physicists. The extracted bulk properties of the high temperature fireball created in such ultra-relativistic collisions have provided unprecedented information for fundamental investigations of the phase diagram of Quantum Chromodynamics (QCD). In this chapter we want to explore the expansion properties of the created matter by investigating the spatial shape of the fireball at LHC energies using HBT correlations. The ALICE collaboration has published first results of two-pion Bose-Einstein correlations in both p-p [Aamo11a] and central Pb-Pb [Aamo11b] collisions at LHC energies in the beginning of the year 2011. These experimental results have attracted the research interest of several theoretical groups [Aamo11b, Karp11, Huma10, Wern11b], whose models are based on hydrodynamic/hydrokinetic and microscopic approaches.

In this chapter we show the HBT radii of two-pion correlations from central ($< 5\%$ of the total cross-section σ_T) Pb-Pb collisions at the LHC energy $\sqrt{s_{NN}} = 2.76$ TeV from UrQMD. The calculations are compared to ALICE data as well as to those at the RHIC energy $\sqrt{s_{NN}} = 200$ GeV. Some predictions and comparison works with data from reactions at LHC have already been pursued based on this version and showed encouraging results for the bulk properties (see [Mitr09, Pete11] and chapter 4). The UrQMD calculation results for p-p collisions at LHC energies are published in [Grae12b], see chapter 5.

6.1. HBT analysis details

To obtain HBT radii, first, about 200 and 10000 central events are calculated for Pb-Pb collisions at LHC and for Au-Au at RHIC, respectively. Then, the two-pion correlation functions are calculated via equation 3.3 (see also [Prat94]) in the longitudinally co-moving system (LCMS) [Bert88, Prat86] and are fitted by the Gaussian shape from equation 3.5.

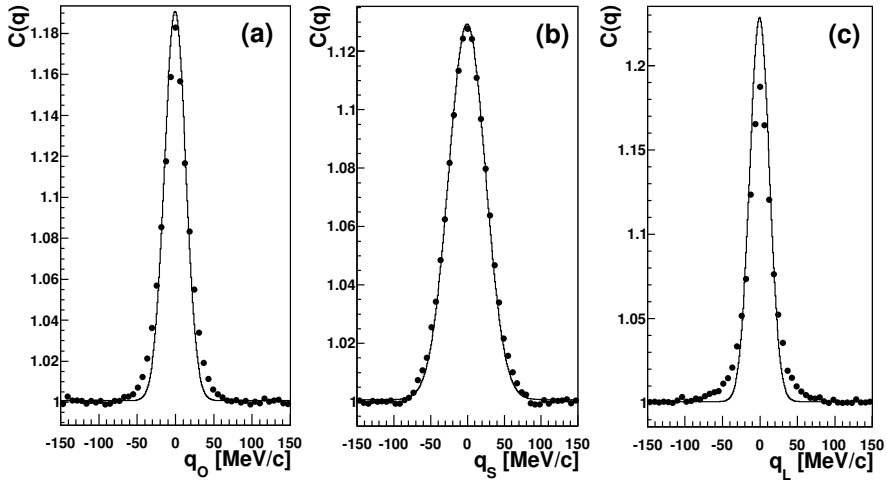

Figure 6.1.: Projections of the three-dimensional correlation function (points) and of the respective fit (lines) for the $K_\perp$-bin $200 - 300$ MeV/c and $|\eta| < 0.8$. When projecting on one axis, the other two components are restricted to the range (-30 $< q <$ 30) MeV/c.

The effect of cross-terms with $i \neq j$ on the HBT radii is found to be negligible in the present fits when a pseudorapidity cut $|\eta| < 0.8$ is used, as in experiments, and is not discussed in this chapter.

For central collisions, the HBT radii are, except for an implicit $\mathbf{K}_\perp$ dependence, related to regions of homogeneity by [Wied99]

$$R_O^2 = \left\langle (x - \beta_\perp t)^2 \right\rangle = \left\langle x^2 \right\rangle - 2 \left\langle \beta_\perp t x \right\rangle + \left\langle \beta_\perp^2 t^2 \right\rangle , \tag{6.1a}$$

$$R_S^2 = \left\langle y^2 \right\rangle , \tag{6.1b}$$

$$R_L^2 = \left\langle (z - \beta_L t)^2 \right\rangle = \left\langle z^2 \right\rangle - 2 \left\langle \beta_L t z \right\rangle + \left\langle \beta_L^2 t^2 \right\rangle , \tag{6.1c}$$

where x, y, z and t are the spatio-temporal separation of the particles in a pair and $\boldsymbol{\beta} = \mathbf{K}/K_0$. If no space-momentum correlations are present the regions of homogeneity and the source size coincide. In central collisions the relation $\left\langle x^2 \right\rangle \simeq \left\langle y^2 \right\rangle$ is satisfied. Thus R_O^2 and R_S^2 differ mainly in the last two terms of equation (6.1a). The first of these two terms is dependent on the strength of the correlation of emission time and transverse emission position, while the second one is especially sensitive to the particle emission duration.

6.2. Lifetime and $K_\perp$ dependent Results

The correlation functions are studied in bins of the transverse momentum $K_\perp = |\mathbf{k}_\perp|$. Figure 6.1 shows the projections of the three-dimensional correlation function (points)

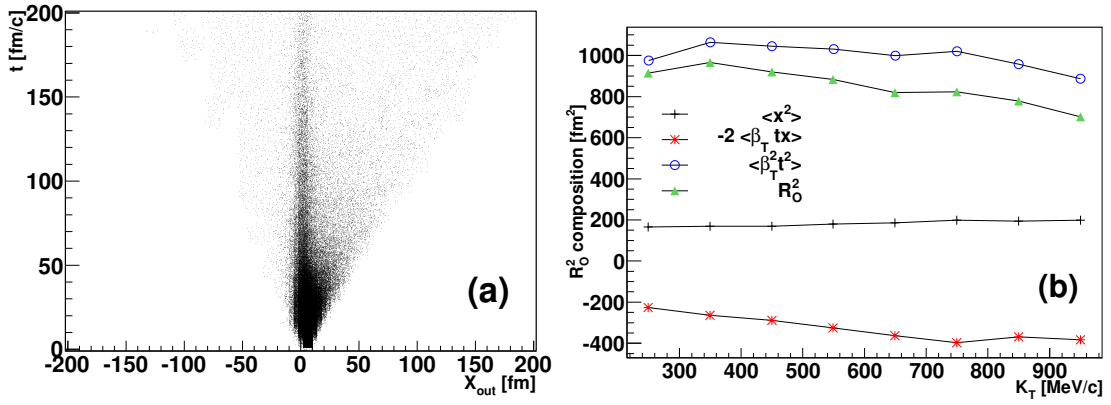

Figure 6.2.: (a) The transverse position x_{out} versus emission time distribution of pions with cuts $|\eta| < 0.8$, $200 < K_\perp < 300$ MeV/c, $|q_i| < 100$ MeV/c, and $t_{freezeout} < 199$ fm/c. (b) The contribution of terms $\langle x^2 \rangle$ (line with crosses), $-2\langle \beta_\perp tx \rangle$ (line with asterisks), and $\langle \beta^2 t^2 \rangle$ (line with open circles) in equation (6.1a), to R_O^2 (line with triangles) with same cuts as for (a).

and of the respective fit (lines) for the $K_\perp$-bin $200 - 300$ MeV/c. It is seen clearly that the correlator in sideward direction can be described by a Gaussian form fairly well. However, it deviates slightly from a Gaussian in the other two directions, especially in the longitudinal direction, as found and discussed in previous publications for HICs at lower energies [Li09b]. At LHC, the fraction of excited unstable particles is much larger than at lower beam energies, therefore, the non-Gaussian effect is more pronounced in the current calculations. At RHIC energies, the non-Gaussian effect was also seen in the experimental HBT correlator, especially in the longitudinal direction [Adam05b]. Furthermore, when comparing our fitting result in figure 6.1 with that observed in experiment (in figure 1 of Ref. [Aamo11b]), it is seen that the non-Gaussian effect is stronger in our calculations than in experiment. In [Li09b] this is studied in further detail and can be improved by the inclusion of a mean-field potential.

Besides the non-Gaussian effect, the contribution of the correlation between the emission time and position to the HBT radii, especially in the outward direction, has been paid more attention in recent years since it closely relates to the stiffness of the EoS of nuclear matter especially at the early stage of the whole dynamic process [Lin02, Li08, Li09a]. In figure 6.2 (a) we show the calculated emission time versus transverse position x_{out} of pions. The cuts $|\eta| < 0.8$ and $200 < K_\perp < 300$ MeV/c are adopted to have the same acceptance as for the extraction of the HBT radii. At the same time, since the correlation function and thus the HBT radii are mainly sensitive to pairs with small momentum difference, a cut on the relative pair momentum $|q_i| < 100$ MeV/c is applied as well. Further, in order to remove the contribution of long-lived resonances, a cut on the freeze-out time ($t_{freezeout} < 199$ fm/c) is used. It is found that, even in the cascade calculation, there exists a visibly positive correlation between the emission time and position. To

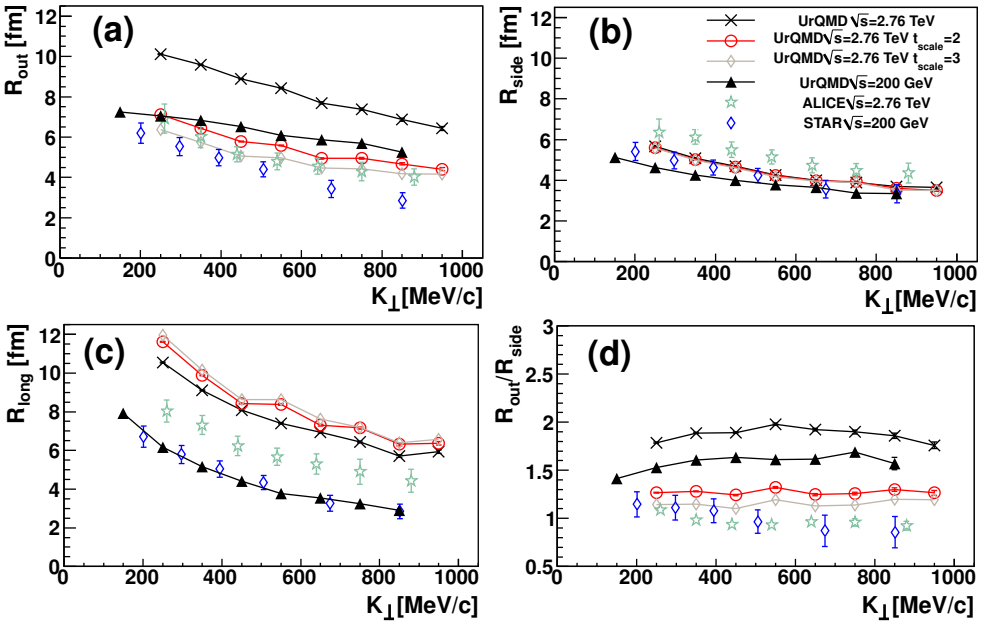

Figure 6.3.: $K_\perp$ dependence of pion HBT radii R_O [panel (a)], R_S [(b)], and R_L [(c)], as well as the ratio R_O/R_S [(d)], for central ($\sigma/\sigma_T < 5\%$) Pb-Pb collisions at LHC energy $\sqrt{s_{NN}} = 2.76$ TeV. For comparison, parameters for central ($\sigma/\sigma_T < 5\%$) Au-Au collisions at RHIC energy $\sqrt{s_{NN}} = 200$ GeV are also shown. Lines with triangles and crosses are for model calculations while scattered symbols are for experimental data of STAR/RHIC and ALICE/LHC collaborations taken from [Adam05b, Aamo11b]. Lines with circles and diamonds show results with an artificially decreased emission duration by a factor of $t_{scale} = 2$ and 3, separately, in the analysis of correlation function.

further analyze the importance of the $x - t$ correlation, we quantitatively calculate all three terms in equation (6.1a) and show them in figure 6.2 (b) as a function of $K_\perp$. As a whole, although the magnitude of the $x - t$ correlation term ($-2\langle\beta_\perp tx\rangle \approx$ -300 fm^2) is as big as that of the emission region term ($\langle x^2\rangle \approx 200$ fm^2), the most important contribution to R_O comes from the emission duration term ($\langle\beta_\perp^2 t^2\rangle \approx 1000$ fm^2). It implies that both a shorter duration time and a stronger $x - t$ correlation lead to a smaller R_O value, which will be further discussed in figure 6.3. Here, it is interesting to see that the direct computation of R_O leads to a value of ≈ 30 fm which is larger than the value extracted from the Gaussian fit to the correlation function by about a factor of three, as was also observed in the AMPT model calculations for Au-Au collisions at RHIC [Lin02].

Figure 6.3 shows the $K_\perp$ dependence of the HBT radii R_O, R_S, and R_L, as well as the ratio R_O/R_S, extracted from the Gaussian fit to the two-pion correlators. The UrQMD cascade calculations for central Pb-Pb collisions at LHC energy $\sqrt{s_{NN}} = 2.76$ TeV (lines with crosses) and central Au-Au collisions at RHIC energy $\sqrt{s_{NN}} = 200$ GeV

(lines with triangles) are compared to corresponding experimental data by ALICE/LHC (open stars) and STAR/RHIC (open diamonds). A strong decrease of the three HBT-radii with $K_\perp$ is seen both in experiments and in the UrQMD calculations for HICs. This implies a substantial expansion of the source and is qualitatively captured by the UrQMD dynamics. Following experimental results, the calculated HBT radii for Pb-Pb at LHC are found to be larger than those for Au-Au at RHIC. The largest increase exists in the longitudinal direction, which is also seen by the experiments. Although the comparison of the calculated HBT radii R_L and R_S with corresponding data at RHIC is fairly well, it gets worse when going to the higher LHC energy. At LHC the calculated R_S values at all $K_\perp$ are found to be slightly smaller than the data, while R_L and R_O values are larger than the data. Together with large calculated R_O, the emission time related quantity R_O/R_S is found to be markedly larger than the data.

From equation (6.1a) and figure 6.2 (b) it is clear that the value of R_O is strongly dependent on the emission duration of the particles. To further investigate the contribution of the emission duration to the HBT radii, we artificially decrease it by rescaling the relative time t to the "effective source center time" $\bar{t}$ ($= \langle t_i \rangle$) by $t = t_i - \bar{t} \rightarrow t' = (t_i - \bar{t})/t_{scale}$ in the calculation of the correlation function at LHC energies. This effectively changes equation (6.1a) to

$$R_O'^2 = \langle (x - \beta_\perp t')^2 \rangle = \langle x^2 \rangle - 2\frac{\langle \beta_\perp t x \rangle}{t_{scale}} + \frac{\langle \beta_\perp^2 t^2 \rangle}{t_{scale}^2}. \tag{6.2}$$

The results for this calculation are presented as lines with circles ($t_{scale} = 2$) and with diamonds ($t_{scale} = 3$) in figure 6.3. The artificially decreased emission duration leads to smaller R_O values in all $K_\perp$ bins but leaves R_S unchanged, as expected. Overall, it results in an improved agreement with the data of the R_O/R_S ratio. From figure 6.3, it is also found that R_L is overestimated at LHC. Since R_L is mainly related to the lifetime of the source, it implies that this lifetime is also overestimated by UrQMD. Other calculations in [Aamo11b, Grae12a] show that UrQMD overestimates the source lifetime by a factor of approximately $2 - 3$ when compared to LHC data. The overestimation of both R_O and R_L can be attributed to the known fact that the pressure in the early stage is not strong enough in the cascade model calculations. A higher pressure would lead to a more explosive expansion, a stronger phase-space correlation, and a faster decoupling of the system, thus leading to smaller regions of homogeneity. For more discussion we refer the reader to [Prat09a, Li08]. With the improved integrated Boltzmann + hydrodynamics hybrid approach [Pete08b, Pete11, Stei11b, Stei11a], where various EoS of nuclear matter during the hydrodynamic evolution may be treated consistently and a decoupling supplemented by realistic 3d hypersurfaces.

7. HBT scaling with particle multiplicity

This chapter is based on [Grae12a]. Over the last decade the experimental programs at the SPS and at RHIC have provided exciting pioneering data [Adam05b, Lisa00b, Alt08a, Afan02, Adam03a, Abel09a, Back06c, Back06b, Back03b, Abel09b]. These programs are currently extended into a system size scan with NA61 at SPS and a systematic beam energy scan with the RHIC-BES initiative. Particle correlations, i.e. Hanbury-Brown-Twiss correlation (HBT) or femtoscopy allow to gain deeper insights into the emission patterns and coherence regions of the matter created [Prat84, Siny89, Hama88, Wied99]. One generally assumes that the observed HBT radii scale with the charged particle density (or number of participants) as the charged particle density should be a good proxy for the final state volume [Lisa05]. However, the interferometry volume may not only depend on multiplicity, but also on the initial size of the colliding system [Siny11]. Indeed, one of the surprising LHC results concerns the scaling violation observed in pp reactions as compared to AA reactions at lower energies at the same charged particle density. In this chapter, we explore the spatial structure of the source created in collisions of various heavy-ions at different energies and centralities to shed light on the observed scaling violation when going from proton-proton to AA collisions at the LHC. For this we use the UrQMD model (see section 2.5). Other investigations on the charged particle yield scaling can be found in [Adam03a, Adam03c, Akke04, Akke06].

7.1. Scaling of the HBT radii

For the analysis in this chapter the correlation functions are fitted over a range $|q_i| <$ 800 MeV/c for proton-proton collisions, $|q_i| <$ 300 MeV/c for carbon-carbon collisions and $|q_i| <$ 150 MeV/c for all other collisions. The difference in the momentum ranges is motivated by the fact that the width of the peak in the correlation function gets broader for smaller systems. Thus, the fit range is bigger for proton-proton and carbon-carbon than it is for lead-lead collisions.

Figure 7.1 shows the three HBT radii R_{out}, R_{side} and R_{long} as a function of the charged particle multiplicity at midrapidity ($|\eta| < 1.2$ for pp and $|\eta| < 0.8$ for all other classes), $(dN_{ch}/d\eta)^{1/3}$ and fixed $K_\perp = 300 - 400$ MeV. The lines with symbols are simulation results for lead-lead collisions at $\sqrt{s_{NN}}$ = 2760, 200, 130, 62.4 GeV for 0-5%, 5-20%, 20-50% and 50-80% centrality, for carbon-carbon at $\sqrt{s_{NN}}$ = 200 GeV in the same centrality classes, for proton-proton at $\sqrt{s}$ = 7 TeV with different $dN_{ch}/d\eta$ classes, for central copper-copper collisions at $\sqrt{s_{NN}}$ = 200 GeV and for central lead-lead collisions at E_{lab} = 158 AGeV. The green stars are experimental results taken from [Adam05b, Lisa00b, Alt08a, Afan02, Adam03a, Abel09a, Back06c, Back06b, Back03b,

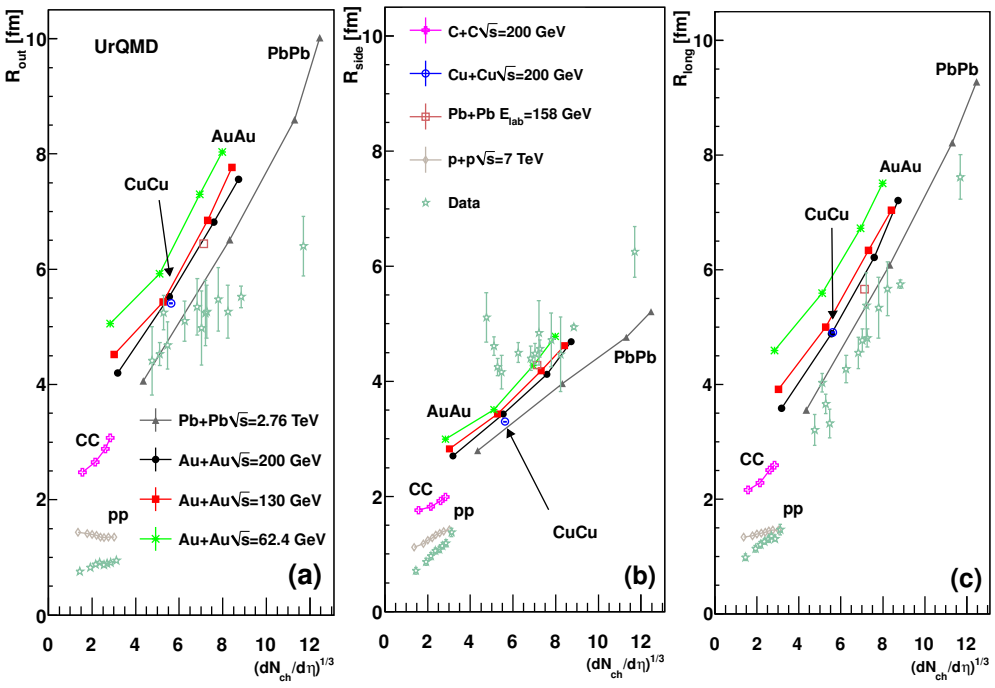

Figure 7.1.: The three HBT radii R_{out}, R_{side} and R_{long} as a function of the charged particle multiplicity at midrapidity, $(dN_{ch}/d\eta)^{1/3}$ and fixed $K_\perp = 300-400$ MeV. The lines with symbols are the simulation results. The gray triangles, the black circles, the red squares and the green crosses are for lead-lead collisions at $\sqrt{s_{NN}}$ = 2760, 200, 130, 62.4 GeV (in the same order) at 0-5%, 5-20%, 20-50% and 50-80% centrality for the different points. The pink crosses are results for carbon-carbon at $\sqrt{s_{NN}}$ = 200 GeV for the same centrality classes and the beige diamonds show results for various multiplicity classes from proton-proton collisions (see chapter 5). Blue circles and brown squares depict results for central copper-copper events at $\sqrt{s_{NN}} = 200$ GeV and central lead-lead collisions at E_{lab} = 158 AGeV. The green stars are experimental results for central gold and lead collisions at $K_\perp$ = 300 GeV/c taken from [Adam05b, Lisa00b, Alt08a, Afan02, Adam03a, Abel09a, Back06c, Back06b, Back03b, Abel09b, Aamo11a, Aamo11b].

Abel09b, Aamo11a, Aamo11b]. For nucleus-nucleus reactions one observes a rather linear scaling with $(dN_{ch}/d\eta)^{1/3}$. The scaling is very good if the change in $(dN_{ch}/d\eta)^{1/3}$ is caused by a change of centrality at a fixed energy. A small offset on the order of 2 fm - 3 fm is visible for different system sizes, if the radii are extrapolated to $N_{ch} \to 0$. This is expected due to the finite size of the nuclei in AA reactions [Siny11]. In contrast, increasing the center-of-mass energy leads to a reduction of the radii at a given fixed N_{ch}-bin. The scaling of the source size with $(dN_{ch}/d\eta)^{1/3}$ for different centralities is a hint that the underlying physics, e.g. pion production via resonance decay versus production via string fragmentation, is nearly unchanged by changes in the collision geometry. A change in $\sqrt{s}$ on the other hand results not only in different weights of the production mechanisms, but also in changed expansion dynamics towards a more violent expansion with increased energy. Qualitatively, one expects a scaling of the length of homogeneity as $R = R_{geom}/\sqrt{1 + \langle v_\perp^2 \rangle m_\perp / 2T}$ [Siny11, Akke95], where R_{geom} is the geometric size of the collision region, $v_\perp$ is the transverse flow velocity and T is the freeze-out temperature. I.e. the increase in transverse flow leads to a decrease of the observed radii with increasing energy as observed in the model. This combination leads to a deviation from the $(dN_{ch}/d\eta)^{1/3}$ scaling of the HBT radii. The proton-proton calculation (and the data) show significantly smaller radii and a different slope from what is expected from nucleus-nucleus results. This behaviour is attributed to the strongly different particle production mechanisms in AA and pp. I.e., bulk emission vs. string/jet dominated emission, which is also in line with the theoretically observed dependence of the HBT radii on the formation time of the hadrons from the jet fragmentation and string decay [Grae12b] (see chapter 5).

Since the $K_\perp$ dependence of the HBT radii tells us much about the expansion of the source [Prat84, Hama88], let us next investigate how a variation of $dN_{ch}/d\eta$ is reflected in the differential HBT radii as recently discussed in [True12]. Figure 7.2 shows the three HBT radii R_{out}, R_{side} and R_{long} at fixed charged particle multiplicity at midrapidity as a function of $K_\perp$. The shown calculations are chosen so that they fall roughly into two $\langle dN_{ch}/d\eta \rangle$ classes. The first class contains calculations with $\langle dN_{ch}/d\eta \rangle \approx 600$ (exact values are 670 for Pb+Pb at $\sqrt{s_{NN}} = 2760$ GeV, 20-50% centrality and 665, 595 and 509 for Pb+Pb at $\sqrt{s_{NN}} = 200$, 130, 62.4 GeV, 0-5% centrality). The second class contains calculations for $\langle dN_{ch}/d\eta \rangle \approx 25$ (exact values are 23 for C+C at $\sqrt{s_{NN}} = 200$ GeV, 0-5% centrality and 32, 28 and 23 for Pb+Pb at $\sqrt{s_{NN}} = 200$, 130, 62.4 GeV and 50-80% centrality).

A very similar slope in $K_\perp$ is observed for all UrQMD results. This leads to the conclusion that the observed HBT radii dependence on the radial flow in the model is weaker than observed in the data. The shift in magnitude of the radii is related to the magnitude differences already observed in figure 7.1 that are mainly dominated by geometry and $\sqrt{s}$ effects.

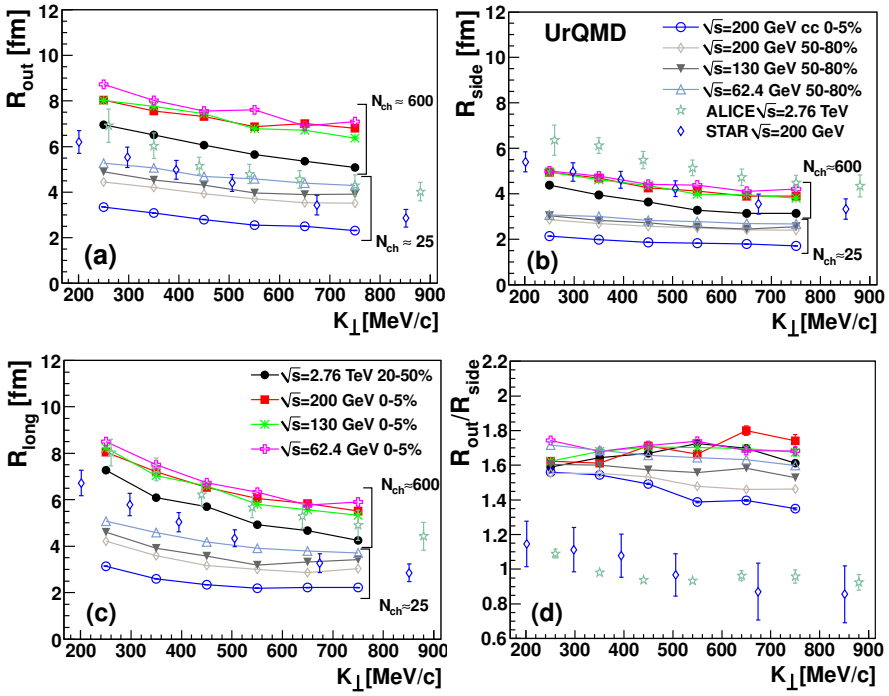

Figure 7.2.: The $K_\perp$ dependence of R_{out}, R_{side} and R_{long}. The black dots are calculations at $\sqrt{s_{NN}}$ = 2760 GeV and 20-50% centrality, the red squares, the green crosses and the pink crosses are lead-lead for 0-5% centrality at $\sqrt{s_{NN}}$ = 200, 130, 62.4 GeV. They have $\langle dN_{ch}/d\eta \rangle \approx$ 670, 665, 595, 509. The other presented calculations are carbon-carbon at $\sqrt{s_{NN}}$ = 200 GeV for 0-5% centrality (blue circles) and lead-lead at $\sqrt{s_{NN}}$ = 200, 130, 62.4 GeV (beige diamonds, grey triangles, blue triangles) all for 50-80% centrality. These collisions have $\langle dN_{ch}/d\eta \rangle \approx$ 23, 32, 28, 23. The green stars represent ALICE lead-lead data for central collisions at $\sqrt{s_{NN}}$ = 2760 GeV [Aamo11b]. The blue diamonds are experimental results for central gold-gold collisions at $\sqrt{s_{NN}}$ = 200 GeV from the STAR collaborator. [Adam05b]

7.2. Scaling of volume and freeze-out time

Next, let us investigate the energy and system size dependence of the homogeneity volume. Figure 7.3 shows the volume of homogeneity as a function of $dN_{ch}/d\eta$ for various systems. Lead-lead calculations are shown for $\sqrt{s_{NN}}$ = 2760, 200, 130, 62.4 GeV (grey triangles, black circles, red squares, green crosses) in the centrality classes 0-5%, 5-20%, 20-40% and 40-80%. The pink crosses show $\sqrt{s_{NN}}$ = 200 GeV carbon-carbon results for the same centralities, and the beige diamonds represent proton-proton calculations at $\sqrt{s}$ = 7 TeV for different $dN_{ch}/d\eta$ bins. Blue circles and brown squares depict results for central copper-copper events at $\sqrt{s_{NN}}$ = 200 GeV and central lead-lead events at E_{lab} = 158 AGeV. These results are compared to experimental data

[Adam05b, Lisa00b, Alt08a, Afan02, Adam03a, Abel09a, Back06c, Back06b, Back03b, Abel09b, Aamo11a, Aamo11b] which is represented by green stars.

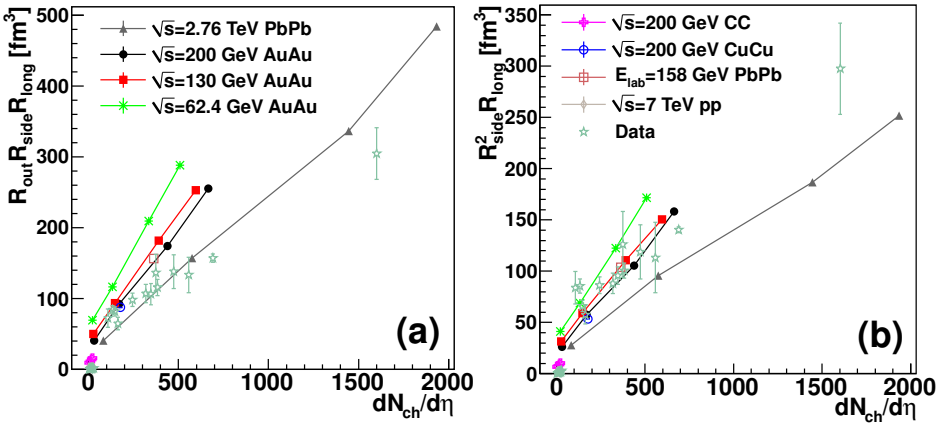

Figure 7.3.: Two definitions of the volume of homogeneity as a function of energy for various systems. In the left plot the volume is defined as $R_{out}R_{side}R_{long}$ and in the right plot the volume is defined as $R^2_{side}R_{long}$. The gray triangles, black circles, red squares and green crosses depict UrQMD results for lead-lead collisions at (in this order) $\sqrt{s_{NN}}$ =2760, 200, 130, 62.4 GeV for the centralities 0-5%, 5-20%, 20-40%, 40-80%. The pink crosses are carbon-carbon calculations at $\sqrt{s_{NN}} = 200$ GeV for the same centralities, the blue circles are central copper-copper collisions at $\sqrt{s_{NN}} = 200$ GeV and the brown squares are central lead-lead collisions at $E_{lab} = 158$ AGeV. The beige diamonds depict proton-proton results at $\sqrt{s} = 7$ TeV for different $(dN_{ch}/d\eta)^{1/3}$ classes. The green stars show experimental results taken from [Adam05b, Lisa00b, Alt08a, Afan02, Adam03a, Abel09a, Back06c, Back06b, Back03b, Abel09b, Aamo11a, Aamo11b].

In line with the experimental data, a strong increase in the volume proportional to the charged particle multiplicity is observed. A good agreement between experiment and theory is observed for the quantity $R^2_{side}R_{long}$ while the experimental results for $R_{out}R_{side}R_{long}$ are slightly overestimated. This is due to a too large R_{out} in the calculations. The overestimation of R_{out} is common for hadronic cascade models and can be explained by a lack of pressure in the early stage of the heavy-ion collision [Li08, Prat09b]. While the volume of the homogeneity region for each individual energy scales very well with $dN_{ch}/d\eta$ figure 7.3 shows a steepening slope with decreasing energy. The calculations also hint to an offset for AA reactions on the order of 25 fm^3 ($R^2_{side}R_{long}$) and 50 fm^3 ($R_{out}R_{side}R_{long}$).

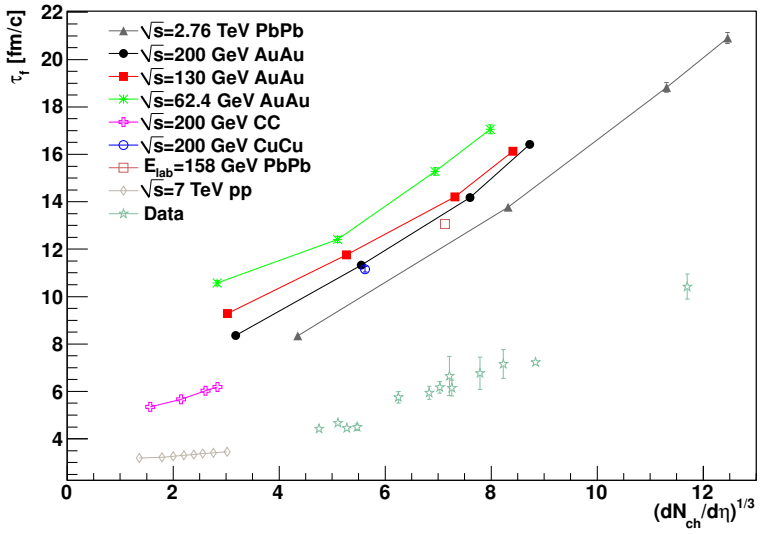

Figure 7.4.: The freeze-out time as a function of energy for various systems. The gray triangles, black circles, red squares and green crosses depict UrQMD results for lead-lead collisions at (in this order) $\sqrt{s_{NN}}$ =2760, 200, 130 62.4 GeV for the centralities 0-5%, 5-20%, 20-40%, 40-80%. The pink crosses are carbon-carbon calculations at $\sqrt{s_{NN}}$ = 200 GeV for the same centralities, the blue circles are central copper-copper collisions at $\sqrt{s_{NN}}$ = 200 GeV and the brown squares are central lead-lead collisions at E_{lab} = 158 AGeV. The beige diamonds depict proton-proton results at $\sqrt{s}$ = 7 TeV for different $(dN_{ch}/d\eta)^{1/3}$ classes. The green stars show experimental results taken from [Adam05b, Lisa00b, Alt08a, Afan02, Adam03a, Abel09a, Back06c, Back06b, Back03b, Abel09b, Aamo11b].

Finally, we explore the apparent freeze-out times τ_f. The results are obtained by fitting the hydrodynamically motivated equation 7.1 [Aamo11b, Makh88] to the $K_\perp$ dependence of R_{long} in the interval $K_\perp$ = 200-800 MeV/c. For this purpose the pion freeze-out temperature is assumed to be T = 120 MeV.

$$R^2_{long} = \tau_f^2 \frac{T}{m_\perp} \frac{K_2(m_\perp/T)}{K_1(m_\perp/T)}, \tag{7.1}$$

where $m_\perp = \sqrt{m_\pi^2 + K_\perp^2}$ and K_i are the integer order modified Bessel functions. Figure 7.4 shows the freeze-out time as a function of $dN_{ch}/d\eta$ for various systems. The grey triangles, the black circles, the red squares and the green crosses are calculations of lead-lead collisions at $\sqrt{s_{NN}}$ = 2760, 200, 130, 62.4 GeV (in the same order) for the centralities 0-5%, 5-20%, 20-40%, 40-80%. The pink crosses are carbon-carbon collisions at $\sqrt{s_{NN}}$ = 200 GeV for the same centralities. The blue circles are calculations for central copper-copper collisions at $\sqrt{s_{NN}}$ = 200 GeV and central lead-lead collisions at E_{lab} = 158 AGeV. Experimental results [Adam05b, Lisa00b, Alt08a, Afan02, Adam03a, Abel09a, Back06c, Back06b, Back03b, Abel09b, Aamo11b] are depicted by

green stars. As for all the other observables, there is scaling for each energy individually. As anticipated from the calculations of R_{long} the decoupling time τ_f increases with decreasing energy. This confirms the idea of a shorter decoupling time with increased energy. The offset in τ_f for $dN_{ch}/d\eta \to 0$ seems to hint towards a minimal decoupling time $\tau_f^{min} \approx 4 - 8$fm/c in AA reactions and $\tau_f^{min} < 2$ fm/c in pp.

8. Compressibility from event-by-event HBT

In thermodynamics, volume fluctuations are directly related to the isothermal compressibility. We use UrQMD (see chapter 2.5) to simulate Pb+Pb collisions at $\sqrt{s_{NN}} = 2.76$ TeV. At LHC energies, for the first time, the multiplicity is high enough to allow an event-by-event HBT (EbE-HBT) analysis. This makes it possible to measure the compressibility of the heated matter by extracting the volume fluctuations. There have been one-dimensional event-by-event HBT analyses [Stoc99], but no three-dimensional ones so far. In this chapter, we use the volume fluctuations obtained by the EbE-HBT with the goal to determine the isothermal compressibility κ_T of the matter present during the collision.

8.1. Underlying theory

8.1.1. Compressibility

Since it is very hard to access κ_T experimentally there are only a few suggestions on how to do so [Mrow98]. In this chapter we demonstrate how to measure κ_T. First of all we need to connect κ_T to measurable quantities. We do this using

$$\frac{\langle \Delta V^2 \rangle}{VT} = -\frac{1}{V}\left(\frac{\partial V}{\partial p}\right)_T = \frac{1}{\kappa_T} \,, \tag{8.1}$$

which can be derived using basic thermodynamics [Land96]. Here V,T and $\langle \Delta V^2 \rangle$ are the volume, temperature and the variance of the volume of the medium under investigation. All of these quantities are in principle measurable taking some intermediate steps.

8.1.2. Event-by-event HBT

One of the quantities needed to determine κ_T from equation 8.1 is the variance of the volume of the pion producing interaction region $\langle \Delta V^2 \rangle$. To measure it, we use pion HBT correlations.

First, we calculate the correlation function $C(\mathbf{q})$ given by equation 3.3 in the longitudinal comoving frame. Usually, the correlation function is averaged over a large number of events from the same collision class. High multiplicities at LHC energies, however, allow to construct $C(\mathbf{q}, \mathbf{K})$ using particles from only one event. In experiment, one would still use mixed events and/or different sign pairs to calculate the correlation function even if

one is doing EbE-HBT.

We fit the resulting correlation functions using a gaussian given by equation 3.5 to obtain the Pratt-Bertsch radii R_{ij}. Even though the R_{ij} are related to regions of homogeneity [Siny89, Hama88] and only approximately to the source sizes, we use their values to calculate the volume $V = R_O R_S R_L$ for every event, which allows us to calculate $\langle \Delta V^2 \rangle$ too.

8.1.3. Effective temperature

The last quantity needed to calculate κ_T is the temperature of the matter in question. We use the usual approach and calculate the m_T spectrum of the pions. We then fit it with

$$\frac{1}{m_T^2}\frac{dN}{dm_T} \sim e^{-\frac{m_T}{T}} \tag{8.2}$$

to get T. The temperature varies however during the evolution of the collisions. Also resonance decays contribute to the m_T spectrum, which in turn becomes slightly non-thermal. For this reason T is often called an effective temperature or inverse slope parameter, but here we will refer to it as temperature.

8.2. Compressibility results

In this chapter we study central lead-lead collisions at $\sqrt{s_{NN}} = 2.76$ TeV within the pseudorapidity window $|\eta| < 1.2$. For our goal to determine κ_T we need to calculate $\langle \Delta V^2 \rangle$. Figure 8.1 shows three slices through a pion correlation function from an arbitrary single event. The black line is a one dimensional gaussian with the parameters obtained from the complete three dimensional fit. At a first glance the statistical errors in the correlation function are pretty big. However the situation is not as bad as it looks, since only slices are shown and there are plenty of support points for the actual three dimensional fit so that a good fit can be achieved most of the time.

One of the difficulties is that even single failed fits can have a huge impact on the final result of the fluctuations. For that reason we have to define a criterion to sort out the fit results that are "not good", in a way that does not bias the result. To achieve this we introduced a cut on the χ^2/DoF and discarded all results with a χ^2/DoF bigger than this cut. The results of this study are shown on the left in figure 8.2. It becomes obvious that the result for $\langle \Delta V^2 \rangle$ does not change anymore for $\chi^2/DoF > 1.2$. So we used a cut of $\chi^2/DoF = 2$ for our analysis. The results for V and $\langle \Delta V^2 \rangle$ can be found in table 8.1.

The last ingredient we need to calculate κ_T is the temperature of the pions. Since the dN/dm_T spectrum deviates slightly from an exponential, the final result depends on the fitted region. We take that into account by varying the fitted region. The right panel of figure 8.2 shows the result for the temperature when fitting from $m_\perp = 200$ MeV up

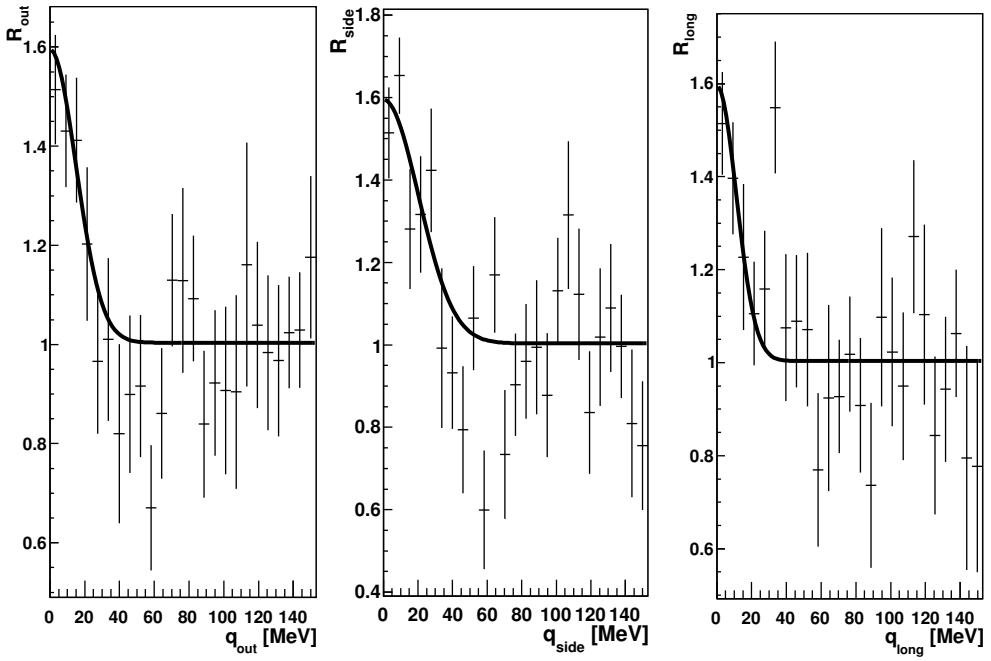

Figure 8.1.: Slices of the correlation function for a random event in Out (left panel), Side (middle panel) and Long (right panel) direction. The black line represents a 1D gaussian with the parameters from the 3D fit by equation 3.5.

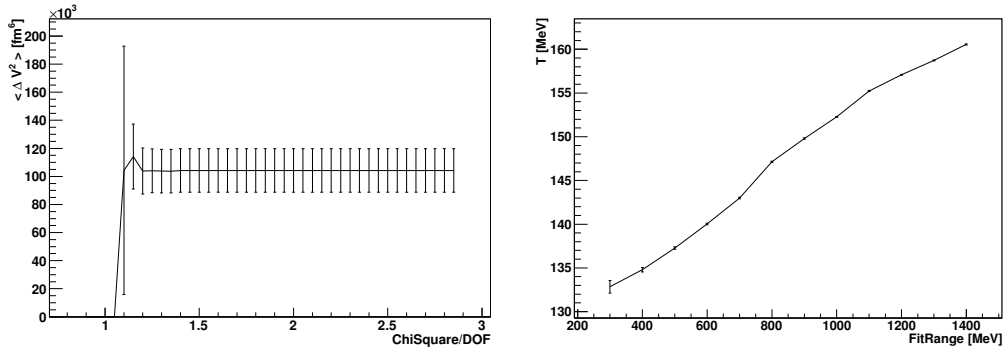

Figure 8.2.: (left) Volume fluctuations as a function of the χ^2/DoF cut used to sort out failed fits. (right) Temperature as a function of the fit range of equation 8.2 to the dN/dm_T spectrum. The fit is performed from 200 MeV up to the value plotted on the x-axis.

b [fm]	κ_T $\left[\frac{MeV}{\mathrm{fm}^3}\right]$	V [fm^3]	$\langle \Delta V^2 \rangle [\mathrm{fm}^6]$	T [MeV]
0	1.09 ± 0.47	773.55 ± 322.83	104222 ± 15517	147.40 ± 13.86
0-3.4	1.02 ± 0.51	651.8 ± 305.59	93384 ± 13200	146.69 ± 14.08

Table 8.1.: This table displays an overview of the results for κ_T, V, $\langle \Delta V^2 \rangle$ and T. The studied system is lead-lead at $\sqrt{s_{NN}} = 2.76$ TeV and $|\eta| < 1.2$.

to the value plotted on the x-axis. The mean value for T is presented in table 8.1, as well as the maximal variation as its error. This leads to $\kappa_T = 1.09 \pm 0.47 \frac{\mathrm{MeV}}{\mathrm{fm}^3}$ in head-on collisions and $\kappa_T = 1.02 \pm 0.51 \frac{\mathrm{MeV}}{\mathrm{fm}^3}$ in the 5 % most central collisions.

9. Tilt in non-central collisions

This chapter is based on [Moun11]. It has long been recognized that measurements relative to the direction of the impact parameter of the collision are more sensitive to important underlying physics of the system than are angle-integrated measurements. The azimuthal dependence of particle yields and spectra – with "directed" and "elliptical flow" being the most prominent ones – are extensively used to extract the QCD equation of state (EoS) and transport coefficients of the quark-gluon plasma such as viscosity [Kolb00, Volo08]. On the other hand, azimuthally-integrated p_T spectra can flag the existence of collective behavior, but are not as discriminating between different models producing such behavior [Lisa95, Song11]. Similarly, the azimuthal dependence of jet quenching is a more discriminating probe of partonic energy loss than azimuthally-integrated measurements [Cole05, Maju07, Bass09]. It is possible that azimuthally-differential analyses might yield a similar improvement in sensitivity of femtoscopy.

Most femtoscopic analyses of pion correlations extract so-called "HBT radii" (c.f. discussion in [Lisa05]) which fully describe the emission distribution only if it is purely Gaussian and features no collective motion. Strictly speaking, neither of these conditions characterize heavy-ion collisions, and there has been considerable activity in measuring the non-Gaussian features of the source via "imaging" techniques [Brow97, Pani00] that fit the source with a sum of spline functions. Large non-Gaussian tails are mostly explained by long-lived resonance production [Brow07].

Moving beyond HBT radii themselves, which characterize the geometry only of subsets ("homogeneity regions" [Makh88]) of the overall source, one is interested in the shape and orientation of the emission region as a whole. Retiere and Lisa have proposed [Reti04] a formula connecting the azimuthal oscillations of HBT radii with the transverse anisotropic shape of the source. Here, we follow the same line and propose a formula for the tilt of the source relative to the beam direction. Both of these formulae are strictly valid only for Gaussian, non-flowing sources. In this chapter, we test these formulae in the context of a realistic transport model featuring non-Gaussian freeze-out distributions and strong flow. We find reasonable consistency between the source eccentricity and tilt as extracted directly from the space-time freeze-out coordinates and the same quantities estimated with the formulae. The discrepancy between the two provides an estimate of the systematic uncertainty one expects, when using azimuthally-differential pion correlation measurements to extract the underlying source shape and orientation.

In section 9.1, we define the formalism and the connection between HBT radii and an

anisotropic but simplified static Gaussian source. There, we present formulae connecting measurable quantities to the interesting features of the geometry. In section 9.2, UrQMD is used to generate a freeze-out distribution featuring non-Gaussian geometry and strong collective flow. We discuss the non-trivial anisotropies of the distribution and the relationship between regions of homogeneity [Makh88, Akke95] and the "whole" source of emission points. In section 9.3, we simulate an experimental analysis, using the UrQMD-generated distributions. We build two-pion correlation functions and use the formulae presented in section 9.1 to estimate the source anisotropies. The calculations are compared to reported experimental results from Au+Au collisions at $\sqrt{s_{NN}} = 3.84$ GeV and predictions are given for heavy-ion collisions at $\sqrt{s_{NN}} = 7.7$ GeV, relevant for FAIR and the RHIC energy scan.

9.1. HBT radii and their connection to the underlying source

As pointed out in section 3.2, femtoscopic two-particle correlation functions as a function of the relative momentum $q = p_1 - p_2$ are often fitted in terms of Gaussian HBT radii $R^2_{i,j}$

$$C(q) = 1 + \lambda \exp\left(- \sum_{i,j=o,s,l} q_i q_j R^2_{i,j} \right). \tag{9.1}$$

Indices i and j indicate the components of the q vector in the so-called Bertsch-Pratt "out-side-long" coordinate system as defined in section 3.3 [Prat86, Bert89, Csor90]. It is worthwhile pointing out that, while one may simultaneously flip the signs of all components of q by swapping the designation of particles 1 and 2, the correlation function depends only on even-order products of q's components; these products have meaningful sign.

We begin by considering a simple source of midrapidity pions which is a Gaussian ellipsoid in space and time, with the major axis of the ellipse tilted with respect to the beam direction, as sketched in figure 9.1. The distribution is characterized by five parameters: a temporal scale, three spatial scales and a tilt angle

$$f(x,y,z) \sim \exp\left(-\frac{(x\cos\theta_s - z\sin\theta_s)^2}{2\sigma^2_{x'}} - \frac{y^2}{2\sigma^2_y} - \frac{(x\sin\theta_s + z\cos\theta_s)^2}{2\sigma^2_{z'}} - \frac{t^2}{2\sigma^2_t} \right), \tag{9.2}$$

where the primes on $\sigma_{x'}$ and $\sigma_{z'}$ signify that these correspond to principle axes of the ellipse.

Its transverse eccentricity about its (tilted) major axis is defined as

$$\epsilon' \equiv \frac{\sigma_y^2 - \sigma_{x'}^2}{\sigma_y^2 + \sigma_{x'}^2} \tag{9.3}$$

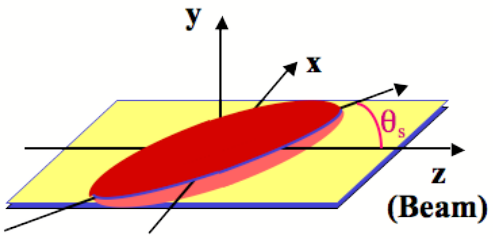

Figure 9.1.: The simplified parameterization of the freeze-out distribution in a heavy-ion collision. In addition to the timescale and three spatial length scales, the ellipsoid may be tilted in the direction of the impact parameter x, relative to the beam axis z.

If $\theta_s = 0$ and $\sigma_x = \sigma_y \equiv \sigma_\perp$ (or equivalently in an azimuthally-integrated analysis), only three parameters characterize the source, and the HBT radii are given by

$$\begin{aligned} R_s^2 &= \sigma_\perp^2 \ , \\ R_o^2 &= \sigma_\perp^2 + \beta_\perp^2 \sigma_t^2 \ , \\ R_l^2 &= \sigma_z^2 + \beta_l^2 \sigma_t^2 \ , \end{aligned} \tag{9.4}$$

where $\beta_\perp$ and β_l are the transverse and longitudinal velocities of the pion pair. "Cross-term" radii $R_{i\neq j}^2$ vanish by symmetry [Lisa00c, Hein02a].

For the more general case, there are six HBT radii, and they depend on the azimuthal angle ϕ. This angle is meaningfully defined over the range [0,2π] about the beam direction relative to the impact parameter, which is defined as the direction perpendicular to the beam, pointing from one nucleus moving in a specific beam direction to the other nucleus. Swapping the two nuclei reverses the direction of the impact parameter (x direction); however, it also reverses the "long" (z) direction. Hence, the sense of the tilt θ_S is well-defined; a source with positive tilt features a positive spatial $x - z$ correlation, as shown in figure 9.1. Experimental measurement of the sense of the tilt [Lisa00a] requires measuring the direction of the impact parameter, for example through directed flow of net baryons at forward rapidity.

The HBT radii, measured as a function of angle ϕ relative to the beam axis, are driven by source widths $\sigma_x, \sigma_y, \sigma_z$, rather than $\sigma_{x'}, \sigma_y, \sigma_{z'}$. The relationships between these widths are given by

$$\begin{aligned} \sigma_{x'}^2 &= \sigma_x^2 \cos^2\theta_s + \sigma_z^2 \sin^2\theta_s + \sigma_{xz}^2 \sin 2\theta_s \ , \\ \sigma_{z'}^2 &= \sigma_x^2 \sin^2\theta_s + \sigma_z^2 \cos^2\theta_s - \sigma_{xz}^2 \sin 2\theta_s \ , \end{aligned} \tag{9.5}$$

where σ_{xz}^2 is the covariance between x and z in the source function; see [Lisa00c] for details.

The HBT radii are related to these widths as [Lisa00c] (see A.3.1)

$$\begin{aligned} R_s^2(\phi) &= \tfrac{1}{2}\left(\sigma_x^2+\sigma_y^2\right)+\tfrac{1}{2}\left(\sigma_y^2-\sigma_x^2\right)\cos 2\phi\,, \\ R_o^2(\phi) &= \tfrac{1}{2}\left(\sigma_x^2+\sigma_y^2\right)-\tfrac{1}{2}\left(\sigma_y^2-\sigma_x^2\right)\cos 2\phi\,+\beta_\perp^2\sigma_t^2\,, \\ R_{os}^2(\phi) &= \tfrac{1}{2}\left(\sigma_y^2-\sigma_x^2\right)\sin 2\phi\,, \\ R_l^2(\phi) &= \sigma_z^2+\beta_l^2\sigma_t^2\,, \\ R_{ol}^2(\phi) &= \sigma_{xz}^2\cos\phi\,, \\ R_{sl}^2(\phi) &= -\sigma_{xz}^2\sin\phi\,. \end{aligned} \tag{9.6}$$

In analogy with equation 9.3, we identify the eccentricity of the source around the beam axis as

$$\epsilon \equiv \frac{\sigma_y^2-\sigma_x^2}{\sigma_y^2+\sigma_x^2}\quad . \tag{9.7}$$

Equations 9.6 express the explicit ϕ-dependence of the HBT radii for a non-flowing source; there is no implicit ϕ-dependence in any of the variables for a non-flowing source. For a source with flow, the constants, e.g. σ_y, may themselves depend on ϕ. In this case, our equations will be violated; below, we quantify this violation and its effect on the extraction of θ_s and ϵ.

Experimentally, one measures the squared HBT radii and calculates the Fourier coefficients quantifying their azimuthal dependence, per [Hein02a, Reti04]

$$\begin{aligned} R_s^2(\phi) &= R_{s,0}^2+2\textstyle\sum_{n=2,4,6,\ldots}R_{s,n}^2\cos(n\phi)\,, \\ R_o^2(\phi) &= R_{o,0}^2+2\textstyle\sum_{n=2,4,6,\ldots}R_{o,n}^2\cos(n\phi)\,, \\ R_{os}^2(\phi) &= 2\textstyle\sum_{n=2,4,6,\ldots}R_{os,n}^2\sin(n\phi)\,, \\ R_l^2(\phi) &= R_{l,0}^2+2\textstyle\sum_{n=2,4,6,\ldots}R_{l,n}^2\cos(n\phi)\,, \\ R_{ol}^2(\phi) &= 2\textstyle\sum_{n=1,3,5,\ldots}R_{ol,n}^2\cos\phi\,, \\ R_{sl}^2(\phi) &= 2\textstyle\sum_{n=1,3,5,\ldots}R_{sl,n}^2\sin\phi\quad . \end{aligned} \tag{9.8}$$

Equivalently,

$$R_{\mu,n}^2(p_T) = \begin{cases} \langle R_\mu^2(p_T,\phi_p)\cos(n\phi_p)\rangle & (\mu = o,s,l,ol) \\ \langle R_\mu^2(p_T,\phi_p)\sin(n\phi_p)\rangle & (\mu = os,sl) \end{cases}. \tag{9.9}$$

In our no-flow Gaussian model, then, the source geometry and orientation are extracted from the Fourier coefficients. Identifying the tilt angle requires [Lisa00c, Hein02a] measuring HBT relative to the first-order reaction plane [Volo08]. Published results from the STAR [Adam04] and CERES [Adam08] collaborations use only the 2$^{\text{nd}}$-order plane

and so only report the source eccentricity about the beam axis. (Efforts to perform the analysis relative to the first-order plane are underway at RHIC [Agga10].) In this case [Reti04] (see A.3.2)

$$\epsilon = 2 \cdot \frac{\tilde{R}^2_{s,2}}{R^2_{s,0}} \quad . \tag{9.10}$$

For the moment, we ignore the tildes above the $n \neq 1$ Fourier coefficients here and below. They represent a trivial finite-binning correction discussed later in section 9.3.

If the first-order plane is identified, first-order azimuthal oscillations in R^2_{sl} and R^2_{ol} are measurable. In this case one obtains the tilt angle according to [Lisa00c] (see A.3.1)

$$\theta_s = \tfrac{1}{2} \tan^{-1} \left(\frac{-4\tilde{R}^2_{sl,1}}{R^2_{l,0} - R^2_{s,0} + 2\tilde{R}^2_{s,2}} \right) . \tag{9.11}$$

The transverse eccentricity in the "natural" frame tilted relative to the beam axis is

$$\epsilon' = \frac{2\tilde{R}^2_{s,2}\left(1 + \cos^2\theta_s\right) + \left(R^2_{s,0} - R^2_{l,0}\right)\sin^2\theta_s - 2\tilde{R}^2_{sl,1}\sin 2\theta_s}{R^2_{s,0}\left(1 + \cos^2\theta_s\right) + \left(2\tilde{R}^2_{s,2} + R^2_{l,0}\right)\sin^2\theta_s + 2\tilde{R}^2_{sl,1}\sin 2\theta_s} \quad . \tag{9.12}$$

9.2. Freeze-out distributions from a more realistic model

Our simple model of the emission function given in equation 9.2 is unrealistic in at least two ways. Firstly, while realistic emission functions are often roughly Gaussian, they are never perfectly so; in this case, the two-pion correlation function is likewise non-Gaussian. Extracting Gaussian HBT radii through fits with equation 9.1, then, could in principle generate considerable mis-representation of the emission function.

The second over-simplification of the source discussed above is its lack of collective flow, which generates correlations between a particle's emission position and its momentum [Makh88]. For example, an explosively flowing source will boost particles emitted from its right side, towards the right. The freeze-out distribution of particles with a given momentum vector is known as the region of homogeneity for that momentum vector. In *principle*, the homogeneity regions for different azimuthal angles might be completely disjoint and unrelated, obviously invalidating equations 9.6, 9.10, 9.11 and 9.12. In practice, the homogeneity regions in blast-wave models [Reti04] or hydrodynamic simulations [Hein02b] are naturally related. For boost-invariant sources, equation 9.10 is estimated to be good to $\approx 30\%$ in these models [Reti04].

While blast-wave and boost-invariant hydro models do feature non-Gaussian sources and collective flow, they are still simplistic. Firstly, any boost-invariant model by definition has no tilt relative to the beam axis; thus they are unable to access physics associated with θ_s. Secondly, they typically use the Cooper-Frye formula to model particle

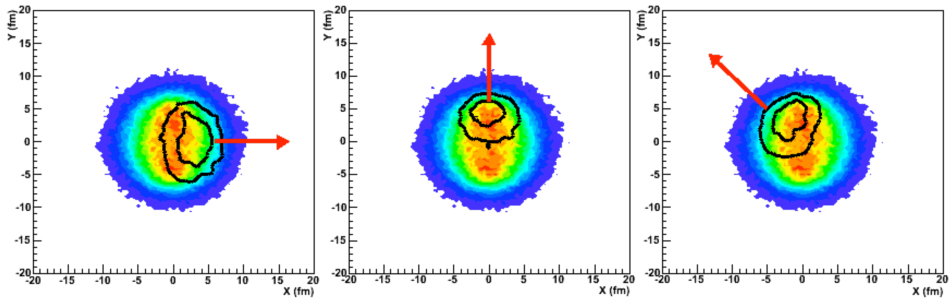

Figure 9.2.: Pion emission points from UrQMD simulations of Au+Au collisions with collision energy $\sqrt{s_{NN}} = 3.84$ GeV (corresponding to a 6 AGeV beam incident on a fixed target) and impact parameter $b = 4-8$ fm. Colored contours (identical for the three panels) show the emission point density of all pions with $p_T < 0.4$ GeV/c. Black contours in the left, middle and right panels indicate the density of emission points for pions with $\phi = \left[-\frac{\pi}{8}, \frac{\pi}{8}\right]$, $\left[\frac{3\pi}{8}, \frac{5\pi}{8}\right]$ and $\left[\frac{5\pi}{8}, \frac{7\pi}{8}\right]$, respectively.

freeze-out from a calculated or parameterized hypersurface; while momentum-space observables (e.g. v_2) may be insensitive to this procedure, interferometry is known to be quite sensitive to the freeze-out procedure.

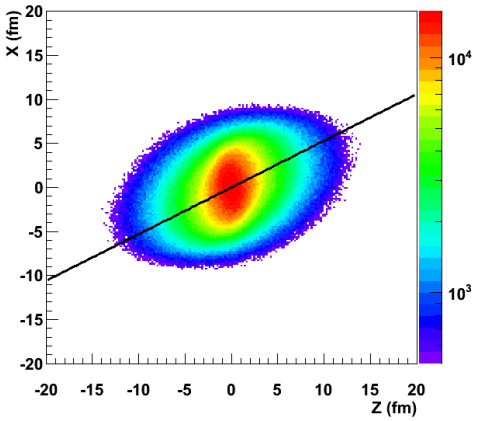

Figure 9.3.: Freeze-out distribution of pions from $\sqrt{s_{NN}} = 3.84$ GeV (6 AGeV beam energy on fixed target) Au+Au collisions with impact parameter $b = 4-8$ fm in the reaction $(x-z)$ plane, as calculated from UrQMD.

In UrQMD, the freeze-out space-time point is naturally defined as the last interaction of a particle. The freeze-out distribution of pions from $\sqrt{s_{NN}} = 3.84$ GeV Au+Au collisions with impact parameter $b = 4-8$ fm in the reaction plane ($x-z$ plane) is shown in figure 9.3. The source has an obvious tilt structure relative to the beam axis. We use the parameterization of equation 9.2 to fit the three-dimensional freeze-out distribution for

all pions with $p_T < 400$ MeV/c and $|y| < 0.6$ – not only those at a given angle ϕ. From this direct analysis of the freeze-out coordinates – obviously not possible in experiment– we find the parameters listed in the third column of table 9.1. It is clear from figure 9.3 that the $x - z$ correlation in the freeze-out distribution has a structure that cannot be captured in a single tilt number; indeed, the tilt is scale-dependent, growing as one focuses on the peak of the distribution. This "twist" feature, which has been observed in simulations before [Lisa00c], might be physically interesting and experimentally accessible; we show a more detailed analysis of this effect in and section 11. For the purpose of this chapter, we identify a range of tilts arising from fitting equation 9.2 to the distribution and varying the fit range in coordinate space from 10 fm $< \Delta x, \Delta y, \Delta z <$ 40 fm. This leads to the range shown in the left column of table 9.1.

Dynamics naturally lead to a strong correlation between a particle's final momentum and the freeze-out position; homogeneity regions are naturally reflected in the final state. Figure 9.2 shows homogeneity regions from UrQMD in the $x-y$ plane for particles emitted at three azimuthal angles. The homogeneity region for particles emitted at a given angle ϕ_1 clearly differs from that for particles emitted at $\phi_2 \neq \phi_1$. Thus, in addition to the *explicit* ϕ-dependence of the HBT radii seen in equations 9.6, there is an additional *implicit* dependence [Volo96, Wied98, Heis99a, Heis99b]. HBT radii measured at a given momentum vector (ϕ, p_T, y) probe only the geometry of the homogeneity region for that momentum vector. *A priori*, it is far from clear that equations 9.10, 9.11 and 9.12, which attempt to relate HBT radius oscillations to the geometry of the "whole" source, will prove good approximations.

In the next section, we test these relations – true for the simplest toy model of equation 9.2 – with UrQMD-generated freeze-out distributions.

9.3. HBT radii and anisotropy parameters from UrQMD-generated correlation functions

We start by generating two-pion correlation functions, analogous to those measured experimentally, from UrQMD events. We will then proceed to fit these correlation functions with the Gaussian anzatz of equation 9.1, as is done in experimental analysis. Finally, we extract Fourier coefficients characterizing the oscillations of the HBT radii with angle; from these we extract the source anisotropy parameters that would be obtained in an experiment.

To simulate experimental conditions, two-pion correlation functions were constructed from the UrQMD events using the so-called weighting method. In this method, pairs of identical pions are selected according to a Monte Carlo algorithm; the correlation function in a given (q_o, q_s, q_l) bin is equal to the pair-wise average of the squared two-pion wavefunction. Considering only quantum symmetrization effects, the correlation

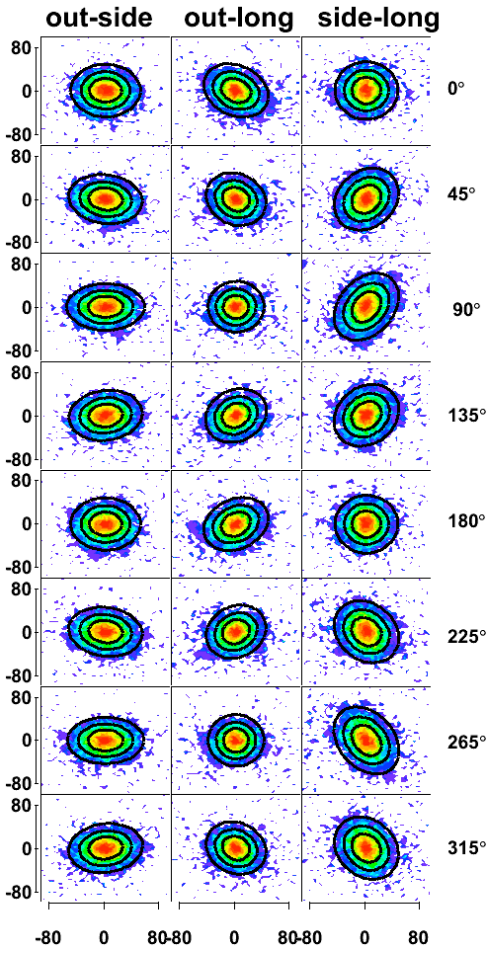

Figure 9.4: Pion correlation functions from Au+Au collisions with collision energy $\sqrt{s_{NN}} = 3.84$ GeV (corresponding to a 6 AGeV beam incident on a fixed target) and impact parameter $b = 4-8$ fm, as calculated with the UrQMD model. Projections in the $q_o - q_s$ (left column), $q_o - q_l$ (middle) and $q_s - q_l$ spaces are made, with the unplotted $\vec{q}$-component smaller than 4 MeV/c. Correlation slices are shown for pion pairs in 45°-wide ϕ bins centered at angles indicated to the right of each row. Shaded contours represent the calculated correlation function. Black contours represent two-dimensional slices of the three-dimensional Gaussian fit to the correlation functions for each selection in ϕ.

function is computed (see A.2.3, here with additional ϕ-binning) as

$$C\left(q_o, q_s, q_l; \phi\right) = \langle 1 + \cos\left(-q^\mu \Delta r_\mu\right)\rangle_\phi, \tag{9.13}$$

where $q = p_1 - p_2$ is the relative momentum and Δr is the space-time separation of the particles at freeze-out.

As explicitly denoted in equation 9.13, the correlation functions were generated for 8 45°-wide bins in pair angle $\phi \equiv \angle(\vec{K}_T, \vec{b})$, where $\vec{K}_T \equiv (\vec{p}_{T,1} + \vec{p}_{T,2})/2$ is the average transverse momentum vector of the pair. Hence, for $-\frac{\pi}{8} < \phi < \frac{\pi}{8}$ ($\frac{5\pi}{8} < \phi < \frac{7\pi}{8}$), pions from sub-region indicated by the black contours in the left (right) panel of figure 9.2 are used to construct the correlation function.

For each bin in ϕ, two-dimensional slices of the three-dimensional correlation function in $q_o - q_s$, $q_s - q_l$ and $q_l - q_o$ are plotted in figure 9.4; in each case the unplotted relative momentum component $q_i < 4$ MeV/c. For a representative ϕ bin, one-dimensional slices

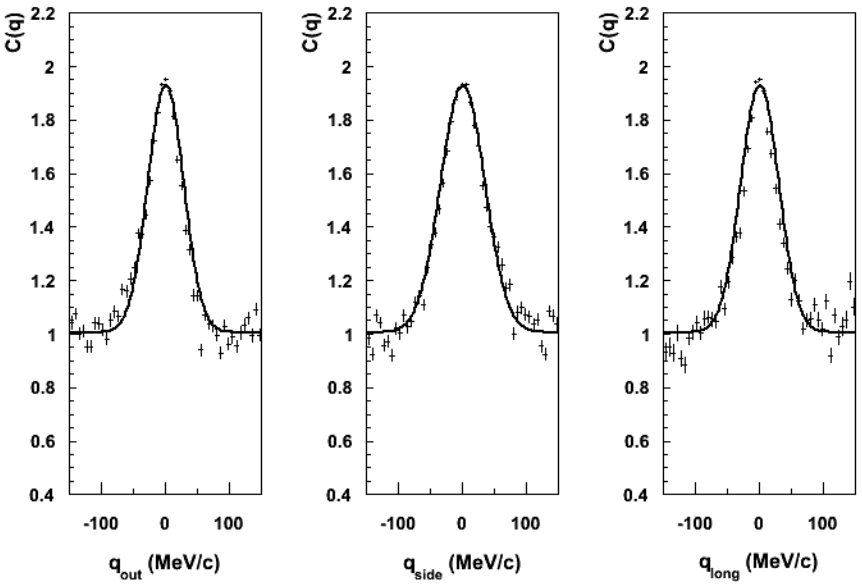

Figure 9.5.: One-dimensional slices in the three components of relative momentum, for pions emitted at $|\phi| < 22.5°$ in Pb+Pb collisions at $\sqrt{s_{NN}} = 3.84$ GeV and $b = 4 - 8$ fm. Curves represent one-dimensional slices of the three-dimensional Gaussian fit to the correlation function.

of the correlation function in the out, side, and long directions are shown in figure 9.5. Most femtoscopic correlation analyses focus on the one-dimensional projections, since the correlation in three-dimensional space factorizes; that is, there is no covariance between components q_i and $q_{j\neq i}$ in the correlation function. This is not the case when the analysis is performed differentially in ϕ [Volo96, Wied98, Heis99a, Heis99b, Lisa00c, Lisa00a, Hein02a], as is clear from the tilted structures in $\vec{q}$-space seen in figure 9.4. These tilts in the individual correlation functions in $\vec{q}$-space for a given angular selection in $\vec{K}$ are not to be confused with the overall spatial tilt of the source sketched in figure 9.1.

As in an experimental analysis, the correlation functions are fitted with the Gaussian functional form of equation 9.1. Two- and one-dimensional slices of these fits are superimposed on the correlation functions in figures 9.4 and 9.5. The six resulting HBT radii are plotted as a function of ϕ on figure 9.6. As in a standard azimuthally-integrated analysis, the "diagonal" radii R_j^2, $j = o, s, l$ are driven by the width of the correlation function in the direction j. The "cross-term" radii $R_{i,j\neq i}^2$ quantify the correlations between $\vec{q}$ components – the tilts of the correlation function; e.g. the ϕ-dependence of the tilt of the correlation function in the $q_s - q_l$ space seen in the right column of figure 9.4 leads directly to the first-order oscillation of R_{sl}^2 seen in figure 9.6. Figure 9.7 shows the radii for $\sqrt{s_{NN}} = 7.7$ GeV collisions.

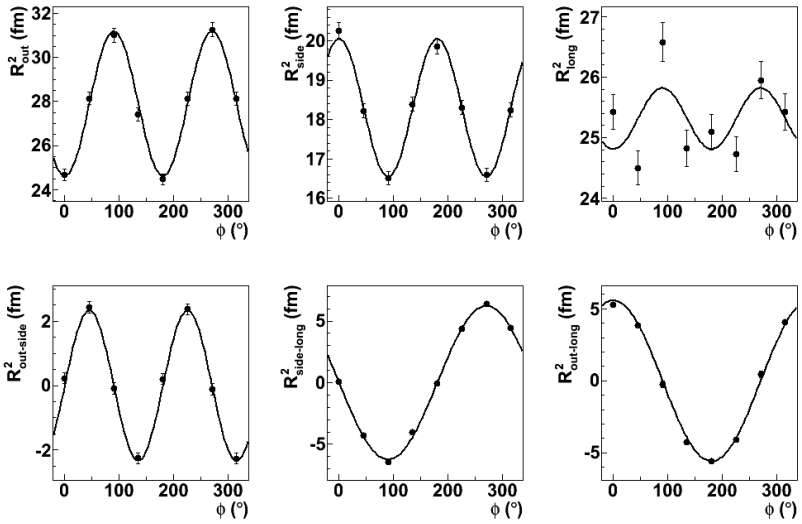

Figure 9.6.: The six HBT radii extracted from Gaussian fits (equation 9.1) to the correlation functions for eight selections on ϕ in Pb+Pb collisions at $\sqrt{s_{NN}} = 3.84$ GeV and $b = 4 - 8$ fm. Curves represent a Fourier decomposition (equation 9.8), including terms up to second-order, where the Fourier components are determined according to equation 9.9. See text for details.

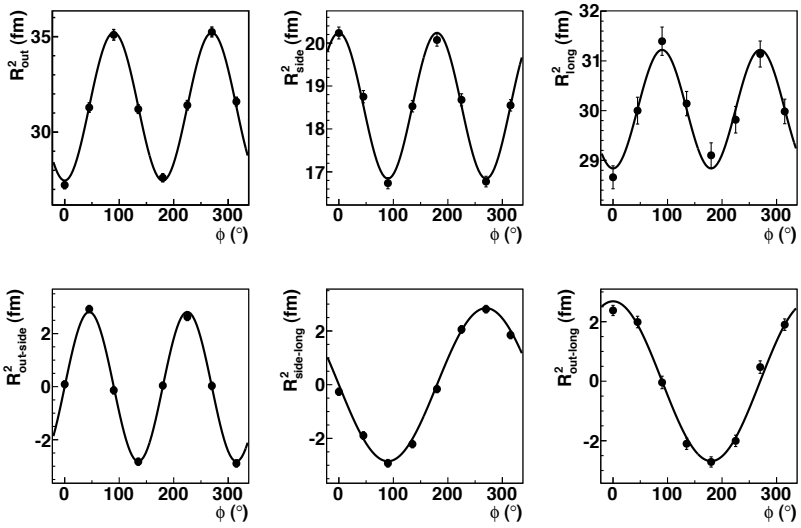

Figure 9.7.: Same as figure 9.6, but for collisions at $\sqrt{s_{NN}} = 7.7$ GeV.

The curves on figures 9.6 and 9.7 represent equations 9.8 using Fourier coefficients $R^2_{\mu,n}$ calculated according to 9.9.

Before we apply equations 9.10-9.12, we note that the argumentation of section 9.1 implicitly assumed that the $R^2_\mu(\phi)$ were measured as a continuous function. In reality, in our analysis as in experiment, the correlation function is measured for ϕ within bins of width $\Delta\phi$. The amplitude of the n^{th}-order oscillation of a binned function is reduced from that of the underlying function. To correct for this finite-binning artifact, we calculate the underlying ("true") Fourier coefficients $\tilde{R}^2_{\mu,n}$ from the ones extracted from the binned radii by

$$\tilde{R}^2_{\mu,n} = \frac{n\Delta\phi/2}{\sin(n\Delta\phi/2)} R^2_{\mu,n}\,. \tag{9.14}$$

For our 45°-wide bins, $\tilde{R}^2_{\mu,1} = 1.026 R^2_{\mu,1}$ and $\tilde{R}^2_{\mu,2} = 1.111 R^2_{\mu,2}$. These binning-corrected Fourier coefficients are used in equations 9.10-9.12. [1]

As in most experimental analyses, the correlation functions from UrQMD simulations are not purely Gaussian, since the source itself is not Gaussian in coordinate space, due to space-momentum correlations (flow), resonance contributions, etc. Of special interest for the present study is the additional fact that the source is not characterized by a tilt angle independent of spatial scale – the "twist" discussed in section 9.2 and more extensively in chapter 11. Following a standard experimental approach [Adam05b], we perform a fit-range study, in which we vary the range in q_o, q_s, q_l, over which we perform the fit with equation 9.1. In particular, we fit the correlation functions in the range $-q_{max} < q_o, q_s, q_l < q_{max}$ for $q_{max} = 60 - 150$ MeV/c. The resulting anisotropy parameters for $\sqrt{s_{NN}} = 3.84$ GeV collisions, calculated according to equations 9.10-9.12, are shown in figure 9.8. The dependence of θ_S on q_{max} is readily understood. Large values of q probe smaller values of coordinate space; thus, as q_{max} is increased, the fit is increasingly sensitive to the large tilt structure seen at small scales in figure 9.3. Figure 9.8, then, is itself a measure of the "twist" structure in coordinate space, though there may be more sophisticated ones. For our purposes, however, we take the variation of the anisotropy parameters plotted in figure 9.8 to define a range of values one might expect from an experimental study. Since a typical experimental analysis would fit at least out to 100 MeV/c (in order to include all of the peak signal), the value ranges listed in the fourth column of table 9.1 correspond to 100 MeV/c $< q_{max} <$ 150 MeV/c.

[1] In principle, one could correct the correlation functions themselves for the finite ϕ-binning, and then extract HBT radii from them, as described in [Hein02a]. However, especially if the reaction-plane estimation resolution [Volo08] is good (in our model analysis, it is perfect), it makes no significant difference whether the correlation functions or the radii themselves are corrected for binning effects [Well02].

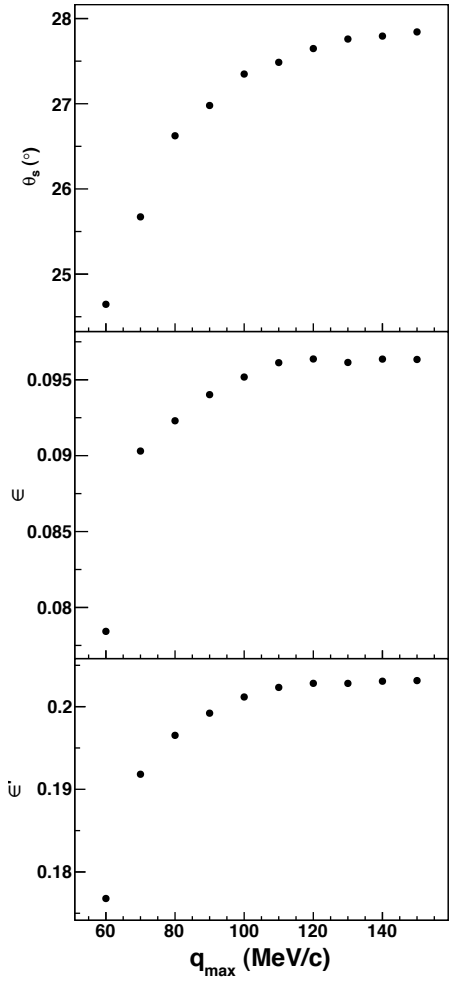

Figure 9.8.: Source anisotropy parameters extracted from two-pion correlation functions for UrQMD-generated Au+Au collisions at $\sqrt{s_{NN}} = 3.84$ GeV at $b = 4 - 8$ fm are plotted as a function of the range in relative momentum over which the correlation functions are fitted. Respectively, top, middle and bottom panels show the source tilt angle θ_S, eccentricity about the beam axis ϵ and eccentricity about the tilted axis ϵ'. See text for details.

The agreement with the parameters extracted via direct analysis of the UrQMD freeze-out coordinates is fair, and we discuss this further in the next section. The fifth column in table 9.1 lists the anisotropy parameters based on HBT radii measured by the E895 collaboration in a fixed-target experiment at $E_{beam} = 6$ AGeV [Lisa00a]. The UrQMD calculation reproduces the tilt angle very well, the eccentricities somewhat less well, though experimental uncertainties are large. UrQMD calculations in the bottom row of the table represent a prediction for collisions at $\sqrt{s_{NN}} = 7.7$ GeV, which will be measured at FAIR and RHIC.

$\sqrt{s_{NN}}$		Direct fit to coordinate space	UrQMD: HBT oscillations	Expt.: HBT oscillations
3.84 GeV	ϵ	$0.13 - 0.17$	$0.095 - 0.096$	0.30 ± 0.15
(6 AGeV)	θ_s	$34° - 41°$	$27.4° - 27.9°$	$26° \pm 7°$
	ϵ'	$0.21 - 0.26$	$0.200 - 0.206$	0.38 ± 0.19
7.7 GeV	ϵ	$0.11 - 0.14$	$0.090 - 0.091$	-
(30 AGeV)	θ_s	$14° - 21°$	$11.7° - 11.9°$	-
	ϵ'	$0.12 - 0.16$	0.109	-

Table 9.1.: Source anisotropy parameters, for Au+Au collisions at two collision energies, with $b = 4 - 8$ fm for pions with $p_T < 0.6$ GeV/c, and $|y| < 0.6$. Impact parameter and momentum cuts were selected to match published data from the E895 collaboration [Lisa00a]. Third column: estimates from a Gaussian fit (equation 9.2) to the freeze-out distribution from UrQMD events. Fourth column: estimates using equations 9.10-9.12 on the azimuthal oscillations of HBT radii from UrQMD events. Fifth column: same as column four, but using experimental data from E895. Experimental data at 7.7 GeV will be analyzed at FAIR and RHIC.

9.4. Discussion

Previous studies [Reti04] of boost-invariant hydrodynamic and blast-wave models found that the eccentricity values estimated from two-particle radii were within 30% of the "true" values; this has been used as a systematic error for the eccentricity in experimental studies [Adam04]. Our results using UrQMD are consistent with this 30% value. The present study is the first estimate of the corresponding uncertainty in the tilt, θ_S; the agreement is somewhat worse, on the order of 35%. Given the complications of dynamically-induced homogeneity regions, a time-evolving emission distribution, non-Gaussianness and "twist" effects, one might easily have expected much worse agreement.

However approximate, quantifying the connection between the radius oscillations and the underlying geometry can be useful. Ideally, the correct model of a heavy-ion collision will reproduce all experimental observations; here, this means the HBT radii and their dependence on azimuthal angle. However, when observations are reproduced and others not, connections to the underlying scenario are important. For example, if a model reproduces R_{long} and R_{side} but over-estimates R_{out} [Soff01, Soff03, Hein02c], attention immediately turns to emission duration, which may be associated with the nature of the transition between confined and deconfined states, latent heat, etc. [Bert89, Prat86, Risc96].

For the azimuthal dependence of HBT radii, the tilt angle and eccentricities probe different aspects of the dynamics. At AGS energies (≈ 3.5 GeV), θ_S reflects the dynamics behind directed flow [Lisa00c] in the earliest stage of the collision and shows strong dependence of the equation of state used in transport calculations [Lisa00a]. Meanwhile,

the eccentricities represent the geometric and temporal [Lisa04] aspects of elliptic flow. It is hoped that the connections we have discussed here between experimental observations and the underlying source anisotropy will help future comparative studies focus on the physics most relevant to each observable.

10. Shape analysis of strongly-interacting systems

This chapter is based on [Lisa11]. We compare anisotropic shape measurements in heavy-ion collisions with similar studies in two other strongly-interacting systems at very different spatial and thermal scales. We discuss the physics associated with anisotropic shapes in these collisions and how these shapes are measured. Several theoretical transport calculations are used to show the sensitivity of the final shape of the source on the underlying physics, and are compared with existing measurements. Particularly interesting is an "anomalous" shape measurement from the CERES collaboration at about $\sqrt{s_{NN}} \approx 20$ GeV, an energy region where several threshold-like behaviours have been reported [Gazd11]. However, the conclusive power of this measurement is minimal, since it is in disagreement with newer data from the RHIC-BES.

10.1. Anisotropic shapes as a probe of three strongly-coupled systems

There is increasing recognition of connections between the physics of ultra-relativistic heavy-ion collisions and other quite different fields. In this section, we briefly discuss three systems of vastly different scales and decidedly distinct physical constituents; these are listed in table 10.1. Despite their differences, they share a striking resemblance. In all cases, a strongly-interacting system is initially prepared in a spatially anisotropic state and then allowed to evolve. The shape at a later time reveals important physics driving the dynamics of the matter.

10.1.1. Anisotropic shape evolution in a cold atomic gas

The first connection to the bulk evolution in heavy-ion collisions and that of cold atomic systems was pointed out several years ago [Kolb03, Shur04]. In particular, in measurements by O'Hara *et al.* [OHar02], a degenerate Fermi gas of ultra-cold ^{6}Li atoms is held in a spatially-anisotropic magnetic trap. The trap is removed, and the shape of the system is measured at a later time; figure 10.1 shows the state of the system at different times after the trap is released. (The measurement of the system shape actually destroys the cold gas, so the panels of figure 10.1 are in reality different gas samples released from identical traps.)

For the system depicted in figure 10.1, a pumping laser has been used to maximize the inter-atom interaction cross-section. Thus, like the ultra-hot partonic system created

system	T (K)	length (m)	time (s)
cold atoms	10^{-6}	10^{-4}	10^{-3}
electrical plasmas in crystals	10^{5}	10^{-7}	10^{-12}
heavy-ion collisions	10^{12}	10^{-15}	10^{-24}

Table 10.1.: Characteristic scales for three strongly-coupled systems. Despite their widely different scales and matter characteristics, their evolution and the methods used to study them are strikingly similar. They are prepared in an anisotropic state, expand hydrodynamically, and their final shape is studied to determine their underlying physical properties.

at RHIC, the ultra-cold degenerate gas is a strongly-coupled quantum fluid, starting from an elongated ellipsoidal configuration and allowed to expand into the surrounding vacuum. As with the QGP at RHIC, the higher pressure gradients along the short direction of the initial shape (horizontal in the figure) lead to a stronger expansion in that direction; with the passage of time, the system becomes more round and after some time (≈ 600 μs in the figure) even reverses the sense of its elongation.

The similarity between these measurements and those of "elliptic flow" in heavy-ion collisions [Volo08] has been noted by others [Kolb03, Shur04]. However, measurements of elliptic flow are restricted to anisotropies in momentum space; a more direct connection is made in space-time. Eleven orders of magnitude smaller and 21 orders faster, the heavy-ion analog is shown in the hydrodynamical calculations of figure 10.1 [Kolb03]. Here, the initial anisotropy of the system is generated by the finite impact parameter of the collision. As with the cold atomic gas, the system rapidly expands preferentially along its shorter axis.

In both systems, the strength of the expansion is driven by pressure gradients which are, in turn, determined by the energy density through the equation of state and thermodynamic state of the system. The inversion of the aspect ratio in the cold gas system, seen about 700 μs after its release, signals a strongly interacting phase, semi-quantitatively understood as a superfluid state [OHar02, Meno02]. For the heavy-ion case, the calculations on the left and right in figure 10.1 begin with identical initial energy distributions; only the EoS is different. If the EoS of a massless gas is assumed (right column), the pressure is large and the expansion rapid. For an EoS featuring a first-order phase transition, the pressure gradients are initially large (in the QGP phase), then very small (as the system passes through the mixed phase) and finally of moderate strength (in the confined phase). Since different regions of the system pass through these phases at different times, the flow pattern is complex. What is clear is that the freeze-out shape in coordinate space is very sensitive both to the EoS of the hot matter of interest, and to the timescale over which its evolution takes place. It is this shape that is extracted by azimuthally-dependent femtoscopic measurements discussed in this chapter.

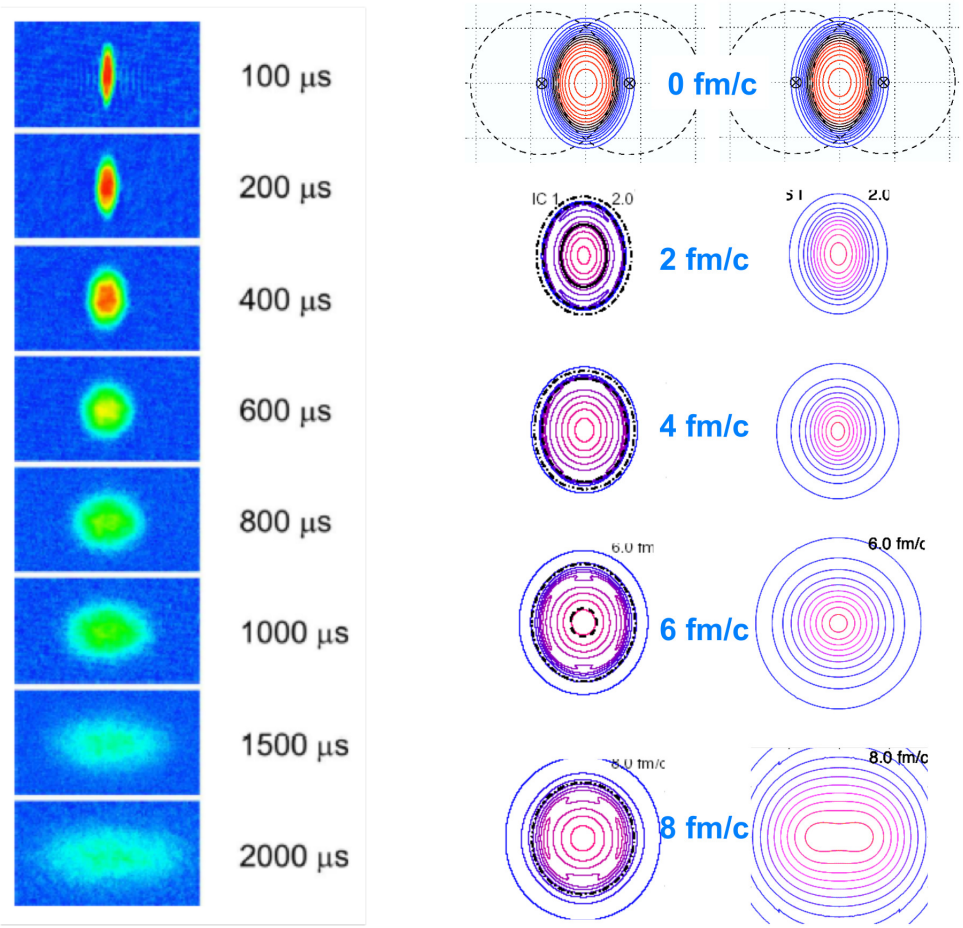

Figure 10.1.: Time evolution of the spatial anisotropy in two strongly-coupled systems. **Left:** A degenerate Fermi gas of ultra-cold Li atoms released from an anisotropic trap. From [OHar02]. **Right:** Hydrodynamical calculation of the evolution of a Au+Au collision at $\sqrt{s_{NN}} = 130$ GeV. Evolution on the right corresponds to an equation of state (EoS) for an ideal massless gas. On the left, the EoS includes a first-order transition between hadronic and QGP phases. From [Kolb03].

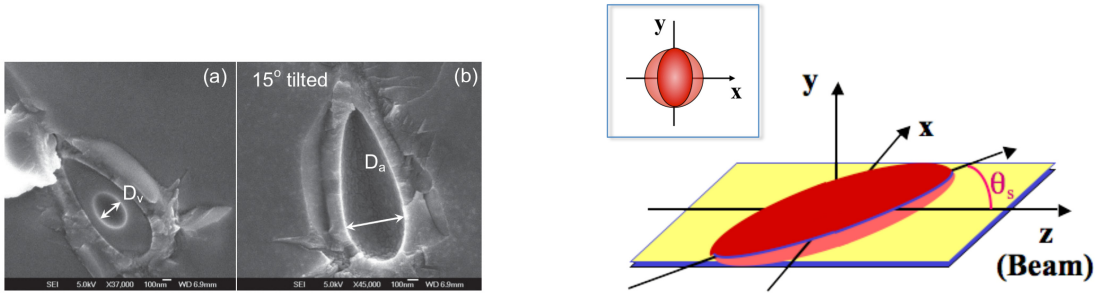

Figure 10.2.: Anisotropic final state of the evolution of dynamic plasmas. **Left:** Scanning electron microscope images of the aftermath of a micro-explosion in sapphire produced by a 150-fs, 100-nJ laser pulse [Juod06]. **Right:** Simplified parameterization of the freeze-out distribution in a heavy-ion collision, as an ellipsoid tilted with respect to the beam axis. **Inset:** Projection of the distribution in the transverse plane.

10.1.2. Anisotropic shape evolution in an electrically-deconfined plasma

Recently, there has been much activity in the study of dynamic condensed matter systems under extreme conditions. This work bears even greater similarity to our study of spatial anisotropies in heavy-ion collisions.

The study of condensed matter systems under extreme pressure has a long history; recently, using diamond anvils, pressures of up to 0.1 TPa (10^6 atm) can be achieved under static conditions in the laboratory, resulting in a surprising diversity of new materials [McMi02]. Exploring even more extreme conditions – 10 TPa or larger – requires explosive generation of a transient system such as are done at the National Ignition Facility [Lind04] or in table-top experiments in which sub-ps laser pulses generate "micro-explosions" under the surface of Sapphire crystals [Juod06] crystals or fused silica [Merm09].

The study of these micro-explosions parallels strikingly the study of femtoexplosions in heavy-ion collisions. In the initial state, the matter is in the charge-confined (atomic) state. Upon rapid deposition of extreme energy density (10^{17} J/m^3), a charge-deconfined plasma is generated within a few fs, at temperatures of $10^5 - 10^6$ K. The plasma expands rapidly ($\sim$ ps), cooling as it does so, and returns to charge-confined degrees of freedom. Plasma hydrodynamics and two-component "blast-wave" pictures [Hall07] are used to describe and understand the source evolution [Juod06].

With huge changes in physical scales and "color charge" replacing "electric charge," the above describes the situation with RHIC collisions rather well, down to the blast-wave parameterizations [Reti04]. In both cases, too, the final-state anisotropy carries impor-

tant physical information. The anisotropic final-state geometry of a micro-explosion is measured directly by a scanning electron microscope; c.f. figure 10.2. In a heavy-ion experiment, it is the final-state momenta that are directly measured, and azimuthally-sensitive two-particle intensity interferometry must be used to measure the coordinate-space geometry.

Since the first proof-of-principle micro-explosion experiments, there has been considerable activity to extract the equation of state of the matter – the plasma state, phase transitions, etc. The approach taken is essentially identical to the one proposed at RHIC: to measure the final-state anisotropy as the initial energy of the system is varied, and compare the results to transport calculations with different EoS.

10.1.3. Anisotropic shape evolution in hot QCD matter

The case on which we shall focus henceforth is the anisotropic evolution of the hot matter generated in the overlap zone of two colliding heavy nuclei; this is indicated in the right panels of figure 10.1. Here, we introduce the anisotropies of interest and the physics driving their evolution. The situation with heavy-ion collisions bears more resemblance to that of the micro-explosions of section 10.1.2 than to the cold atoms discussed in 10.1.1, since the experimenter cannot freely choose the time to measure the system anisotropy. When particles decouple from the medium created in a heavy-ion collision, they are said to "freeze-out." Only the final state of the system – after it has expanded and frozen out – is available for examination; its temporal evolution must be modeled.

The anisotropy of the hot zone in a heavy-ion collision has two sources. Firstly, the beam direction ($\hat{z}$) is clearly special; both in momentum- and coordinate-space, the hot source is extended in $\hat{z}$. Collisions at finite impact parameter break the remaining symmetry in the azimuthal variable around the beam direction. The so-called reaction plane is the plane spanned by the impact parameter (oriented in the $\hat{x}$-direction in this work) and the beam direction. Figure 10.2 shows a plausible if simplistic sketch of the hot matter produced in a non-central heavy-ion collision, containing the minimal set of possible anisotropies– different length scales in each direction, and a tilt of the source away from the beam axis.

Of particular interest is the transverse eccentricity of the source, mentioned already in section 10.1.1. This eccentricity may be quantified by $\epsilon \equiv \left(\sigma_y^2 - \sigma_x^2\right) / \left(\sigma_y^2 + \sigma_x^2\right)$, where $\sigma_{x,y}$ are characteristic scales of the system in and out of the reaction plane, respectively, and will be discussed in more detail shortly. As discussed there, and seen in figure 10.1, the final state eccentricity is determined by both the anisotropic pressure gradient and the system lifetime; increasing either or both of these results in a lower (possibly negative) ϵ.

The other major feature of the freeze-out distribution is the tilt of its major axis, relative to the beam direction. Such tilts are ubiquitously produced in three-dimensional sim-

ulations of heavy-ion collisions. At low energies ($\sqrt{s_{NN}} \approx 4$ GeV), $\theta_s \approx 30°$ [Lisa00a]; its sign discriminated between competing explanations of momentum-space anisotropies for charged pions [Lisa00c].

Generic expectations for the collision energy dependence of freeze-out shapes seem straightforward. The eccentricity, ϵ, is affected by pressure and timescale. One expects both the lifetime and the energy density of the system to increase with increasing $\sqrt{s_{NN}}$. Thus – if the relationship between pressure and energy density (the EoS) remains fixed – it is natural to expect ϵ to decrease monotonically with $\sqrt{s_{NN}}$. The tilt is a manifestly non-boost-invariant aspect of the QGP created in the collision. Directed flow measurements at all energies confirm that the dynamics of heavy-ion collisions are never, strictly speaking, boost invariant. Even the hope that the system is "essentially" boost-invariant at midrapidity may be easily shattered if a finite tilt angle is measured there. Nevertheless, due to the increased elongation of dynamics along the beam direction, it is natural to expect a monotonic decrease of θ_s with $\sqrt{s_{NN}}$ as well.

10.2. Measuring source anisotropy in heavy-ion collisions

In the two parallel cases discussed in section 10.1, the final spatial source anisotropy is measured directly. Of course, the spatial and temporal scales involved in a heavy-ion collision render such measurements impossible. Instead, spatial sizes and shapes are extracted via two-particle femtoscopy [Lisa05]. This technique exploits the connection between the measured two-particle relative momentum correlation function $C(\vec{q})$ and the spatial separation distribution $S(\vec{r})$ as described in chapter 3.

In an azimuthally sensitive femtoscopic study, HBT radii are measured as a function of the pair angle $\phi_p \equiv \angle\left(\vec{K}_T, \vec{b}\right)$ where $\vec{K}_T \equiv \frac{1}{2}(\vec{p}_{T,1} + \vec{p}_{T,2})$. Since the "out" and "side" directions are rotated relative to the x and y directions by ϕ_p, even in the simplest case of figure 10.2 one expects oscillations in the $R^2_{i,j}(\phi_p)$. Indeed, such oscillations in non-central collisions have been clearly observed; figure 10.3 shows HBT radii measured at the lowest ($\sqrt{s_{NN}} = 2.2$ GeV) [Lisa00a] and highest ($\sqrt{s_{NN}} = 200$ GeV) [Adam04] energy collisions explored by these analyses. Suppression of oscillations due to the finite reaction-plane resolution may be corrected for [Hein02a]. Similar to the analysis of momentum flow, Fourier moments of the oscillating radii are extracted.

$$R^2_{\mu,n} = \begin{cases} \langle R^2_\mu(\phi_p)\cos(n\phi_p)\rangle(\mu = o, s, l, ol) \\ \langle R^2_\mu(\phi_p)\sin(n\phi_p)\rangle(\mu = os, sl) \end{cases} . \tag{10.1}$$

Once the Fourier moments of the radii are known, the eccentricity ϵ and the tilt angle θ_s can be determined from equations 3.10 and 3.12.

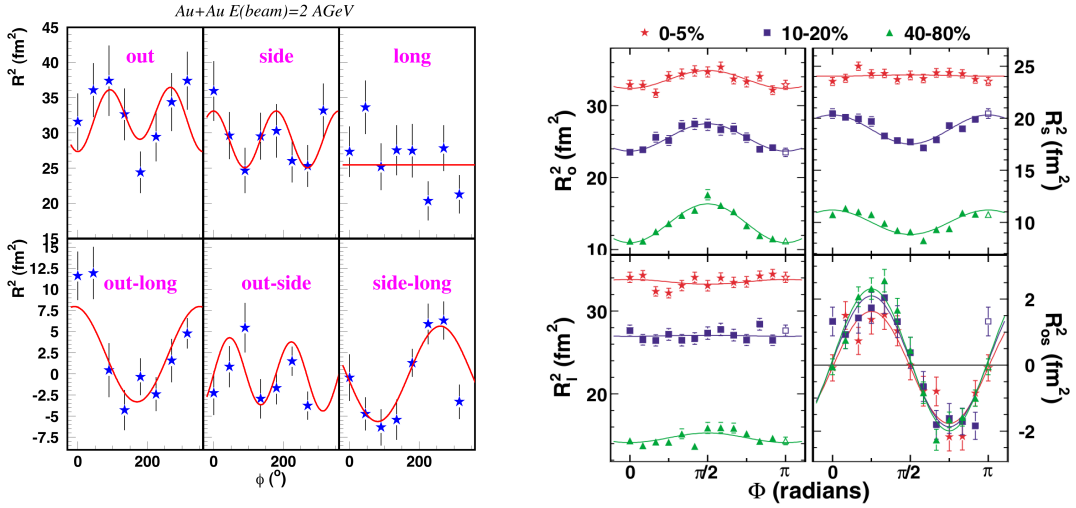

Figure 10.3.: Oscillating HBT radii at the lowest and highest measured energies. **Left:** $\sqrt{s_{NN}} = 2.35$ GeV Au+Au collisions with impact parameter $b \approx 5$ fm. [Lisa00a] **Right:** $\sqrt{s_{NN}} = 200$ GeV Au+Au collisions of varying centrality. From [Adam04].

Additionally,

$$\epsilon' \equiv \frac{\sigma_y^2 - \sigma_{x'}^2}{\sigma_y^2 + \sigma_{x'}^2} = \frac{2R_{s,2}^2\left(1+\cos^2\theta_s\right) + \left(R_{s,0}^2 - R_{l,0}^2\right)\sin^2\theta_s - 2R_{sl,1}^2\sin 2\theta_s}{R_{s,0}^2\left(1+\cos^2\theta_s\right) + \left(2R_{s,2}^2 + R_{l,0}^2\right)\sin^2\theta_s + 2R_{sl,1}^2\sin 2\theta_s}\,, \tag{10.2}$$

allows to determine the transverse eccentricity in the "natural" frame [Moun11] tilted relative to the beam axis to the major axes of the ellipse depicted in figure 10.2.

As suggested in the inset to figure 10.2, $\sigma_{x'} < \sigma_x$ for a simple tilted elongated ellipsoid. Hence, if the final-state emitting source retains its initial out-of-plane extension ($\sigma_y > \sigma_{x'}$), as indicated by measurements so far, the eccentricity measured about the beam axis will be smaller than that measured about the tilted axis: $\epsilon < \epsilon'$.

At low energies, the direction of the impact parameter $\vec{b}$ can be estimated easily, thanks to a relatively strong first-order anisotropy in momentum-space – the so called "directed flow;" in this case, ϕ_p has a meaningful range $[0, 2\pi]$. At RHIC energies, on the other hand, the first-order momentum-space anisotropy is weak, while the second-order momentum-space anisotropy ("elliptic flow") is much easier to measure. Thus, at the higher energies, only the plane that contains $\vec{b}$ is defined, but not the direction of $\vec{b}$ itself; this corresponds, in figure 10.2, to identifying the yellow reaction plane, but not distinguishing $\pm\hat{x}$. In this case, ϕ_p is measured only modulo π and first-order oscillations

like $R^2_{sl,1}$ cannot be measured. Spatial information on the source tilt θ_s and eccentricity in the source's natural coordinate system ϵ' are inaccessible in such analyses. Similarly, two-dimensional transport calculations such as 2+1-dimensional boost-invariant hydrodynamics [Kolb03] are implicitly blind to any tilt structure.

Strong position-momentum correlations, due to collective flow or other sources, imply that pion pairs measured at a given ϕ_p do not sample the entire pion-emitting zone, but only a selected "homogeneity region" [Akke95]. In *principle,* the correspondence between the homogeneity regions and the "whole" source can be almost arbitrary, so that extracting the shape of the latter through measurement of the former is necessarily model dependent. However, studies with reasonable blast-wave parameterizations [Reti04] and realistic transport calculations [Moun11] – both of which feature strong flow and non-trivial correspondence between homogeneity regions and the entire source – indicate that equations 3.10, 3.12 and 10.2 are good to a model-dependent systematic uncertainty of $\approx 30\%$.

10.3. Compilation of experimental results

Until mid of 2011 only three experiments, listed in table 10.2, had published azimuthally-sensitive pion HBT radii. With the progress of the RHIC Beam Energy Scan there are additional data points published [Anso11, Schm12] by the STAR collaboration. All experiments estimated the impact parameter of the collision based on charged particle multiplicity. Since system anisotropy clearly depends on the impact parameter, it is important to compare collisions with similar centrality. In order to best compare results from the $7.4 - 29.7\%$ centrality cut of E895 (corresponding to $b = 4 - 8$ fm), several centrality cuts were combined, for the higher energy measurements.

It is worthwhile to describe in detail how centrality bins were merged, since the comparison between shapes from different collision energies is important for our message. The most relevant centrality bins reported by the STAR Collaboration are for $5 - 10\%$,

Experiment	$\sqrt{s_{NN}}$ (GeV)	centrality (%)	rapidity
AGS/E895 [Lisa00a]	2.35, 3.04, 3.61	(7.4-29.7)	$\|y\| < 0.6$
SPS/CERES [Adam08]	17.3	(7.5-10)⊕(10-15)⊕(15-25) and (10-15)⊕(15-25)	$-1 < y < -0.5$
RHIC/STAR [Adam04]	7.7, 11.5, 19.6 27, 62.4	(5-10)⊕(10-20)⊕(20-30) and (10-20)⊕(20-30)	$\|y\| < 0.5$

Table 10.2.: Measurements of the anisotropic shapes from heavy-ion collisions. The third column indicates which centrality bins were averaged, to obtain the shape parameters of figures 10.4 and 10.5. See text for details.

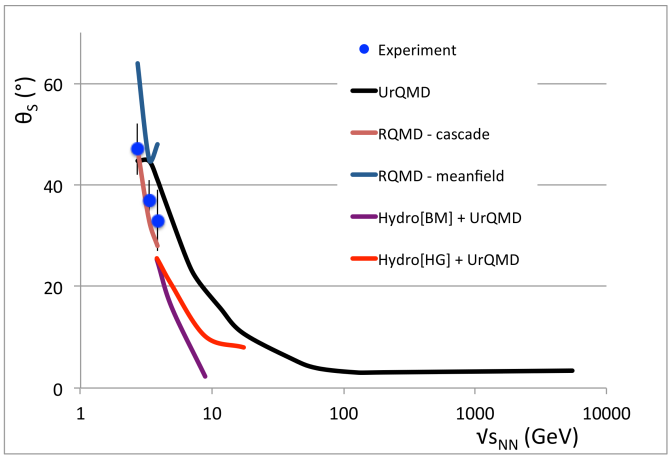

Figure 10.4.: Source tilt relative to the beam direction vs. energy for mid-central heavy-ion collisions. See sections 10.3 and 10.4 for a discussion of the experimental data and model calculations, respectively.

$10-20\%$ and $20-30\%$ of total cross-section. We combine data from these three bins as

$$\epsilon^{\mathrm{STAR}}_{(5-10)\oplus(10-20)\oplus(20-30)} \equiv \frac{1\times\epsilon^{\mathrm{STAR}}_{(5-10)} + 2\times\epsilon^{\mathrm{STAR}}_{(10-20)} + 2\times\epsilon^{\mathrm{STAR}}_{(20-30)}}{1+2+2}. \tag{10.3}$$

Here, the weighting factors (1,2,2) account for the fact that the $5-10\%$ bin contains half the number of events as either of the other two bins listed. This selection includes more central events– in particular, events in the $5-7.4\%$ centrality range– than are included in the E895 cuts. Therefore, the value $\epsilon^{\mathrm{STAR}}_{(5-10)\oplus(10-20)\oplus(20-30)} = 0.081 \pm 0.006$ should be considered a lower bound on the shape compared with E895. An upper bound may be obtained by combining only the two more peripheral bins: $\epsilon^{\mathrm{STAR}}_{(10-20)\oplus(20-30)} = 0.094 \pm 0.007$.

The relevant centrality ranges reported by CERES are $7.5-10\%$, $10-15\%$ and $15-25\%$ of the total cross-section. A fair range to use in our comparison is between $\epsilon^{\mathrm{CERES}}_{(7.5-10)\oplus(10-15)\oplus(15-25)} = 0.035 \pm 0.018$ and $\epsilon^{\mathrm{CERES}}_{(10-15)\oplus(15-25)} = 0.043 \pm 0.020$.
All measurements focused on low-momentum pions ($p_T \approx 0.25$ GeV/c), for which the formulae 3.10, 3.12 and 10.2 work best [Reti04]. STAR and E895 measurements center on midrapidity, where participant contributions should be maximal, while the CERES measurement is somewhat backwards in the center of mass frame. Since HBT measurements typically vary slowly with rapidity, this difference is unlikely to affect CERES' shape estimation, but a measurement at midrapidity would provide a better comparison with the other experiments.

E895 measured HBT radii relative to the first-order event plane (i.e., the direction of the impact parameter); results for $\sqrt{s_{NN}} = 2.35$ GeV are shown on the left panel of figure 10.3. The spatial tilt is shown in figure 10.4. The tilt is strikingly large at these

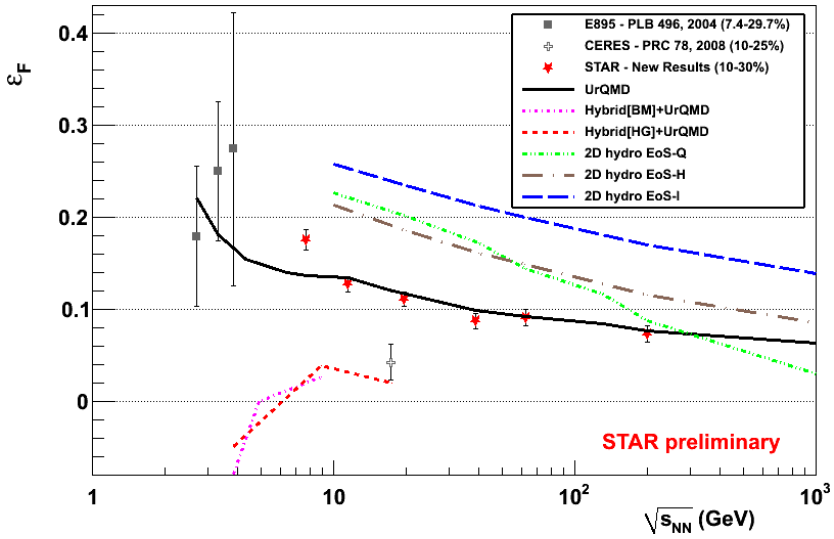

Figure 10.5.: Source eccentricity vs. energy for mid-central heavy-ion collisions. See sections 10.3 and 10.4 for a discussion of the experimental data and model calculations, respectively. Plot taken from [Schm12].

low energies and drops with energy, consistent with the expectation [Bjor83] that collisions become increasingly boost-invariant (at least near midrapidity) with increasing energy. It will be important to extend tilt measurements to higher energies, since a finite θ_s is manifestly "boost-variant," even at $y = 0$. If θ_s is more than a few degrees, boost-invariant models may not be valid and would at least require double-checking with true three-dimensional calculations.

Figure 10.5 shows the measurements from the experiments listed in table 10.2. Filled symbols indicate ϵ, the eccentricity relative to the beam axis (c.f. equation 3.10), while open symbols indicate the eccentricity in the natural frame of the source (equation 10.2), measured only by E895. For the CERES and STAR data points, the average of the upper and lower bounds discussed above are plotted, with the difference between the bounds and the statistical error bars added, to be conservative. Even though the CERES point is in conflict with RHIC data, the non-monotonic behaviour of $\epsilon\left(\sqrt{s_{NN}}\right)$ is still intriguing. As discussed in Section 10.1.3, rather general considerations lead to the expectation of a monotonic decrease of ϵ with energy. The unexpected dip in figure 10.5 occurs in the energy region in which phase transition "threshold" effects have been reported [Gazd11] and around which some speculate that heavy-ion collisions sample the non-trivial features sketched in figure 1.1; c.f [Agga10].

To contribute our own speculation, we note that such non-monotonic behaviour could arise from one of two effects, both related to a first-order phase transition. Firstly, an

extended lifetime due to the transition would allow the system to evolve further towards a round shape (c.f. figure 10.1), causing a dip just around the threshold energy. Using this simplistic scenario to explain the data, the CERES data point at $\sqrt{s_{NN}} \approx 17$ GeV lies near the threshold energy. Alternatively, we may fix the lifetime and consider effects of the stiffness of the EoS, quantified by the speed of sound in the medium, $c_s^2 = \frac{\partial P}{\partial e}$, where P and e are the pressure and energy density, respectively. At low energies, the system is in the hadronic phase, and $c_s^2 \approx \frac{1}{6}$; as $\sqrt{s_{NN}}$ increases, pressure gradients increase in proportion to the energy deposited in the system; here, ϵ would fall with $\sqrt{s_{NN}}$. Near the threshold energy, the system may spend much of its time in the mixed phase, for which $c_s^2 = 0$; here, the system shape would evolve little from its initial, large value. As the energy increased still further, the system spends most of its time in the deconfined plasma phase, for which $c_s^2 \approx 1/3$, and $\epsilon\left(\sqrt{s_{NN}}\right)$ again falls monotonically.

Considering the newer data from the RHIC-BES [Anso11, Schm12] puts doubt on the interpretation of the eccentricity behaviour as a phase transition. There are additional data points for $\sqrt{s_{NN}} = 7.7, 11.5, 19.6, 27$ & 62.4 GeV. All data points follow the cascade UrQMD prediction almost embarrassingly well except the $\sqrt{s_{NN}} = 7.7$ GeV point, which is about 30% above the UrQMD line. This means that the CERES data point at $\sqrt{s_{NN}} \approx 17$ GeV is in disagreement with the STAR data point at $\sqrt{s_{NN}} = 19.6$ GeV. This is a serious threat to the interpretation of the eccentricity behaviour at this energy as a sign for a phase transition, since the exciting non-monotonic behaviour vanishes when ignoring the CERES point.

10.4. Transport model calculations

10.4.1. Two-dimensional boost-invariant hydrodynamics

Here, we use one of the most successful models – AZHYDRO [Kolb00], a (2+1)-dimensional ideal hydrodynamic model. This model uses a common simplifying assumption [Shur80, Bjor83] that the initial conditions and subsequent dynamics are boost-invariant; all interesting physics takes place in the transverse plane. For our purposes, this means that the model assumes a non-tilted source ($\theta_s = 0$), and only ϵ is calculable.

It is by now rather clear that boost-invariant ideal hydrodynamic calculations are invalid at energies below about $\sqrt{s_{NN}} \approx 20$ GeV [Kolb03] as (i) the densities achieved are inconsistent with a zero-mean-free-path approximation, and (ii) the system is not boost-invariant. Nevertheless, we will perform calculations over a wide range of energies, including very low ones, to map the excitation function and explore the EoS dependence of the shape parameters.

In order to extend the model into both the LHC high energy regime as well as low energy heavy-ion collisions, the initialization routine must be tuned to the appropriate collision energies. The initial temperature distribution was parameterized through the initial

transverse entropy profile geometrically using an optical Glauber calculation discussed in [Kolb03].

Within the optical Glauber model calculation, the density of wounded nucleons (N_w) and binary nucleon-nucleon collisions ($N_{\rm bin}$) are estimated in the transverse plane. The total entropy density is then a superposition of the "soft" wounded nucleon density and the "hard" binary collision density, appropriately scaled [Kolb01, Khar01] to match both the charged hadron multiplicity and centrality dependence observed in experiments (25% hard contribution). The multiplicity is simply the momentum integrated particle distribution at a given rapidity y (typically at midrapidity, $y = 0$) [Kolb03, Kolb01]. Furthermore, for consistency, as the initial entropy density (and consequently the initial temperature) changes for each collision, the thermalization time τ_0 is correspondingly changed in order to keep the "uncertainty relationship" ($\tau_0 T_0 \approx 1$) constant [Kolb03, Frod07]. The multiplicity is then matched to the expected charged multiplicity of each collision energy.

For the transition of fluid cells to particles, we use a constant energy density $e = 0.075$ GeV/fm^3 which corresponds to a isotherm which varies depending on the equation of state used to describe the matter. For all equations of state used in these simulations, the freeze-out temperature is $T_f \approx 130$ MeV.

In order to study a range of possible phases of matter, three distinct equations of state were used in the hydrodynamic simulations. These are discussed in [Kolb00] and represent a purely hadronic state of matter (EOS H), a pure quark/gluon gas (EOS I), and a Maxwellian-constructed EOS Q which contains a first-order phase transition between EOS I and EOS H. In [Kolb00], EOS Q was used exclusively to describe the matter created at $\sqrt{s_{NN}} = 130$ GeV.

HBT radii were extracted by fitting projections of two-pion correlation functions, calculated according to the method of [Frod06]. These radii were then used in equation 3.10 to extract the final-state eccentricities shown in figure 10.5. For each EoS used, the eccentricity monotonically decreases as a function of energy, an effect both of increased system lifetime and pressure as $\sqrt{s_{NN}}$ increases, as discussed in section 10.1.3.

There is considerable sensitivity to the EoS used in the calculation. Using the initialization procedure discussed above, use of the stiff equation of state, EoS-I with $c_s^2 = \frac{1}{3}$, results in a much more out-of-plane shape – i.e. one that has not evolved much from the initial overlap shape. The shape evolves considerably more when using the softer EoS-H ($c_s^2 = \frac{1}{6}$). Since for a given energy density pressure gradients are proportional to c_s, these results suggest that effects of system lifetime dominate over those of pressure, in these calculations. This conclusion is consistent with the results when using EoS-Q. These shapes track closely with those of EoS-H for low $\sqrt{s_{NN}}$ where the system is dominated by the hadronic phase. At around $\sqrt{s_{NN}}$, the threshold effect of the "soft" mixed phase ($c_s^2 = 0$) become apparent, increasing the system lifetime and further decreasing ϵ.

It is clear from figure 10.5 that the phase transition is needed to explain the single RHIC data point– at least in this model. Extension of the shape excitation function to higher (LHC) energies will be important to further constrain the EoS. The validity of (2+1)-dimensional models breaks down at these energies, limiting their utility in constraining the EoS with low-energy data.

10.4.2. Microscopic Boltzmann transport

UrQMD is particularly attractive for this study since it is applicable over a broad range of energies.

In addition, we also use an earlier incarnation of this model, Relativistic Quantum Molecular Dynamics (RQMD) [Sorg95] which was widely used over the more limited energy range of the AGS and SPS – $\sqrt{s_{NN}} \approx 3-20$ GeV. It is satisfying to see good consistency between the older and newer versions of the model, in terms of predicted shapes.

For the UrQMD calculations, ϵ, ϵ' and θ_s were extracted by directly fitting the freeze-out distribution with the functional form of equation 3.11. For the older RQMD calculations, the model output was processed through equation 3.2 to generate correlation functions, which were fitted with equation 3.5 to extract HBT radii. These radii were then used to calculate shape parameters according to equations 3.10, 3.12 and 10.2. For these models, the shape parameters extracted using these two methods should be consistent to $\approx 30\%$ [Moun11]. The simulations reproduce the very large tilt angles measured at low $\sqrt{s_{NN}}$ and predict a sharp fall-off with energy. The RQMD model features the possibility to include the effects of a medium-induced mean field on the trajectories of the hadrons during the collision; θ_s is significantly sensitive to this mean-field effect. In particular, the spatial tilt measurements are best described when effects of the mean field are ignored ("cascade mode"). This is interesting in light of the fact that reproducing the *momentum*-space tilt ("directed flow" or v_1 [Volo08]) demands inclusion of mean-field effects [Liu00]. While measurement of spatial shapes already constrain the EoS of hot nuclear matter, combining both coordinate- and momentum-space shapes place even stricter constraints on the dynamics.

The final-state eccentricity, plotted in figure 10.5, reproduces the large ϵ (and ϵ') values measured at the AGS, with little dependence on the nuclear mean field. At SPS energies ($\sqrt{s_{NN}} \approx 17$ GeV), tilt angles on the order of 10° are predicted by UrQMD. This is just about the point at which the effect of the tilt on the measured eccentricity (c.f. inset of figure 10.2) vanishes; i.e. $\epsilon \approx \epsilon'$ for $\sqrt{s_{NN}} > 17$ GeV in this model. The monotonic decrease predicted by the model is not nearly strong enough to reproduce the CERES measurement, but falls rather smoothly to closely approach the shape measured at top RHIC energy. The model predicts closely the more recent RHIC-BES measurements [Anso11, Schm12]. At still higher energies (e.g. LHC), the model predicts a continued out-of-plane final eccentricity with little $\sqrt{s_{NN}}$-dependence.

10.4.3. Hybrid hydrodynamic-Boltzmann calculation

As with the UrQMD calculations discussed in section 10.4.2, shape parameters were extracted from a direct fit of the freeze-out distribution with equation 3.11. Large tilts are again predicted at low collision energies, with significant sensitivity to the EoS used in the calculation. The effect of the first-order phase transition (Hydro[BM]) is clear: At low $\sqrt{s_{NN}}$ even the earliest dense phase of the collision is below threshold to be affected by the phase transition. Thus there is no dependence on the EoS in θ_s at low energies. However, at larger energies, the mixed phase reduces the sideward pressure very early in the system evolution, reducing θ_s compared to a EoS without phase transition. It would be very interesting indeed to measure tilt angles at SPS energies.

That shapes from Hydro[HG]+UrQMD are not identical to those from "pure" UrQMD is at first puzzling, given that the EoS in the hydrodynamic phase is that used in the Boltzmann model. This is likely a technical issue – particles that would be emitted early in the "pure" UrQMD simulation are generally absorbed into the hydro phase in the hybrid model, only to reappear at the iso-eigentime freeze-out hyper-surface. Thus, for now it is best not to compare hybrid calculations to pure Boltzmann simulations, but to compare one hybrid calculation to the other, concluding that the EoS sensitively affects the final-state shape of a heavy-ion collision.

Due to this increased system lifetime, the system eccentricities in the hybrid calculations are allowed to evolve to much lower values than those predicted by UrQMD. Indeed, the system in its natural rotated frame is essentially round transversely ($\epsilon' \approx 0$), so the large tilt can even produce $\epsilon < 0$ – an in-plane extended source, measured about the beam axis; ϵ then grows with $\sqrt{s_{NN}}$ because θ_s decreases. The eccentricity at SPS energy essentially reproduces the CERES result (though challenged by the RHIC-BES data), probably an artifact of the extended lifetime effect discussed above.

11. Measuring a twisted emission geometry

This chapter is based on [Grae13]. In chapter 9, we found tilt of the particle emission zone, in non-central Pb+Pb collisions, away from the beam axis. This tilt depends on the scale at which the freeze-out distribution is measured. In section 11.1 of this chapter, we explain how to extract the substructure of the tilt of the pion freeze-out distribution in the event plane from the spatial freeze-out distribution. We explore this new feature of the source, the twist, not yet measured or discussed extensively in the literature. A parameterization of the twist and aspects of its physical origin are discussed. Section 11.2 suggests a phenomenological approach that allows to measure the twist experimentally via azimuthally sensitive HBT and an example of the results from such an approach.

11.1. Analysis of the pion freeze-out distribution

The anisotropic "almond" shape of the emission zone in the transverse plane created in non-central collisions is discussed extensively in the literature, as it leads to momentum-space anisotropies (elliptic flow) [Olli92]. However, the spatial substructure of the emission region is much richer than its projection onto the transverse plane. The projection onto the reaction plane (even when selecting particles emitted only at midrapidity) is characterized by a nontrivial shape and anisotropies. Transport calculations and three-dimensional hydrodynamic simulations generate distributions characterized by a tilt relative to the beam direction, which has been related to "antiflow" [Brac00, Lisa00c] or a "third component" of flow [Cser99, Cser11]. In the transport calculations, the emission zone to first-order resembles a tilted ellipsoid [Lisa00c], an idealization which is shown in figure 9.1.

As in chapter 9, we parametrize the tilted freeze-out distribution by a three-dimensional Gaussian ellipsoid in space, rotated by the angle θ_S (see figure 9.1) around the y-axis. This is described by equation 9.2. Analyzing the freeze-out distribution in detail (see figure 11.1) reveals that the system is not characterized by one unique tilt angle, but exhibits a complex geometry. While the innermost part is almost aligned to the x-axis ($\theta_S \approx 90°$), the tilt angle is significantly smaller at the outermost part of the distribution.

The source of this structure is seen in figure 11.2. It shows the time evolution of the pion freeze-out distribution (colored surface). The black contours represent the position of the spectators in each time-step, while the vector field depicts the direction of the average velocity at each space-time point. The vector field is split into a directed flow

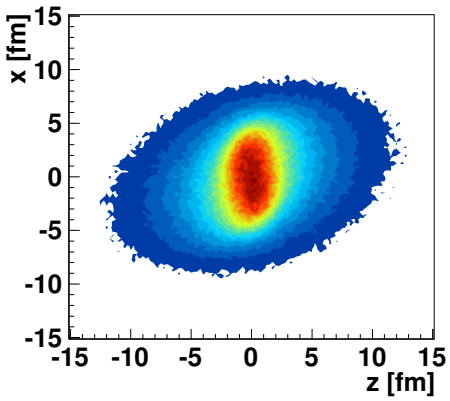

Figure 11.1.: Projection of the pion freeze-out distribution for Pb+Pb at $E_{lab} = 8$ AGeV, $b = 3.4 - 6.8$ fm, $|y| < 0.5$ and $p_\perp < 0.4$ GeV.

(black arrowheads) and an antiflow (magenta arrows) component. To determine whether a given point in space-time is characterized by flow or antiflow, the average pion momentum $\overline{\vec{p}}$ is calculated for each (0.5-fm)^3 cell in the $x - z$ plane. Cells with $\overline{p}_x \cdot \overline{p}_z > 0$ (resp. < 0) are considered to be dominated by flow (resp. antiflow).

From the time evolution it becomes clear that different angles in the tilt structure have their origin at different times of the evolution. In the beginning up to $t \approx 4$ fm/c, only very few particles are emitted without further reinteractions. After that, more particles contribute to the freeze-out. From $t \approx 4$ fm/c to $t \approx 10$ fm/c, the emission pattern is dominated by the fact that the spectator nucleons shadow the emission of particles in their direction. This gives rise to an antiflow [Brac00] since most particles giving a positive contribution to flow are absorbed by the passing target and projectile nucleons. This automatically leads to a backwards tilt in the freeze-out distribution from early times. After $t \approx 10$ fm/c the spectators have moved on, so they no longer shadow the emission. At this point, about 1/3 of pion emission has occurred (see insets in figure 11.2). The momentum and spatial anisotropies evolve differently in the absence of the shadowing influence, leading to a time-dependent tilt angle. This pattern imprints itself onto the time-integrated freeze-out distribution (figure 11.1) as a scale-dependent tilt angle – the twist. It is the time-integrated freeze-out distribution that is experimentally accessible via HBT measurements, so any experimental sensitivity to the time evolution of the tilt is through this twist.

To underscore the importance of exploring this twist, we point out that even at the later stages of emission (final panels of figure 11.2), the antiflow component in the regions far from the retreating spectators is as strong as the flow component in the other regions. Thus, there are *two components to antiflow* in these collisions: shadowing effects in the early stage and preferential spatial expansion along the short axis of the distribution in the later stage. This latter component is the analog to the more familiar pressure-

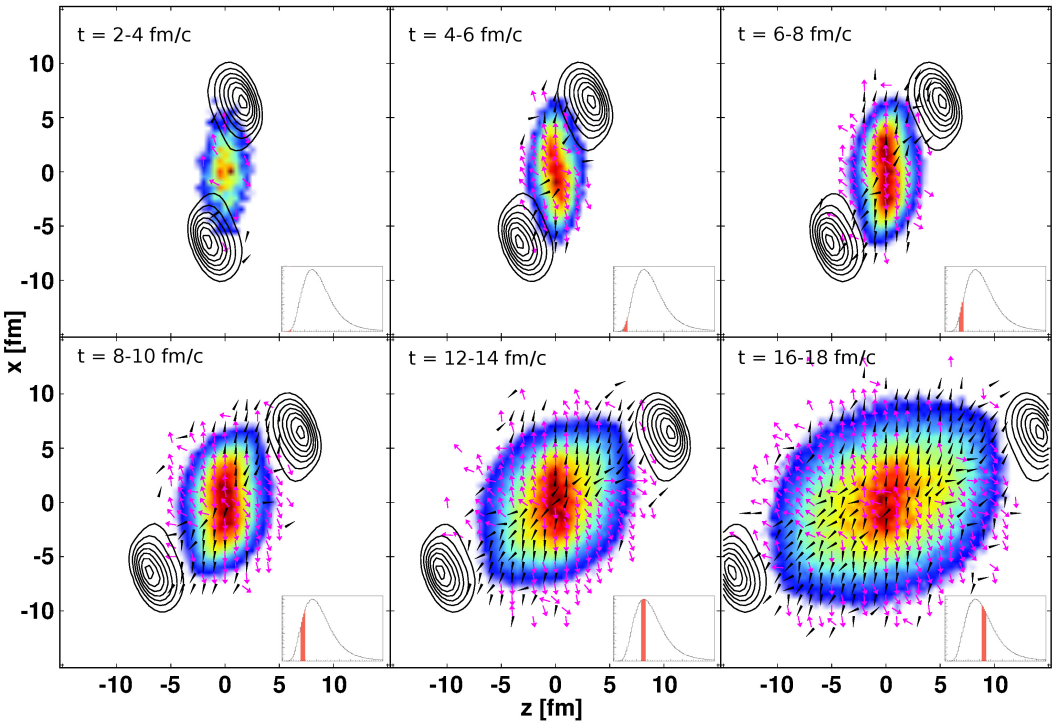

Figure 11.2.: Shape of the freeze-out region from pions frozen out at different times (colored surface). The contour lines depict the position of the spectators in each time-step. The vector field shows the direction of movement at each position and time. The black arrowheads contribute to the directed flow while the magenta arrows contribute to the antiflow. The inlay shows the freeze-out luminosity of pions versus freeze-out time. The shaded region in the inlay highlights the luminosity corresponding to the time-step in the overall picture.

gradient-driven elliptic flow in the $x-y$ plane. The interplay between flow and the two sources of antiflow is complex, presumably energy-dependent, and may be crucial for understanding the details of v_1 measurements.

In most hydrodynamical modeling of elliptic flow, an anisotropic initial state is generated by some (often ad-hoc) mechanism, and then the system responds according to pressure gradients, equation of state, etc. In full transport calculations like UrQMD, there turns out to be at best an approximate factorization into two stages – the deposition of energy into the transverse plane at midrapidity, and the reaction of the system to the initial-state distribution. However, such a factorization is manifestly impossible when considering patterns in the $x-z$ plane, where the source is evolving violently even as it emits particles. Understanding v_1 and similar measurements requires a much more detailed understanding of the space-time evolution of anisotropic structures.

To explore this pattern quantitatively, we fit different parts of the distribution separately, by defining equidistant (2 fm) rings in the $x-z$ plane around the collision center. Then we perform separate fits for each section of the freeze-out distribution taking into account only the part of the distribution between two adjacent rings. The y-direction is unrestricted for these fits. The results of this procedure are shown in figures 11.3 and 11.4. In figure 11.3, the red contours are the pion freeze-out distribution for Pb+Pb at $E_{lab} = 8$ AGeV, $|y| < 0.5$, $p_\perp^\pi < 400$ MeV. The angle of the black line represents the result for $\theta_S(r)$ from the separated fitting, while its length describes the outer limit for the currently applied fit.

In figure 11.4 the results for the tilt angle of these fits are presented versus the radius of the fitted segment (red triangles). To characterize the source effectively we chose to parametrize the $\theta_S(r)$-dependence on r by

$$\theta_S(r) = \theta_0 + \theta_{Mag} \exp\left(-\frac{r^2}{2\sigma_{twist}^2}\right). \tag{11.1}$$

Inserting equation 11.1 into equation 9.2, we gain a new expression for the freeze-out distribution, now with a radius-dependent $\theta_S(r)$. The black contours figure 11.3 represent the projection of the three-dimensional fit of the parametrized freeze-out distribution to the actual freeze-out distribution from UrQMD. It describes the overall shape reasonably well and provides a good description of the tilt angle. The black line in figure 11.4 shows the functional dependence of $\theta_S(r)$ extracted from equation 11.1 using the values for the parameters obtained from the full three-dimensional fit.

11.2. Tilt and twist from azimuthally sensitive HBT calculation

The drawback of the procedure described in Section 11.1 is that it is not possible to measure the spatial freeze-out distribution directly in experiment. If it were possible to measure the twist, this would put additional constraints on many theoretical models.

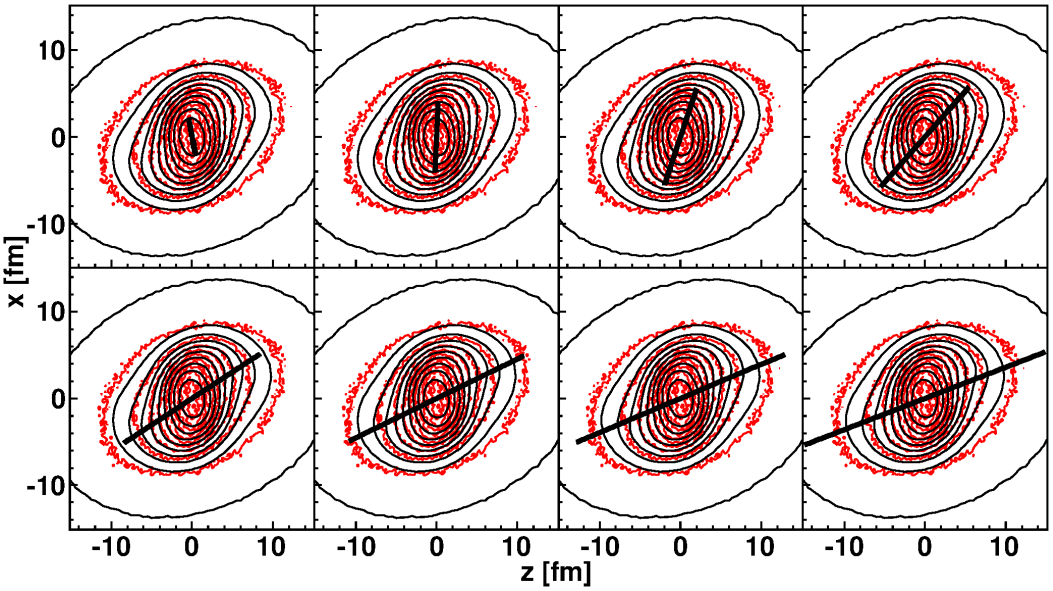

Figure 11.3.: Fit to the pion freeze-out distribution for Pb+Pb at $E_{lab} = 8$ AGeV, $b = 3.4 - 6.8$ fm, $|y| < 0.5$ and $p_\perp < 0.4$ GeV. The red contour is the actual freeze-out distribution from UrQMD. The black contour represent the three-dimensional fit to the whole freeze-out distribution. The black lines represent the fit results for the sphere shells. Their angle represents the fitted angle, while their length represents the radius of the fit sphere.

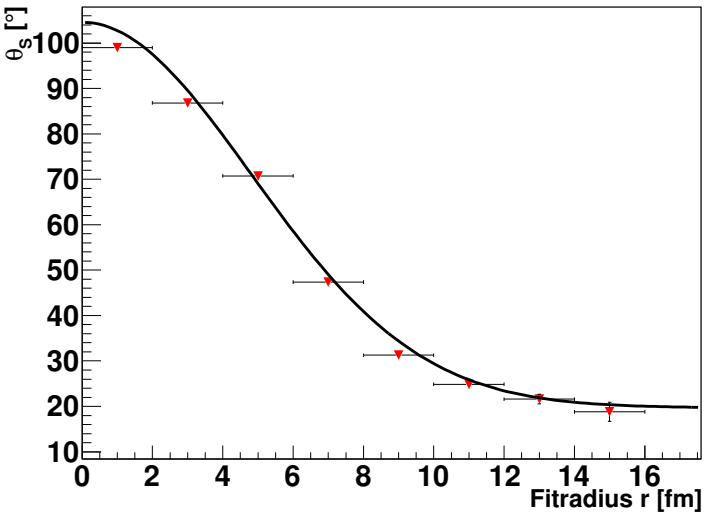

Figure 11.4.: Radius dependence of the tilt angle for the fits with rings (red triangles) and for the full 3D-fit with a radius dependent $\theta_S(r)$ (black line). The system is Pb+Pb at $E_{lab} = 8$ AGeV, $b = 3.4 - 6.8$ fm, $|y| < 0.5$ and $p_\perp < 400$ MeV.

We propose to employ azimuthally sensitive HBT [Lisa00a, Moun11, Lisa11, Lisa00c] in a restricted momentum range to measure the tilt experimentally. Let us briefly outline the procedure to measure θ_S (independent of r) via HBT.

As usual the correlation function is calculated using equation 3.3

$$C(\mathbf{q},\mathbf{K}) = \mathbf{1} + \int \mathbf{d^4x} \cos(\mathbf{q}\cdot\mathbf{x})\mathbf{d}(\mathbf{x},\mathbf{K}) \tag{11.2}$$

where C is the correlation function, q is the four-momentum difference of the correlated particles, $K = (p_1 + p_2)/2$ is the pair momentum, x is the particle separation four-vector and d is the normalized pion freeze-out separation distribution. For the azimuthally sensitive analysis of the HBT correlations, the momentum space is subdivided in several azimuthal sections around the beam axis. For each of the sections an individual correlation function is computed. The azimuthal angle of the pair momentum vector determines in which correlation function each pion pair is counted.
Each of the correlation functions is then fitted separately with

$$C(\mathbf{q},\mathbf{K}) = \mathbf{1} + \lambda(\mathbf{K}) \exp\left[- \sum_{\mathbf{i,j=o,s,l}} \mathbf{q_i q_j R^2_{ij}}(\mathbf{K}) \right], \tag{11.3}$$

to obtain the HBT radii R_{ij}. For non-central collisions this leads to HBT radii oscillating with the azimuthal angle ϕ. Doing a fourier decomposition, it is possible to extract θ_S for low momentum pairs using

$$\theta_S = \frac{1}{2}\tan^{-1}\left(\frac{-4R^2_{sl,1}}{R^2_{l,0} - R^2_{s,0} + 2R^2_{s,2}}\right), \tag{11.4}$$

where in $R_{\nu,\mu}$ the μ denotes the order of the fourier coefficient, e.g. $R_{s,2}$ is the second-order fourier coefficient of the R_s parameter. Details on this method and on finite bin width corrections can be found in [Wied99] and chapter 9. While equation 11.4 allows us to experimentally determine θ_S, it does not give us any information on the r-dependence of $\theta_S(r)$ and it is not clear how to generalize the derivation of equation 11.4 to a r dependent θ_S. Thus we resorted to a phenomenological way to determine the twist.

It was already noticed in chapter 9 that the twist in the freeze-out distribution leads to a rising θ_S with the fit range of the correlation functions.This correlation can be attributed to the fact that larger/smaller values of q are sensitive to smaller/larger structures in coordinate space. To get a $\theta_S(r)$ we exploit this behaviour by applying the same procedure described in Section 11.1 for the freeze-out distribution in coordinate space, now to the correlation function in momentum space. Namely, we generate correlation functions for eight 45°-wide bins in ϕ to do the azimuthal HBT analysis. We then define equidistant sphere surfaces in momentum space around the origin and do the azimuthal HBT analysis needed for θ_S in equation 11.4 for each sphere shell between two adjacent sphere surfaces separately. As a result of this procedure we obtain a $\theta_S(q)$. The result

for Pb+Pb, $E_{lab} = 8$ AGeV, $b = 3.4 - 6.8$ fm, $|y| < 0.6$ and $p_\perp < 0.4$ GeV is shown as red triangles in figure 11.5 versus q_{fit}, where q_{fit} is the middle radius of each sphere shell.

Indeed, figure 11.4 and figure 11.5 do bear a striking similarity if one keeps in mind that larger q values mean sensitivity to smaller regions of homogeneity and vice versa. In figure 11.6, we compare the results of both methods (see figures 11.4 and 11.5) in a single figure. The symbols show $\theta_S(q)$ versus 1/q (blue circles) and $\theta_S(r)$ versus r (red triangles). It is clear that a simple $r \sim 1/q$, as done for the plot, reflects the relation between the spatial extension of the source and the region of homogeneity only qualitatively (there might be some other proportionality factor that depends on the flow and temperature). Nevertheless it clearly indicates that the momentum bin differential azimuthally sensitive HBT allows to capture the complicated source structure. Let us now compare the calculations to the expectations obtained from equations 9.2 and 11.1. The dashed black line in figure 11.6 is a fit of equation 11.1 to $\theta_S(1/q)$. The description of the theoretical data points is very good and leads to θ_{Mag} and θ_0 of both methods being similar to each other.

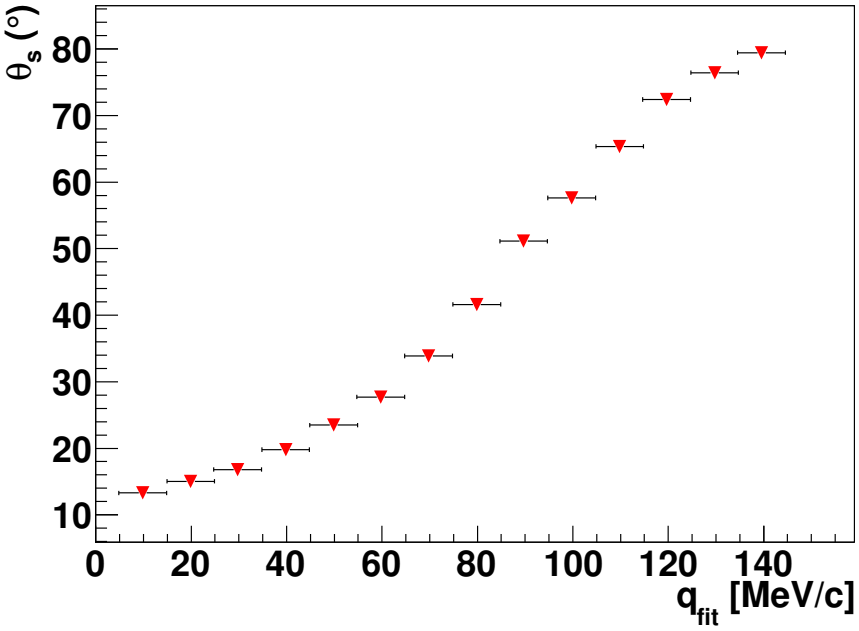

Figure 11.5.: Results for $\theta_S(q)$ plotted versus q_{fit}, where q_{fit} denotes the q segment of the correlation function that is fitted. The investigated system is Pb+Pb at $E_{lab} = 8$ AGeV, $b = 3.4 - 6.8$ fm, $|y| < 0.5$ and $p_\perp < 400$ MeV.

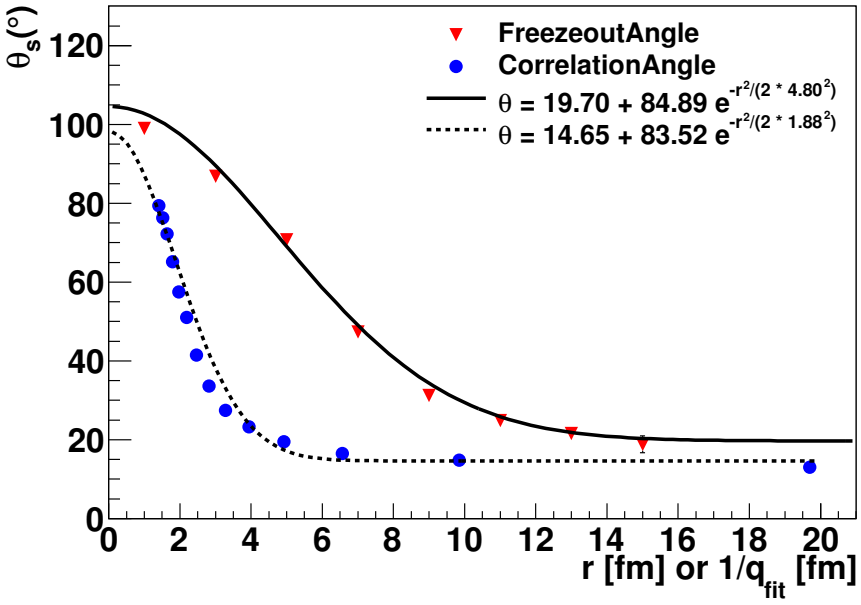

Figure 11.6.: θ_S extracted via fits to the freeze-out distribution (red triangles) and via fits to the HBT correlation functions (blue circles). The x-axis shows the fit radius r for the freeze-out distribution and the inverse of the momentum fit range $1/q_{fit}$ for the correlation functions. The dashed black line is a fit of equation 11.1 to θ_S from the correlation function. The full black line is also equation 11.1 but using the parameters of a fully three-dimensional fit to the freeze-out distribution with equation 9.2 using the r-dependent $\theta_S(r)$.

12. Summary

The main focus of this thesis is to explore temporal and geometric properties of heavy-ion collisions via HBT correlations using the UrQMD model.

First, rapidity and pseudorapidity distributions in elementary collisions and heavy-ion collisions from AGS up to LHC and Tevatron energies have been studied in the UrQMD model. The model performs well describing these basic observables over the whole energy range where data is available.

After this, the main part of the thesis, addressing HBT correlations, begins. An analysis of p+p collisions at $\sqrt{s} = 7$ TeV shows that UrQMD underpredicts the charged particle multiplicity dependence of the HBT radii in this system. This is attributed to the absence of preformed hadron interactions in the model. The values of the HBT radii versus $K_\perp$ depend significantly on the formation time used in UrQMD. Using this fact and comparing to data, the formation time is constrained to be smaller than 0.8 fm/c in this framework.

Investigating central ($\sigma/\sigma_T < 5\%$) Pb+Pb collisions at the LHC energy $\sqrt{s_{NN}} = 2.76$ TeV with UrQMD R_O, R_S and R_L have been extracted. The study reveals a similar $K_\perp$ dependence, both in experiment and from the model. However, R_O andR_L at this energy are overpredicted, while R_S is nicely reproduced. Thus, also the R_O/R_S ratio data is overshot. Further investigations, including the experimentally inaccessible freeze-out distribution, showed that the discrepancy in R_O can be cured if the source lifetime is reduced by a factor of $\approx 2-3$. Still, R_L is not influenced by the reduced lifetime since it is computed in the LCMS. A more violent expansion in the early phase would lead to a reduced lifetime of the system. At the same time it would create smaller regions of homogeneity, also influencing the R_L parameter. Again, the inclusion of preformed hadron interactions in the model would lead to a more violent expansion.

In the light of recent LHC data on p+p and A+A collisions, which indicate a modification of the multiplicity scaling of the HBT radii, the N_{ch} scaling for a large variety of systems and energies has been explored. A good scaling of the HBT radii with $dN_{ch}/d\eta$ within a given system and energy is found. At the same time the radii decrease slightly with increasing beam energy for a fixed $dN_{ch}/d\eta$. This is attributed to a change in the chemical composition of the system for each energy. For the radii, as well as the volume, the slope of the scaling in p+p collisions differs strongly from the A+A results. This is related to the differing particle emission patterns (bulk vs. strings) in A+A and p+p.

The high multiplicities in heavy-ion collisions at LHC energies allow to perform an event-by-event HBT analysis. The EbE-HBT results are used to gauge the extent of volume fluctuations present in heavy-ion collisions. By relating the fluctuations to the isothermal compressibility κ_T it is possible to calculate κ_T using only measurable quantities. Using UrQMD to perform a quasi-experimental analysis yields a value of $\kappa_T = 1.09 \pm 0.47 \frac{\text{MeV}}{\text{fm}^3}$ in head-on collisions and $\kappa_T = 1.02 \pm 0.51 \frac{\text{MeV}}{\text{fm}^3}$ in the 5% most central collisions. Even though the error on κ_T is about 50%, a measurement would provide strong constraints for models if a similar accuracy could be reached in experiment using this method.

Going from central to non-central collisions breaks the azimuthal symmetry about the beam axis. This opens up the field for observables related to azimuthal asymmetries, the final state eccentricity ϵ_f and a tilt angle θ_S of the source away from the beam axis. The oscillations of the HBT radii in an azimuthally sensitive HBT (asHBT) analysis are directly related to ϵ_f and θ_S in the case of a Gaussian source with no space-momentum correlations. Applying this analysis to a more realistic freeze-out distribution generated by UrQMD shows that these relations also hold approximately in this more complex case. ϵ_f and θ_S extracted by a fit to the freeze-out distribution differ only slightly from the values obtained via the asHBT analysis. The good agreement is actually surprising given that the presence of flow breaks the analytic relations and that the tilt has a scale dependence, visible by naked eye.

Studying the energy dependence of θ_S and ϵ_f reveals several things. First of all, θ_S decreases with increasing beam energy, leading to a negligible θ_S above $\sqrt{s_{NN}} \approx 17$ GeV. Secondly, ϵ_f also decreases with increasing beam energy in UrQMD cascade mode, which is to be expected. On the experimental side there is a non-monotonic behaviour in the energy dependence of ϵ_f reported from the CERES collaboration. This could be related to the onset of a phase transition at this energy. However, this behaviour has not been confirmed by more recent measurements during the RHIC-BES that are in disagreement with the CERES measurement and show a monotonic decrease of ϵ_f.

The other important finding about the tilt is its scale dependence, or "twist". The twist originates from antiflow and shadowing of pion emission at early times and the absence of shadowing at later times. The spatial twist is experimentally accessible via asHBT. Using the fact that pairs with small momentum difference are sensitive to large space-time structures and vice versa we calculated the tilt angle on different scales. The analysis shows that this procedure provides a qualitatively accurate picture of the radius dependence of the tilted freeze-out distribution. For the first time, this analysis makes it possible to disentangle the geometry of the source from different times up to a certain point. The twist structure is in principle accessible by experimental HBT analysis and may allow to gain complementary insights into the early emission stages of the reaction. Since the signal vanishes at high energies, the twist is probably best observed at FAIR energies.

In conclusion this thesis covered the standard integrated HBT analyses, extracting the Pratt-Bertsch radii, at LHC energies. The analyses at theses energies showed a too soft expansion in UrQMD probably related to the absence of a partonic phase in UrQMD. The most promising results in this thesis at these energies are the restriction of the formation time to $\tau_f < 0.8$ fm/c and the "mock-measurement" of the isothermal compressibility to a value of $\kappa_T \approx 1 \frac{\text{MeV}}{\text{fm}^3}$. In simulations of non-central heavy-ion collisions at energies of $E_{lab} = 6, 8$ and 30 AGeV the validity of the formulae to calculate θ_s via HBT has been checked numerically, even for the case of non-Gaussian, flowing sources. On this basis a method has been developed and tested in the course of this thesis to measure a scale dependent $\theta_s(r)$. The signal of a $\theta_s(r)$ should be strongest at FAIR energies.

A. Important HBT formulae

A.1. Two-particle wavefunction for identical bosons

The symmetrized wavefunction ψ_{12} for two bosonic particles emitted from position x_i with momentum p_i and detected at position x_i' has the form

$$\psi_{12} = \frac{1}{\sqrt{2}}\left[e^{ip_1(x_1'-x_1)}e^{ip_2(x_2'-x_2)} + e^{ip_2(x_2'-x_1)}e^{ip_1(x_1'-x_2)}\right] \quad . \tag{A.1}$$

From this wavefunction the two-particle probability follows as

$$\begin{aligned}
|\psi_{12}|^2 &= \frac{1}{2}\left|e^{ip_1(x_1'-x_1)}e^{ip_2(x_2'-x_2)} + e^{ip_2(x_2'-x_1)}e^{ip_1(x_1'-x_2)}\right|^2 \\
&= \frac{1}{2}\left[e^{ip_1(x_1'-x_1)}e^{ip_2(x_2'-x_2)} + e^{ip_2(x_2'-x_1)}e^{ip_1(x_1'-x_2)}\right] \\
&\quad \times \left[e^{-ip_1(x_1'-x_1)}e^{-ip_2(x_2'-x_2)} + e^{-ip_2(x_2'-x_1)}e^{-ip_1(x_1'-x_2)}\right] \\
&= \left[1 + \cos(p_1(x_1'-x_1) + p_2(x_2'-x_2) - p_2(x_2'-x_1) - p_1(x_1'-x_2))\right] \\
&= \left[1 + \cos(q\Delta x)\right]
\end{aligned} \tag{A.2}$$

where $\Delta x = x_1 - x_2$ and $q = p_1 - p_2$.

A.2. Relation of radii to distributions

A.2.1. Smoothness approximation

The smoothness approximation assumes that the momentum distribution is sufficiently smooth to write

$$\begin{aligned}
S(x_1,p_1)S(x_2,p_2) &= S(x_1, K - \tfrac{1}{2}q)S(x_2, K + \tfrac{1}{2}q) \\
&\approx S(x_1,K)S(x_2,K) \quad .
\end{aligned} \tag{A.3}$$

A.2.2. The mass-shell constraint

The mass-shell constraint eliminates one component in the HBT analysis and thus prevents a model independent measurement of the space and time extension of particle

emitting sources.

$$\begin{aligned} q_\mu \beta^\mu &= \frac{(p_1 - p_2)_\mu (p_1 + p_2)^\mu}{2K_0} \\ &= \frac{p_1^2 - p_2^2}{2K_0} \\ &= \frac{m_1^2 - m_2^2}{2K_0} \\ &= 0 \end{aligned} \tag{A.4}$$

Where $\beta = K/K_0$ and $K = (p_1 + p_2)/2$.

$$q_\mu \beta^\mu = q^0 \frac{K^0}{K^0} - \vec{\beta} \cdot \vec{q} \tag{A.5}$$

Combining equations A.4 and A.5 leads to

$$\begin{aligned} q^0 &= \vec{\beta} \cdot \vec{q} \\ &= \beta_{out} q_{out} + \beta_{long} q_{long} \end{aligned} \tag{A.6}$$

A.2.3. Relative distance distribution

The correlation function for a source extended in space can be obtained by integrating over the phase space distributions $S(p, x)$ and the two-particle wavefunction.

$$C(q, K) = \frac{\int d^4x_1 d^4x_2 S(p_1, x_1) S(p_2, x_2) |\psi_{12}|^2}{\int d^4x_1 d^4x_2 S(p_1, x_1) S(p_2, x_2)} \tag{A.7}$$

Combining equation A.2 and A.7, one obtains

$$\begin{aligned} C(q, K) &= \frac{\int d^4x_1 d^4x_2 S(p_1, x_1) S(p_2, x_2)(1 + \cos(\Delta x \cdot q))}{\int d^4x_1 d^4x_2 S(p_1, x_1) S(p_2, x_2)} \\ &= 1 + \frac{\int d^4r d^4\Delta x S(p_1, r + \frac{\Delta x}{2}) S(p_2, r - \frac{\Delta x}{2}) \cos(\Delta x \cdot q)}{\int d^4r d^4\Delta x S(p_1, r + \frac{\Delta x}{2}) S(p_2, r - \frac{\Delta x}{2})} \\ &\overset{\text{eqn.}A.3}{=} 1 + \frac{\int d^4r d^4\Delta x S(K, r + \frac{\Delta x}{2}) S(K, r - \frac{\Delta x}{2}) \cos(\Delta x \cdot q)}{\int d^4r d^4\Delta x S(K, r + \frac{\Delta x}{2}) S(K, r - \frac{\Delta x}{2})} \\ &\overset{\text{eqn.}A.9}{=} 1 + \int d^4\Delta x S_{dist}(K, \Delta x) \cos(\Delta x \cdot q) \\ &= 1 + \langle \cos(\Delta x \cdot q) \rangle_{dist} \\ &\overset{\text{eqn.}A.6}{=} 1 + \langle \cos([\beta_o q_o + \beta_l q_l]\Delta t - \Delta x_o q_o - \Delta x_s q_s - \Delta x_l q_l) \rangle_{dist} . \end{aligned} \tag{A.8}$$

Here $\langle \cos(\Delta x \cdot q) \rangle_{dist}$ is the average with respect to the relative distance distribution $S_{dist}(K, \Delta x)$.

$$S_{dist}(K, \Delta x) = \frac{\int d^4r S(K, r + \frac{\Delta x}{2}) S(K, r - \frac{\Delta x}{2})}{\int d^4r d^4\Delta x S(K, r + \frac{\Delta x}{2}) S(K, r - \frac{\Delta x}{2})} \tag{A.9}$$

A.2.4. Gaussian parametrization

One often assumes the phase space distribution $S(p,x)$ to be gaussian.

$$S(p,x) = S(p)e^{-\frac{x_\mu x_\nu}{2R^2_{\mu\nu}}} \tag{A.10}$$

This allows to extract the HBT radii $R_{\mu\nu}$ from the correlation function and to relate them to the phase space distribution. $R_{\mu\nu}$ is a symmetric matrix.

$$\begin{aligned}
C(q,K) &= \frac{\int d^4x_1 d^4x_2 S(p_1,x_1)S(p_2,x_2)(1+\cos(\Delta x\cdot q))}{\int d^4x_1 d^4x_2 S(p_1,x_1)S(p_2,x_2)} \\
&= 1 + \frac{\int d^4r d^4\Delta x S(p_1, r+\frac{\Delta x}{2})S(p_2, r-\frac{\Delta x}{2})\cos(\Delta x\cdot q)}{\int d^4r d^4\Delta x S(p_1, r+\frac{\Delta x}{2})S(p_2, r-\frac{\Delta x}{2})} \\
&= 1 + \frac{\int d^4r d^4\Delta x S(p_1)S(p_2) e^{-\frac{(r+\frac{\Delta x}{2})_\mu (r+\frac{\Delta x}{2})_\nu}{2R^2_{\mu\nu}}} e^{-\frac{(r-\frac{\Delta x}{2})_\mu (r-\frac{\Delta x}{2})_\nu}{2R^2_{\mu\nu}}} \cos(\Delta x\cdot q)}{\int d^4r d^4\Delta x S(p_1,x_1)S(p_2,x_2)} \\
&= 1 + \frac{\int d^4r d^4\Delta x S(p_1)S(p_2) e^{-\frac{r_\mu r_\nu + \frac{\Delta x_\mu x_\nu}{4}}{R^2_{\mu\nu}}} \cos(\Delta x\cdot q)}{\int d^4r d^4\Delta x S(p_1,x_1)S(p_2,x_2)} \\
&= 1 + \frac{\int d^4r d^4\Delta x S(p_1)S(p_2) e^{-\frac{r_\mu r_\nu + \frac{\Delta x_\mu \Delta x_\nu}{4}}{R^2_{\mu\nu}}} e^{-i\Delta x\cdot q}}{\int d^4r d^4\Delta x S(p_1,x_1)S(p_2,x_2)} \\
&= 1 + \frac{\int d^4\Delta x S(p_1) e^{-\frac{\Delta x_\mu \Delta x_\nu}{4R^2_{\mu\nu}}} e^{-i\Delta x\cdot q}}{\int d^4\Delta x S(p_1,x_1)} \\
&= 1 + \frac{\int d^4\Delta x S(p_1) e^{-\left(\frac{\Delta x_\mu}{2R_{\mu\nu}} + iq_\mu R^{\mu\nu}\right)\left(\frac{\Delta x_\nu}{2R_{\mu\nu}} + iq_\nu R^{\mu\nu}\right) - q_\mu q_\nu R^{\mu\nu 2}}}{\int d^4\Delta x S(p_1,x_1)} \\
&= 1 + e^{-q_\mu q_\nu R^{\mu\nu 2}}
\end{aligned} \tag{A.11}$$

When going from chaotic to partially coherent emission equation A.11, changes to [Wied99]

$$C(q,K) = 1 + \lambda e^{-q_\mu q_\nu R^{\mu\nu 2}} \ , \tag{A.12}$$

where λ is the chaoticity parameter, which is a number between zero and one and decreases with increasing coherence.

A.2.5. Radii and variances

To get the relation between the HBT radii and the space-time extension of the source, let us take a look at the curvature of the correlation function at zero

$$\left.\frac{\partial^2 C(q,K)}{\partial q_\mu \partial q_\nu}\right|_{q=0} \ . \tag{A.13}$$

If we determine the curvature in the gaussian case from equation A.11, we get

$$\begin{aligned} -\left.\frac{\partial^2 C(q,K)}{\partial q^\mu \partial q^\nu}\right|_{q=0} &= -\frac{\partial^2}{\partial q^\mu \partial q^\nu}\left[1+e^{-q_\epsilon q_\lambda R^{\epsilon\lambda 2}}\right]_{q=0} \\ &= \frac{\partial}{\partial q^\mu}\left[\left(\frac{\partial q_\lambda}{\partial q^\nu}q_\epsilon + \frac{\partial q_\epsilon}{\partial q^\nu}q_\lambda\right) R^{\epsilon\lambda 2} e^{-q_\epsilon q_\lambda R^{\epsilon\lambda 2}}\right]_{q=0} \\ &= \left[\frac{\partial q_\lambda}{\partial q^\mu}\frac{\partial q_\epsilon}{\partial q^\nu} + \frac{\partial q_\epsilon}{\partial q^\mu}\frac{\partial q_\lambda}{\partial q^\nu}\right] R^{\lambda\epsilon 2} e^{-q_\epsilon q_\lambda R^{\epsilon\lambda 2}}\Big|_{q=0} \\ &= \left(g_{\mu\lambda}g_{\nu\epsilon} + g_{\nu\lambda}g_{\mu\epsilon}\right) R^{\epsilon\lambda 2} \\ &= 2R^2_{\mu\nu} \end{aligned} \tag{A.14}$$

At the same time we can use equation A.8 to determine the curvature

$$\left.\frac{\partial^2 C(q,K)}{\partial q^\mu \partial q^\nu}\right|_{q=0} = \left.\frac{\partial^2}{\partial q^\mu \partial q^\nu}\left\langle \cos([\beta_o q_o + \beta_l q_l]\Delta t - \Delta x_o q_o - \Delta x_s q_s - \Delta x_l q_l)\right\rangle_{dist}\right|_{q=0} \tag{A.15}$$

For the out-out case this leads to

$$-\left.\frac{\partial^2 C(q,K)}{\partial q^o \partial q^o}\right|_{q=0} = \left\langle (\Delta x_o - \beta_o \Delta t)^2 \right\rangle_{dist} \tag{A.16}$$

$$= 2\left\langle (\Delta x_o - \beta_o \Delta t)^2 \right\rangle \quad . \tag{A.17}$$

The factor two that appears from equation A.16 to A.17 comes from the transition of the average with respect to the distance distribution to the average with respect to the spatial distribution. In the gaussian case considered here the difference between two normal distributed variables is again a normal distribution with a width added quadratically from the original distributions.

Combining equations A.14 and A.17 relates the HBT radii to the time and space distributions of the frozen out particles like follows.

$$R^2_o = \left\langle (\Delta x_o - \beta_o \Delta t)^2 \right\rangle \tag{A.18}$$

$$R^2_s = \left\langle \Delta x_s^2 \right\rangle \tag{A.19}$$

$$R^2_l = \left\langle (\Delta x_l - \beta_l \Delta t)^2 \right\rangle \tag{A.20}$$

$$R^2_{os} = \left\langle (\Delta x_o - \beta_o \Delta t)\Delta x_s \right\rangle \tag{A.21}$$

$$R^2_{ol} = \left\langle (\Delta x_o - \beta_o \Delta t)(\Delta x_l - \beta_l \Delta t) \right\rangle \tag{A.22}$$

$$R^2_{sl} = \left\langle (\Delta x_l - \beta_l \Delta t)\Delta x_s \right\rangle \tag{A.23}$$

A.3. Azimuthal sensitive HBT

Azimuthal sensitive HBT stands for a HBT analysis that is differential in the angle around the beam axis. Let us define the angle Φ as the angle between pair momentum

vector K and the impact parameter vector $\vec{b}$. This allows to rewrite equations A.18 - A.23 in a rotated coordinate system for every pair. Closely following [Wied98] one can write the coordinate transformation as

$$\mathcal{D}_\Phi \vec{\beta} = \begin{pmatrix} \beta_o \\ 0 \\ \beta_l \end{pmatrix}, \mathcal{D}_\Phi \vec{x} = \begin{pmatrix} x\cos\Phi + y\sin\Phi \\ -x\sin\Phi + y\cos\Phi \\ z \end{pmatrix} , \tag{A.24}$$

which leads to the following relations for the radii:

$$\begin{aligned} R_o^2 &= \left\langle \Delta x^2 \right\rangle \cos^2\Phi + \left\langle \Delta y^2 \right\rangle \sin^2\Phi + \left\langle \Delta t^2 \right\rangle \beta_o^2 \\ &\quad + \langle \Delta x \Delta y \rangle \sin 2\Phi - 2\beta_o \langle \Delta y \Delta t \rangle \sin\Phi - 2\beta_o \langle \Delta x \Delta t \rangle \cos\Phi \\ R_s^2 &= \left\langle \Delta x^2 \right\rangle \sin^2\Phi - \langle \Delta x \Delta y \rangle \sin 2\Phi + \left\langle \Delta y^2 \right\rangle \cos^2\Phi \\ R_l^2 &= \left\langle (\Delta z - \beta_l \Delta t)^2 \right\rangle \\ R_{os}^2 &= \frac{1}{2}\left\langle \Delta y^2 \right\rangle \sin 2\Phi - \frac{1}{2}\left\langle \Delta x^2 \right\rangle \sin 2\Phi \\ &\quad + \langle \Delta x \Delta y \rangle \cos 2\Phi + \langle \Delta t \Delta x \rangle \beta_o \sin\Phi - \langle \Delta y \Delta t \rangle \beta_o \cos\Phi \\ R_{ol}^2 &= \langle (\Delta z - \beta_l \Delta t)(\Delta x \cos\Phi + \Delta y \sin\Phi - \beta_o \Delta t) \rangle \\ R_{sl}^2 &= \langle (\Delta z - \beta_l \Delta t)(\Delta y \cos\Phi - \Delta x \sin\Phi) \rangle \quad . \end{aligned} \tag{A.25}$$

A.3.1. Tilt angle

Using the symmetries present in collisions of equal mass nuclei at midrapidity one can show [Hein02a, Lisa00c] that all off-diagonal terms of the space time variances except $\langle \Delta x \Delta z \rangle$ oscillate symmetrically around zero. This simplifies equations A.25 to

$$\begin{aligned} R_o^2 &= \frac{1}{2}\left(\left\langle \Delta x^2 \right\rangle + \left\langle \Delta y^2 \right\rangle\right) + \frac{1}{2}\left(\left\langle \Delta y^2 \right\rangle - \left\langle \Delta x^2 \right\rangle\right)\cos 2\Phi + \beta_o^2 \left\langle \Delta t^2 \right\rangle \\ R_s^2 &= \frac{1}{2}\left(\left\langle \Delta x^2 \right\rangle + \left\langle \Delta y^2 \right\rangle\right) + \frac{1}{2}\left(\left\langle \Delta y^2 \right\rangle - \left\langle \Delta x^2 \right\rangle\right)\cos 2\Phi \\ R_l^2 &= \left\langle \Delta z^2 \right\rangle + \beta_l^2 \left\langle \Delta t^2 \right\rangle \\ R_{os}^2 &= \frac{1}{2}\sin 2\Phi \left(\left\langle \Delta y^2 \right\rangle - \left\langle \Delta x^2 \right\rangle\right) \\ R_{ol}^2 &= \langle \Delta x \Delta z \rangle \cos\Phi \\ R_{sl}^2 &= -\langle \Delta x \Delta z \rangle \sin\Phi \quad . \end{aligned} \tag{A.26}$$

The tensor $B_{\mu\nu}$ holding the space time variances takes the form

$$B = \begin{pmatrix} \Delta t^2 & 0 & 0 & 0 \\ 0 & \Delta x^2 & 0 & \Delta x \Delta z \\ 0 & 0 & \Delta y^2 & 0 \\ 0 & \Delta x \Delta z & 0 & \Delta z^2 \end{pmatrix} \quad . \tag{A.27}$$

B can be brought into a diagonal form by calculating $J^{-1}BJ$, where J is

$$J = \begin{pmatrix} 1 & 0 & 0 & 0 \\ 0 & \Delta x & 0 & -\Delta z \\ 0 & 0 & 1 & 0 \\ 0 & \Delta z & 0 & \Delta x \end{pmatrix} \quad . \tag{A.28}$$

If one identifies J with the four-dimensional rotation matrix $D_y(\theta)$ that describes a rotation around the y-axis

$$D_y(\theta) = \begin{pmatrix} 1 & 0 & 0 & 0 \\ 0 & \cos\theta & 0 & \sin\theta \\ 0 & 0 & 1 & 0 \\ 0 & -\sin\theta & 0 & \cos\theta \end{pmatrix} \quad , \tag{A.29}$$

one finds the relation $\tan\theta = -\frac{\Delta z}{\Delta x}$. This relation can be rewritten as

$$\theta = \frac{1}{2}\tan^{-1}\left(\frac{2\Delta x \Delta z}{\Delta z^2 - \Delta x^2}\right) \tag{A.30}$$

using elementary trigonometric identities. Further details can be found in [Lisa00c].

In an experimental analysis of azimuthal sensitive HBT the radii parameters are usually expanded into a fourier series in the following way

$$\begin{aligned} R_o^2(\Phi) &= R_{o,0}^2 + 2\sum_{n=2,4,6,\ldots} R_{o,n}^2 \cos(n\Phi) \\ R_s^2(\Phi) &= R_{s,0}^2 + 2\sum_{n=2,4,6,\ldots} R_{s,n}^2 \cos(n\Phi) \\ R_l^2(\Phi) &= R_{l,0}^2 + 2\sum_{n=2,4,6,\ldots} R_{l,n}^2 \cos(n\Phi) \\ R_{os}^2(\Phi) &= 2\sum_{n=2,4,6,\ldots} R_{os,n}^2 \sin n\Phi \\ R_{ol}^2(\Phi) &= 2\sum_{n=1,3,5,\ldots} R_{ol,n}^2 \cos n\Phi \\ R_{sl}^2(\Phi) &= 2\sum_{n=1,3,5,\ldots} R_{sl,n}^2 \sin n\Phi \quad . \end{aligned} \tag{A.31}$$

With this and using the longitudinal comoving system ($\beta_l = 0$) equation A.30, can be rewritten in terms of fourier coefficients of the HBT parameters [Moun11].

$$\theta = \frac{1}{2}\tan^{-1}\left(\frac{-4R_{sl,1}^2}{R_{l,0}^2 - R_{s,0}^2 + 2R_{s,2}^2}\right) \tag{A.32}$$

A.3.2. Eccentricity

The transverse spatial eccentricity ϵ in heavy-ion collisions is defined as

$$\epsilon = \frac{\langle \Delta y^2 \rangle - \langle \Delta x^2 \rangle}{\langle \Delta x^2 \rangle + \langle \Delta y^2 \rangle} \tag{A.33}$$

using equations A.26 and A.31 the eccentricity can be expressed in terms of the fourier coefficients of the HBT radii as

$$\epsilon = 2\frac{R_{s,2}^2}{R_{s,0}^2} \quad . \tag{A.34}$$

B. Bibliography

[Aad10] Aad, G. and others: *Charged-particle multiplicities in pp interactions at $\sqrt{s} = 900$ GeV measured with the ATLAS detector at the LHC.* Phys.Lett., B688:21–42, 2010, [arXiv: 1003.3124].

[Aad12] Aad, Georges and others: *Measurement of the centrality dependence of the charged particle pseudorapidity distribution in lead-lead collisions at $\sqrt{s_{NN}} = 2.76$ TeV with the ATLAS detector.* Phys.Lett., B710:363–382, 2012, [arXiv: 1108.6027].

[Aamo11a] Aamodt, K. et al.: *Femtoscopy of pp collisions at $\sqrt{s} = 0.9$ and 7 TeV at the LHC with two-pion Bose-Einstein correlations.* Phys.Rev., D84:112004, 2011, [arXiv: 1101.3665].

[Aamo11b] Aamodt, K. et al: *Two-pion Bose-Einstein correlations in central Pb-Pb collisions at sqrt($s_N N$) = 2.76 TeV.* Phys.Lett., B696:328–337, 2011, [arXiv: 1012.4035].

[Abe90] Abe, F. et al.: *Pseudorapidity distributions of charged particles produced in $\bar{p}p$ interactions at $\sqrt{s} = 630$ GeV and 1800 GeV.* Phys.Rev., D41:2330, 1990.

[Abel09a] Abelev, B.I. et al.: *Pion Interferometry in Au+Au and Cu+Cu Collisions at RHIC.* Phys.Rev., C80:024905, 2009, [arXiv: 0903.1296].

[Abel09b] Abelev, B.I. et al.: *Systematic Measurements of Identified Particle Spectra in pp, d^+ Au and Au+Au Collisions from STAR.* Phys.Rev., C79:034909, 2009, [arXiv: 0808.2041].

[Abel12] Abelev, B. et al.: *Charged kaon femtoscopic correlations in pp collisions at $\sqrt{s} = 7$ TeV.* 2012, [arXiv: 1212.5958].

[Abre02] Abreu, M.C. et al.: *Scaling of charged particle multiplicity in Pb Pb collisions at SPS energies.* Phys.Lett., B530:43–55, 2002.

[Abre08] Abreu, S. et al.: *Heavy Ion Collisions at the LHC - Last Call for Predictions.* J.Phys., G35:054001, 2008, [arXiv: 0711.0974].

[Adam03a] Adamova, D. et al.: *Beam energy and centrality dependence of two pion Bose-Einstein correlations at SPS energies.* Nucl.Phys., A714:124–144, 2003, [arXiv: nucl-ex/0207005].

[Adam03b] Adamova, D. et al.: *Enhanced production of low-mass electron pairs in 40-A-GeV Pb Au collisions at the CERN SPS.* Phys. Rev. Lett., 91:042301, 2003, [arXiv: nucl-ex/0209024].

[Adam03c] Adamova, D. et al.: *Universal pion freezeout in heavy ion collisions.* Phys.Rev.Lett., 90:022301, 2003, [arXiv: nucl-ex/0207008].

[Adam04] Adams, J. et al.: *Azimuthally sensitive HBT in Au + Au collisions at s(NN)**(1/2) = 200-GeV.* Phys.Rev.Lett., 93:012301, 2004, [arXiv: nucl-ex/0312009].

[Adam05a] Adams, J. et al.: *Azimuthal anisotropy in Au+Au collisions at s(NN)**(1/2) = 200-GeV.* Phys.Rev., C72:014904, 2005, [arXiv: nucl-ex/0409033].

[Adam05b] Adams, J. et al: *Pion interferometry in Au+Au collisions at S(NN)**(1/2) = 200-GeV.* Phys.Rev., C71:044906, 2005, [arXiv: nucl-ex/0411036].

[Adam05c] Adams, John et al.: *Experimental and theoretical challenges in the search for the quark gluon plasma: The STAR collaboration's critical assessment of the evidence from RHIC collisions.* Nucl. Phys., A757:102–183, 2005, [arXiv: nucl-ex/0501009].

[Adam08] Adamova, D. et al.: *Azimuthal dependence of pion source radii in Pb+Au collisions at 158-A-GeV.* Phys.Rev., C78:064901, 2008, [arXiv: 0805.2484].

[Adco05] Adcox, K. et al.: *Formation of dense partonic matter in relativistic nucleus nucleus collisions at RHIC: Experimental evaluation by the PHENIX collaboration.* Nucl. Phys., A757:184–283, 2005, [arXiv: nucl-ex/0410003].

[Afan02] Afanasiev, S. V. et al.: *Energy dependence of pion and kaon production in central Pb + Pb collisions.* Phys. Rev., C66:054902, 2002, [arXiv: nucl-ex/0205002].

[Agak07] Agakichiev, G. et al.: *Dielectron production in C-12 + C-12 collisions at 2-AGeV with HADES.* Phys. Rev. Lett., 98:052302, 2007, [arXiv: nucl-ex/0608031].

[Agga10] Aggarwal, M.M. et al.: *An Experimental Exploration of the QCD Phase Diagram: The Search for the Critical Point and the Onset of Deconfinement.* 2010, [arXiv: 1007.2613].

[Agga11] Aggarwal, M.M. et al.: *Pion femtoscopy in p^+p collisions at $\sqrt{s} = 200$ GeV.* Phys.Rev., C83:064905, 2011, [arXiv: 1004.0925].

[Ahle00] Ahle, L. et al.: *An excitation function of K- and K+ production in Au + Au reactions at the AGS.* Phys. Lett., B490:53–60, 2000, [arXiv: nucl-ex/0008010].

[Akke95] Akkelin, S.V. and Yu.M. Sinyukov: *The HBT interferometry of expanding sources.* Phys.Lett., B356:525–530, 1995.

[Akke04] Akkelin, S.V. and Yu.M. Sinyukov: *Phase-space densities and effects of resonance decays in a hydrodynamic approach to heavy ion collisions.* Phys.Rev., C70:064901, 2004, [arXiv: nucl-th/0310036].

[Akke06] Akkelin, S.V. and Yu.M. Sinyukov: *HBT search for new states of matter in A+A collisions.* Phys.Rev., C73:034908, 2006, [arXiv: nucl-th/0505045].

[Alex93] Alexopoulos, T. et al.: *A Study of source size in p anti-p collisions at s**(1/2) = 1.8-TeV using pion interferometry.* Phys.Rev., D48:1931–1942, 1993.

[Alne87] Alner, G.J. et al.: *UA5: A general study of proton-antiproton physics at $\sqrt{s}$ = 546-GeV.* Phys.Rept., 154:247–383, 1987.

[Alt06] Alt, C. et al.: *Energy and centrality dependence of anti-p and p production and the anti-Lambda/anti-p ratio in Pb+Pb collisions between 20/A-GeV and 158/A-Gev.* Phys. Rev., C73:044910, 2006.

[Alt08a] Alt, C. et al.: *Bose-Einstein correlations of pi-pi- pairs in central Pb+Pb collisions at A-20, A-30, A-40, A-80, and A-158 GeV.* Phys.Rev., C77:064908, 2008, [arXiv: 0709.4507].

[Alt08b] Alt, C. et al.: *Pion and kaon production in central Pb + Pb collisions at 20-A and 30-A-GeV: Evidence for the onset of deconfinement.* Phys.Rev., C77:024903, 2008, [arXiv: 0710.0118].

[Alve09] Alver, B. et al.: *System size, energy and centrality dependence of pseudorapidity distributions of charged particles in relativistic heavy ion collisions.* Phys.Rev.Lett., 102:142301, 2009, [arXiv: 0709.4008].

[Ande83a] Andersson, Bo, G. Gustafson, G. Ingelman and T. Sjostrand: *Parton Fragmentation and String Dynamics.* Phys.Rept., 97:31–145, 1983.

[Ande83b] Andersson, Bo, G. Gustafson and B. Soderberg: *A General Model for Jet Fragmentation.* Z.Phys., C20:317, 1983.

[Andr05] Andronic, A. et al.: *Excitation function of elliptic flow in Au + Au collisions and the nuclear matter equation of state.* Phys. Lett., B612:173–180, 2005, [arXiv: nucl-ex/0411024].

[Anso11] Anson, Christopher: *Energy dependence of the freeze out eccentricity from the azimuthal dependence of HBT at STAR.* J.Phys., G38:124148, 2011, [arXiv: 1107.1527].

[Appe99] Appelshauser, H. et al.: *Baryon stopping and charged particle distributions in central Pb + Pb collisions at 158-GeV per nucleon.* Phys. Rev. Lett., 82:2471–2475, 1999, [arXiv: nucl-ex/9810014].

[Arle03] Arleo, Francois: *Quenching of hadron spectra in DIS on nuclear targets.* Eur.Phys.J., C30:213–221, 2003, [arXiv: hep-ph/0306235].

[Arme00] Armesto, N. and C. Pajares: *Central rapidity densities of charged particles at RHIC and LHC.* Int.J.Mod.Phys., A15:2019–2052, 2000, [arXiv: hep-ph/0002163].

[Arna06] Arnaldi, R. et al.: *First measurement of the rho spectral function in high- energy nuclear collisions.* Phys. Rev. Lett., 96:162302, 2006, [arXiv: nucl-ex/0605007].

[Arni83] Arnison, G. et al.: *CHARGED PARTICLE MULTIPLICITY DISTRIBUTIONS IN PROTON ANTI-PROTON COLLISIONS AT 540-GeV CENTER-OF-MASS ENERGY.* Phys.Lett., B123:108, 1983.

[Arse05] Arsene, I. et al.: *Quark Gluon Plasma an Color Glass Condensate at RHIC? The perspective from the BRAHMS experiment.* Nucl. Phys., A757:1–27, 2005, [arXiv: nucl-ex/0410020].

[Back01] Back, B.B. et al.: *Baryon rapidity loss in relativistic Au+Au collisions.* Phys.Rev.Lett., 86:1970–1973, 2001, [arXiv: nucl-ex/0003007].

[Back03a] Back, B.B. et al.: *Comparison of the total charged particle multiplicity in high-energy heavy ion collisions with e+ e- and p p / anti-p p data.* 2003, [arXiv: nucl-ex/0301017].

[Back03b] Back, B.B. et al.: *The Significance of the fragmentation region in ultrarelativistic heavy ion collisions.* Phys.Rev.Lett., 91:052303, 2003, [arXiv: nucl-ex/0210015].

[Back05] Back, B. B. et al.: *The PHOBOS perspective on discoveries at RHIC.* Nucl. Phys., A757:28–101, 2005, [arXiv: nucl-ex/0410022].

[Back06a] Back, B.B. et al.: *Centrality and energy dependence of charged-particle multiplicities in heavy ion collisions in the context of elementary reactions.* Phys.Rev., C74:021902, 2006.

[Back06b] Back, B.B. et al.: *Charged-particle pseudorapidity distributions in Au+Au collisions at $s(NN)^{1/2}$ = 62.4-GeV.* Phys.Rev., C74:021901, 2006, [arXiv: nucl-ex/0509034].

[Back06c] Back, B.B. et al.: *Transverse momentum and rapidity dependence of HBT correlations in Au + Au collisions at s(NN)**(1/2) = 62.4-GeV and 200-GeV.* Phys.Rev., C73:031901, 2006, [arXiv: nucl-ex/0409001].

[Baie08] Baier, Rudolf, Paul Romatschke, Dam Thanh Son, Andrei O. Starinets and Mikhail A. Stephanov: *Relativistic viscous hydrodynamics, conformal invariance, and holography.* JHEP, 0804:100, 2008, [arXiv: 0712.2451].

[Balt08] Baltz, A.J. et al.: *The Physics of Ultraperipheral Collisions at the LHC.* Phys.Rept., 458:1–171, 2008, [arXiv: 0706.3356].

[Bass98] Bass, S. A. et al.: *Microscopic models for ultrarelativistic heavy ion collisions.* Prog. Part. Nucl. Phys., 41:255–369, 1998, [arXiv: nucl-th/9803035].

[Bass09] Bass, Steffen A. et al.: *Systematic Comparison of Jet Energy-Loss Schemes in a realistic hydrodynamic medium.* Phys.Rev., C79:024901, 2009, [arXiv: 0808.0908].

[Bear02] Bearden, I.G. et al.: *Pseudorapidity distributions of charged particles from Au+Au collisions at the maximum RHIC energy.* Phys.Rev.Lett., 88:202301, 2002, [arXiv: nucl-ex/0112001].

[Bear04] Bearden, I.G. et al.: *Nuclear stopping in Au + Au collisions at s(NN)**(1/2) = 200-GeV.* Phys.Rev.Lett., 93:102301, 2004, [arXiv: nucl-ex/0312023].

[Beca02] Becattini, F. and G. Passaleva: *Statistical hadronisation model and transverse momentum spectra of hadrons in high energy collisions.* Eur. Phys. J., C23:551–583, 2002, [arXiv: hep-ph/0110312].

[Beri12] Beringer, J. and others: *Review of Particle Physics (RPP).* Phys.Rev., D86:010001, 2012.

[Bert88] Bertsch, G., M. Gong and M. Tohyama: *Pion Interferometry in Ultrarelativistic Heavy Ion Collisions.* Phys.Rev., C37:1896–1900, 1988.

[Bert89] Bertsch, G.F.: *PION INTERFEROMETRY AS A PROBE OF THE PLASMA.* Nucl.Phys., A498:173C–180C, 1989.

[Bial76] Biallas, A., M. Bleszynski and W. Czyz: *Multiplicity distributions in nucleus-nucleus collisions at high energies.* Nuclear Physics B, 111(3):461 – 476, 1976.

[Bial99] Bialas, A.: *Fluctuations of string tension and transverse mass distribution.* Phys.Lett., B466:301–304, 1999, [arXiv: hep-ph/9909417].

[Bjor83] Bjorken, J.D.: *Highly Relativistic Nucleus-Nucleus Collisions: The Central Rapidity Region.* Phys.Rev., D27:140–151, 1983.

[Blei99] Bleicher, M. et al.: *Relativistic hadron hadron collisions in the ultrarelativistic quantum molecular dynamics model.* J. Phys., G25:1859–1896, 1999, [arXiv: hep-ph/9909407].

[Blei05] Bleicher, M: *Ultra-Relativistic hh, hA and AA interactions.* Lecture Notes, 2005.

[Blei11] Bleicher, Marcus: *The Low energy frontier: What is exciting about physics below the top RHIC energy.* 2011, [arXiv: 1107.3482].

[Blum07] Blume, C.: *Centrality and energy dependence of proton, light fragment and hyperon production.* J.Phys., G34:S951–954, 2007, [arXiv: nucl-ex/0701042].

[Brac00] Brachmann, J. et al.: *Antiflow of nucleons at the softest point of the EoS.* Phys.Rev., C61:024909, 2000, [arXiv: nucl-th/9908010].

[Brau95] Braun-Munzinger, P., J. Stachel, J. P. Wessels and N. Xu: *Thermal equilibration and expansion in nucleus-nucleus collisions at the AGS.* Phys. Lett., B344:43–48, 1995, [arXiv: nucl-th/9410026].

[Brow97] Brown, David A. and Pawel Danielewicz: *Imaging of sources in heavy ion reactions.* Phys.Lett., B398:252–258, 1997, [arXiv: nucl-th/9701010].

[Brow98] Brown, David A. and Pawel Danielewicz: *Optimized discretization of sources imaged in heavy ion reactions.* Phys.Rev., C57:2474–2483, 1998, [arXiv: nucl-th/9712066].

[Brow07] Brown, D.A., R. Soltz, J. Newby and A. Kisiel: *Exploring Lifetime Effects in Femtoscopy.* Phys.Rev., C76:044906, 2007, [arXiv: 0705.1337].

[Buss12] Buss, O., T. Gaitanos, K. Gallmeister, H. van Hees, M. Kaskulov and others: *Transport-theoretical Description of Nuclear Reactions.* Phys.Rept., 512:1–124, 2012, [arXiv: 1106.1344].

[Cain09] Caines, Helen: *The RHIC Beam Energy Scan: STAR'S Perspective.* pages 375–378, 2009, [arXiv: 0906.0305].

[Cass04] Cassing, W., K. Gallmeister and C. Greiner: *Suppression of high transverse momentum hadrons at RHIC by prehadronic final state interactions.* Nucl.Phys., A735:277–299, 2004, [arXiv: hep-ph/0311358].

[Cass08] Cassing, W. and E.L. Bratkovskaya: *Parton transport and hadronization from the dynamical quasiparticle point of view.* Phys.Rev., C78:034919, 2008, [arXiv: 0808.0022].

[Cass09] Cassing, W.: *From Kadanoff-Baym dynamics to off-shell parton transport.* Eur.Phys.J.ST, 168:3–87, 2009, [arXiv: 0808.0715].

[Chaj08] Chajecki, Zbigniew and Mike Lisa: *Global Conservation Laws and Femtoscopy of Small Systems.* Phys.Rev., C78:064903, 2008, [arXiv: 0803.0022].

[Cley99] Cleymans, J. and K. Redlich: *Chemical and thermal freeze-out parameters from 1-A-GeV to 200-A-GeV.* Phys. Rev., C60:054908, 1999, [arXiv: nucl-th/9903063].

[Cole05] Cole, B.A. et al.: *Differential probes of medium-induced energy loss.* Eur.Phys.J., C43:271–280, 2005.

[Coop74] Cooper, Fred and Graham Frye: *Comment on the Single Particle Distribution in the Hydrodynamic and Statistical Thermodynamic Models of Multiparticle Production.* Phys.Rev., D10:186, 1974.

[Cser99] Csernai, L.P. and D. Rohrich: *Third flow component as QGP signal.* Phys.Lett., B458:454, 1999, [arXiv: nucl-th/9908034].

[Cser11] Csernai, L.P., V.K. Magas, H. Stocker and D.D. Strottman: *Fluid Dynamical Prediction of Changed v1-flow at LHC.* Phys.Rev., C84:024914, 2011, [arXiv: 1101.3451].

[Csor90] Csorgo, T., J. Zimanyi, J. Bondorf, H. Heiselberg and S. Pratt: *TWO PION CORRELATION FROM SPACER.* Phys.Lett., B241:301–307, 1990.

[Eheh96] Ehehalt, W. and W. Cassing: *Relativistic transport approach for nucleus nucleus collisions from SIS to SPS energies.* Nucl. Phys., A602:449–486, 1996.

[Elli03] Elliott, J. B. et al.: *Constructing the phase diagram of finite neutral nuclear matter.* Phys. Rev., C67:024609, 2003, [arXiv: nucl-ex/0205004].

[Falt04] Falter, T., W. Cassing, K. Gallmeister and U. Mosel: *Hadron attenuation in deep inelastic lepton-nucleus scattering.* Phys.Rev., C70:054609, 2004, [arXiv: nucl-th/0406023].

[Fili96] Filip, Peter: *Azimuthally sensitive HBT analysis.* 1996, [arXiv: hep-ex/9609001].

[Frod06] Frodermann, Evan, Ulrich Heinz and Michael Annan Lisa: *Fitted HBT radii versus space-time variances in flow-dominated models.* Phys.Rev., C73:044908, 2006, [arXiv: nucl-th/0602023].

[Frod07] Frodermann, Evan, Rupa Chatterjee and Ulrich Heinz: *Evolution of pion HBT radii from RHIC to LHC: Predictions from ideal hydrodynamics.* J.Phys., G34:2249–2254, 2007, [arXiv: 0707.1898].

[Gall08] Gallmeister, K. and U. Mosel: *Time Dependent Hadronization via HERMES and EMC Data Consistency.* Nucl.Phys., A801:68–79, 2008, [arXiv: nucl-th/0701064].

[Gazd11] Gazdzicki, Marek, Mark Gorenstein and Peter Seyboth: *Onset of deconfinement in nucleus-nucleus collisions: Review for pedestrians and experts.* Acta Phys.Polon., B42:307–351, 2011, [arXiv: 1006.1765].

[Geli10] Gelis, Francois, Edmond Iancu, Jamal Jalilian-Marian and Raju Venugopalan: *The Color Glass Condensate.* Ann.Rev.Nucl.Part.Sci., 60:463–489, 2010, [arXiv: 1002.0333].

[Gian04] Gianotti, F.: *Physics at the LHC.* Phys.Rept., 403:379–399, 2004.

[Gold59] Goldhaber, Gerson, William B. Fowler, Sulamith Goldhaber and T.F. Hoang: *Pion-pion correlations in antiproton annihilation events.* Phys.Rev.Lett., 3:181–183, 1959.

[Gold60] Goldhaber, Gerson, Sulamith Goldhaber, Won-Yong Lee and Abraham Pais: *Influence of Bose-Einstein statistics on the anti-proton proton annihilation process.* Phys.Rev., 120:300–312, 1960.

[Grae12a] Graef, Gunnar, Marcus Bleicher and Qingfeng Li: *Examination of scaling of Hanbury-Brown–Twiss radii with charged particle multiplicity.* Phys.Rev., C85:044901, 2012, [arXiv: 1203.4071].

[Grae12b] Graef, Gunnar, Qingfeng Li and Marcus Bleicher: *Formation time dependence of femtoscopic $\pi\pi$ correlations in p+p collisions at $\sqrt{s_{NN}}$=7 TeV.* J.Phys., G39:065101, 2012, [arXiv: 1203.4421].

[Grae13] Graef, Gunnar, Mike Lisa and Marcus Bleicher: *A twisted emission geometry in non-central Pb+Pb collisions measurable via azimuthally sensitive HBT.* 2013, [arXiv: 1302.3408].

[Gyul94] Gyulassy, Miklos and Xin-Nian Wang: *HIJING 1.0: A Monte Carlo program for parton and particle production in high-energy hadronic and nuclear collisions.* Comput.Phys.Commun., 83:307, 1994, [arXiv: nucl-th/9502021].

[Hall07] Hallo, Ludovic, Antoine Bourgeade, Vladimir T. Tikhonchuk, Candice Mezel and Jérome Breil: *Model and numerical simulations of the propagation and absorption of a short laser pulse in a transparent dielectric material: Blast-wave launch and cavity formation.* Phys. Rev. B, 76:024101, Jul 2007.

[Hama88] Hama, Yogiro and Sandra S. Padula: *BOSE-EINSTEIN CORRELATION OF PARTICLES PRODUCED BY EXPANDING SOURCES.* Phys.Rev., D37:3237, 1988.

[Hama05] Hama, Yogiro, T. Kodama and Jr. Socolowski, O.: *Topics on hydrodynamic model of nucleus nucleus collisions.* Braz. J. Phys., 35:24–51, 2005, [arXiv: hep-ph/0407264].

[Hanb54] Hanbury Brown, R. and R.Q. Twiss: *A New type of interferometer for use in radio astronomy.* Phil.Mag., 45:663–682, 1954.

[Hanb56a] Hanbury Brown, R. and R.Q. Twiss: *A Test of a new type of stellar interferometer on Sirius.* Nature, 178:1046–1048, 1956.

[Hanb56b] Hanbury Brown, R. and R.Q. Twiss: *Correlation between photons in two coherent beams of light.* Nature, 177(4497):27–29, 1956.

[Harr97] Harr, R. et al.: *Pseudorapidity distribution of charged particles in $\bar{p}p$ collisions at $\sqrt{s}$ = 630-GeV.* Phys.Lett., B401:176–180, 1997, [arXiv: hep-ex/9703002].

[Hein02a] Heinz, Ulrich W., A. Hummel, M.A. Lisa and U.A. Wiedemann: *Symmetry constraints for the emission angle dependence of HBT radii.* Phys.Rev., C66:044903, 2002, [arXiv: nucl-th/0207003].

[Hein02b] Heinz, Ulrich W. and Peter F. Kolb: *Emission angle dependent pion interferometry at RHIC and beyond.* Phys.Lett., B542:216–222, 2002, [arXiv: hep-ph/0206278].

[Hein02c] Heinz, Ulrich W. and Peter F. Kolb: *Two RHIC puzzles: Early thermalization and the HBT problem.* 2002, [arXiv: hep-ph/0204061].

[Heis99a] Heiselberg, Henning: *Emission times and opacities from interferometry in noncentral relativistic nuclear collisions.* Phys.Rev.Lett., 82:2052–2055, 1999, [arXiv: nucl-th/9809077].

[Heis99b] Heiselberg, Henning and Anne-Marie Levy: *Elliptic flow and HBT in noncentral nuclear collisions.* Phys.Rev., C59:2716–2727, 1999, [arXiv: nucl-th/9812034].

[Hira02] Hirano, Tetsufumi: *Is early thermalization achieved only near midrapidity in Au + Au collisions at sNN =130 GeV?* Phys. Rev., C65:011901, 2002, [arXiv: nucl-th/0108004].

[Hira06] Hirano, Tetsufumi, Ulrich W. Heinz, Dmitri Kharzeev, Roy Lacey and Yasushi Nara: *Hadronic dissipative effects on elliptic flow in ultrarelativistic heavy-ion collisions.* Phys.Lett., B636:299–304, 2006, [arXiv: nucl-th/0511046].

[Huma10] Humanic, Thomas J.: *Predictions of hadronic observables in Pb+Pb collisions at $\sqrt{s}_{NN} = 2.76$ TeV from a hadronic rescattering model.* 2010, [arXiv: 1011.0378].

[Juod06] Juodkazis, S., K. Nishimura, S. Tanaka, H. Misawa, E. G. Gamaly, B. Luther-Davies, L. Hallo, P. Nicolai and V. T. Tikhonchuk: *Laser-Induced Microexplosion Confined in the Bulk of a Sapphire Crystal: Evidence of Multimegabar Pressures.* Phys. Rev. Lett., 96:166101, Apr 2006.

[Karp11] Karpenko, Yu.A. and Yu.M. Sinyukov: *Femtoscopic scales in central A+A collisions at RHIC and LHC energies in hydrokinetic model.* J.Phys., G38:124059, 2011, [arXiv: 1107.3745].

[Khar01] Kharzeev, Dmitri and Marzia Nardi: *Hadron production in nuclear collisions at RHIC and high density QCD.* Phys.Lett., B507:121–128, 2001, [arXiv: nucl-th/0012025].

[Kisi06] Kisiel, Adam, Tomasz Taluc, Wojciech Broniowski and Wojciech Florkowski: *THERMINATOR: Thermal heavy-ion generator.* Comput. Phys. Commun., 174:669–687, 2006, [arXiv: nucl-th/0504047].

[Koda01] Kodama, T., C. E. Aguiar, T. Osada and Yogiro Hama: *Entropy-based relativistic smoothed particle hydrodynamics.* J. Phys., G27:557–560, 2001.

[Kolb00] Kolb, Peter F., Josef Sollfrank and Ulrich W. Heinz: *Anisotropic transverse flow and the quark hadron phase transition.* Phys.Rev., C62:054909, 2000, [arXiv: hep-ph/0006129].

[Kolb01] Kolb, P.F., Ulrich W. Heinz, P. Huovinen, K.J. Eskola and Kimmo Tuominen: *Centrality dependence of multiplicity, transverse energy, and elliptic flow from hydrodynamics.* Nucl.Phys., A696:197–215, 2001, [arXiv: hep-ph/0103234].

[Kolb03] Kolb, Peter F. and Ulrich W. Heinz: *Hydrodynamic description of ultrarelativistic heavy-ion collisions.* 2003, [arXiv: nucl-th/0305084].

[Kope07] Kopeliovich, B.Z., J. Nemchik and Ivan Schmidt: *Time Evolution of Jets and Perturbative Color Neutralization.* Nucl.Phys., A782:224–233, 2007, [arXiv: hep-ph/0608044].

[Land53] Landau, L.D.: *On the multiparticle production in high-energy collisions.* Izv.Akad.Nauk Ser.Fiz., 17:51–64, 1953.

[Land96] Landau, L.D. and E.M. Lifshitz: *Lehrbuch der theoretischen Physik V: Statistische Physik.* Akademie-Verlag Berlin, 1996.

[Li08] Li, Qingfeng, Marcus Bleicher and Horst Stocker: *The Effect of pre-formed hadron potentials on the dynamics of heavy ion collisions and the HBT puzzle.* Phys.Lett., B659:525–530, 2008, [arXiv: 0709.1409].

[Li09a] Li, Qing-feng, Jan Steinheimer, Hannah Petersen, Marcus Bleicher and Horst Stocker: *Effects of a phase transition on HBT correlations in an integrated Boltzmann+Hydrodynamics approach.* Phys.Lett., B674:111–116, 2009, [arXiv: 0812.0375].

[Li09b] Li, Qingfeng and Marcus Bleicher: *A Model comparison of resonance lifetime modifications, a soft equation of state and non-Gaussian effects on pi-pi correlations at FAIR/AGS energies.* J.Phys., G36:015111, 2009, [arXiv: 0808.3457].

[Li12] Li, Qingfeng, G. Graf and Marcus Bleicher: *UrQMD calculations of two-pion HBT correlations in central Pb-Pb collisions at $\sqrt{s_{NN}} = 2.76$ TeV.* Phys.Rev., C85:034908, 2012, [arXiv: 1203.4104].

[Lin02] Lin, Zi-wei, C. M. Ko and Subrata Pal: *Partonic effects on pion interferometry at RHIC.* Phys. Rev. Lett., 89:152301, 2002, [arXiv: nucl-th/0204054].

[Lin05] Lin, Zi-Wei, Che Ming Ko, Bao-An Li, Bin Zhang and Subrata Pal: *A Multi-phase transport model for relativistic heavy ion collisions.* Phys.Rev., C72:064901, 2005, [arXiv: nucl-th/0411110].

[Lind04] Lindl, John D., Peter Amendt, Richard L. Berger, S. Gail Glendinning, Siegfried H. Glenzer, Steven W. Haan, Robert L. Kauffman, Otto L. Landen and Laurence J. Suter: *The physics basis for ignition using indirect-drive targets on the National Ignition Facility.* Physics of Plasmas, 11(2):339–491, 2004.

[Lisa95] Lisa, M.A. et al.: *Radial flow in Au + Au collisions at E = 0.25-A/GeV - 1.15-A/Gev.* Phys.Rev.Lett., 75:2662–2665, 1995, [arXiv: nucl-ex/9502001].

[Lisa00a] Lisa, M.A. et al.: *Azimuthal dependence of pion interferometry at the AGS.* Phys.Lett., B496:1–8, 2000, [arXiv: nucl-ex/0007022].

[Lisa00b] Lisa, M.A. et al.: *Bombarding energy dependence of pi-minus interferometry at the Brookhaven AGS.* Phys.Rev.Lett., 84:2798–2802, 2000.

[Lisa00c] Lisa, Michael Annan, Ulrich W. Heinz and Urs Achim Wiedemann: *Tilted pion sources from azimuthally sensitive HBT interferometry.* Phys.Lett., B489:287–292, 2000, [arXiv: nucl-th/0003022].

[Lisa04] Lisa, Michael Annan: *Azimuthally sensitive interferometry and the source lifetime at RHIC.* Acta Phys.Polon., B35:37–46, 2004, [arXiv: nucl-ex/0312012].

[Lisa05] Lisa, Michael Annan, Scott Pratt, Ron Soltz and Urs Wiedemann: *Femtoscopy in relativistic heavy ion collisions.* Ann.Rev.Nucl.Part.Sci., 55:357–402, 2005, [arXiv: nucl-ex/0505014].

[Lisa11] Lisa, M.A. et al.: *Shape analysis of strongly-interacting systems: The Heavy ion case.* New J.Phys., 13:065006, 2011, [arXiv: 1104.5267].

[Liu00] Liu, H. et al: *Sideward flow in Au + Au collisions between 2-A-GeV and 8-A-GeV.* Phys.Rev.Lett., 84:5488–5492, 2000, [arXiv: nucl-ex/0005005].

[Liu11a] Liu, Fu-Ming and Klaus Werner: *Direct photons at low transverse momentum: A QGP signal in pp collisions at LHC.* Phys.Rev.Lett., 106:242301, 2011, [arXiv: 1102.1052].

[Liu11b] Liu, Fu-Ming and Klaus Werner: *On QGP Formation in pp Collisions at 7 TeV.* J.Phys., G38:124183, 2011, [arXiv: 1106.5909].

[Luzu08] Luzum, Matthew and Paul Romatschke: *Conformal Relativistic Viscous Hydrodynamics: Applications to RHIC results at s(NN)**(1/2) = 200-GeV.* Phys.Rev., C78:034915, 2008, [arXiv: 0804.4015].

[Maju07] Majumder, A.: *Resolving the plasma profile via differential single inclusive suppression.* Phys.Rev., C75:021901, 2007, [arXiv: nucl-th/0608043].

[Makh88] Makhlin, A.N. and Yu.M. Sinyukov: *Hydrodynamics of Hadron Matter Under Pion Interferometric Microscope.* Z.Phys., C39:69, 1988.

[Manl92] Manley, D.M. and E.M. Saleski: *Multichannel resonance parametrization of pi N scattering amplitudes.* Phys.Rev., D45:4002–4033, 1992.

[McMi02] McMillan, Paul F.: *New materials from high-pressure experiments.* Nat. Mater., 1:19–25, 2002.

[Meht09] Mehtar-Tani, Yacine and Georg Wolschin: *Baryon Stopping as a new Probe of Geometric Scaling.* Phys.Rev.Lett., 102:182301, 2009, [arXiv: 0811.1721].

[Meno02] Menotti, C., P. Pedri and S. Stringari: *Expansion of an Interacting Fermi Gas.* Phys.Rev.Lett., 89:250402, 2002.

[Merm09] Mermillod-Blondin, A., J. Bonse, A. Rosenfeld, I. V. Hertel, Yu. P. Meshcheryakov, N. M. Bulgakova, E. Audouard and R. Stoian: *Dynamics of femtosecond laser induced voidlike structures in fused silica.* Applied Physics Letters, 94(4):041911, 2009.

[Mitr09] Mitrovski, Michael, Tim Schuster, Gunnar Graf, Hannah Petersen and Marcus Bleicher: *Charged particle (pseudo-) rapidity distributions in $p^+\bar{p}$ / p^+p and Pb+Pb/Au+Au collisions from SPS to LHC energies from UrQMD.* Phys.Rev., C79:044901, 2009, [arXiv: 0812.2041].

[Moha11] Mohanty, Bedangadas: *STAR experiment results from the beam energy scan program at RHIC.* J.Phys., G38:124023, 2011, [arXiv: 1106.5902].

[Moun11] Mount, E., G. Graef, M. Mitrovski, M. Bleicher and M.A. Lisa: *Correspondence between HBT radii and the emission zone in non-central heavy ion collisions.* Phys.Rev., C84:014908, 2011, [arXiv: 1012.5941].

[Mrow98] Mrowczynski, Stanislaw: *Hadronic matter compressibility from event by event analysis of heavy ion collisions.* Phys.Lett., B430:9–14, 1998, [arXiv: nucl-th/9712030].

[Nils87] Nilsson-Almqvist, Bo and Evert Stenlund: *Interactions Between Hadrons and Nuclei: The Lund Monte Carlo, Fritiof Version 1.6.* Comput.Phys.Commun., 43:387, 1987.

[Nori04] Norieaga, Merceds. L.: *Pion Interferometry in Au + Au Collisions at a Center of Mass Energy per Nucleon of 200 GeV.* PhD Thesis, 2004.

[OHar02] O'Hara, K.M., S.L. Hemmer, M.E. Gehm, S.R. Granade and J.E. Thomas: *Observation of a Strongly Interacting Degenerate Fermi Gas of Atoms.* Science, 298:2179–2182, 2002, [arXiv: cond-mat/0212463].

[Olli92] Ollitrault, Jean-Yves: *Anisotropy as a signature of transverse collective flow.* Phys.Rev., D46:229–245, 1992.

[Paec03] Paech, K., Horst Stoecker and A. Dumitru: *Hydrodynamics near a chiral critical point.* Phys. Rev., C68:044907, 2003, [arXiv: nucl-th/0302013].

[Pani00] Panitkin, Sergei Y. and David A. Brown: *Imaging proton sources with space momentum correlations.* Phys.Rev., C61:021901, 2000, [arXiv: nucl-th/9906022].

[Pete08a] Petersen, Hannah, Marcus Bleicher, Steffen A. Bass and Horst Stocker: *UrQMD-2.3 - Changes and Comparisons.* 2008, [arXiv: 0805.0567].

[Pete08b] Petersen, Hannah, Jan Steinheimer, Gerhard Burau, Marcus Bleicher and Horst Stocker: *A Fully Integrated Transport Approach to Heavy Ion Reactions with an Intermediate Hydrodynamic Stage.* Phys.Rev., C78:044901, 2008, [arXiv: 0806.1695].

[Pete11] Petersen, Hannah: *Identified Particle Spectra and Anisotropic Flow in an Event-by-Event Hybrid Approach in Pb+Pb collisions at* $\sqrt{s_{\mathrm{NN}}} = 2.76$ *TeV.* Phys.Rev., C84:034912, 2011, [arXiv: 1105.1766].

[Pink99] Pinkenburg, C. et al.: *Elliptic flow: Transition from out-of-plane to in-plane emission in Au + Au collisions.* Phys. Rev. Lett., 83:1295–1298, 1999, [arXiv: nucl-ex/9903010].

[Prat84] Pratt, S.: *Pion Interferometry for Exploding Sources.* Phys.Rev.Lett., 53:1219–1221, 1984.

[Prat86] Pratt, S.: *Pion Interferometry of Quark-Gluon Plasma.* Phys.Rev., D33:1314–1327, 1986.

[Prat93] Pratt, S.: *Pion lasers from high-energy collisions.* Phys.Lett., B301:159–164, 1993.

[Prat94] Pratt, S. et al: *Testing transport theories with correlation measurements.* Nucl.Phys., A566:103C–114C, 1994.

[Prat09a] Pratt, Scott: *The Long Slow Death of the HBT Puzzle.* Acta Phys.Polon., B40:1249–1256, 2009, [arXiv: 0812.4714].

[Prat09b] Pratt, Scott: *The Long Slow Death of the HBT Puzzle.* Nucl.Phys., A830:51C–57C, 2009, [arXiv: 0907.1094].

[Reti04] Retiere, Fabrice and Michael Annan Lisa: *Observable implications of geometrical and dynamical aspects of freeze out in heavy ion collisions.* Phys.Rev., C70:044907, 2004, [arXiv: nucl-th/0312024].

[Risc95a] Rischke, Dirk H., Stefan Bernard and Joachim A. Maruhn: *Relativistic hydrodynamics for heavy ion collisions. 1. General aspects and expansion into vacuum.* Nucl. Phys., A595:346–382, 1995, [arXiv: nucl-th/9504018].

[Risc95b] Rischke, Dirk H., Yaris Pursun and Joachim A. Maruhn: *Relativistic hydrodynamics for heavy ion collisions. 2. Compression of nuclear matter and the phase transition to the quark - gluon plasma.* Nucl. Phys., A595:383–408, 1995, [arXiv: nucl-th/9504021].

[Risc96] Rischke, Dirk H. and Miklos Gyulassy: *The Time delay signature of quark - gluon plasma formation in relativistic nuclear collisions.* Nucl.Phys., A608:479–512, 1996, [arXiv: nucl-th/9606039].

[Ryu12] Ryu, Sangwook, Sangyong Jeon, Charles Gale, Bjoern Schenke and Clint Young: *MUSIC with the UrQMD Afterburner.* 2012, [arXiv: 1210.4588].

[Sark06] Sarkisyan, Edward K.G. and Alexander S. Sakharov: *Multihadron production features in different reactions.* AIP Conf.Proc., 828:35–41, 2006, [arXiv: hep-ph/0510191].

[Sche10] Schenke, Bjoern, Sangyong Jeon and Charles Gale: *(3+1)D hydrodynamic simulation of relativistic heavy-ion collisions.* Phys.Rev., C82:014903, 2010, [arXiv: 1004.1408].

[Sche11] Schenke, Bjorn, Sangyong Jeon and Charles Gale: *Elliptic and triangular flow in event-by-event (3+1)D viscous hydrodynamics.* Phys.Rev.Lett., 106:042301, 2011, [arXiv: 1009.3244].

[Schm12] Schmah, Alexander: *Highlights of the Beam Energy Scan from STAR.* Central Eur.J.Phys., 10:1238–1241, 2012, [arXiv: 1202.2389].

[Schw51] Schwinger, Julian S.: *On gauge invariance and vacuum polarization.* Phys.Rev., 82:664–679, 1951.

[Seng93] Senger, P. et al.: *The KAON spectrometer at SIS.* Nucl. Instrum. Meth., A327:393–411, 1993.

[Shur80] Shuryak, Edward V.: *Quantum Chromodynamics and the Theory of Superdense Matter.* Phys.Rept., 61:71–158, 1980.

[Shur04] Shuryak, Edward V. and Ismail Zahed: *Rethinking the properties of the quark gluon plasma at T approximately T(c).* Phys.Rev., C70:021901, 2004, [arXiv: hep-ph/0307267].

[Siny89] Sinyukov, Yu.M.: *HANBURY BROWN/TWISS CORRELATIONS FOR EXPANDING HADRON AND QUARK - GLUON MATTER.* Nucl.Phys., A498:151C–160C, 1989.

[Siny11] Sinyukov, Yu.M. and Iu.A. Karpenko: *Hydrokinetic predictions for femtoscopy scales in A+A collisions in the light of recent ALICE LHC results.* Phys.Part.Nucl.Lett., 8:896–902, 2011, [arXiv: 1103.5632].

[Sjos06] Sjostrand, Torbjorn, Stephen Mrenna and Peter Z. Skands: *PYTHIA 6.4 Physics and Manual.* JHEP, 0605:026, 2006, [arXiv: hep-ph/0603175].

[Sjos08] Sjostrand, Torbjorn, Stephen Mrenna and Peter Z. Skands: *A Brief Introduction to PYTHIA 8.1.* Comput.Phys.Commun., 178:852–867, 2008, [arXiv: 0710.3820].

[Soff01] Soff, Sven, Steffen A. Bass and Adrian Dumitru: *Pion interferometry at RHIC: Probing a thermalized quark gluon plasma?* Phys.Rev.Lett., 86:3981–3984, 2001, [arXiv: nucl-th/0012085].

[Soff03] Soff, Sven, Steffen A. Bass, David H. Hardtke and Sergey Y. Panitkin: *Particle correlations at RHIC: Scrutiny of a puzzle.* Nucl.Phys., A715:801–804, 2003, [arXiv: nucl-th/0209055].

[Song08] Song, Huichao and Ulrich W. Heinz: *Suppression of elliptic flow in a minimally viscous quark-gluon plasma.* Phys.Lett., B658:279–283, 2008, [arXiv: 0709.0742].

[Song11] Song, Huichao, Steffen A. Bass, Ulrich Heinz, Tetsufumi Hirano and Chun Shen: *200 A GeV Au+Au collisions serve a nearly perfect quark-gluon liquid.* Phys.Rev.Lett., 106:192301, 2011, [arXiv: 1011.2783].

[Sorg95] Sorge, H.: *Flavor production in Pb (160-A/GeV) on Pb collisions: Effect of color ropes and hadronic rescattering.* Phys.Rev., C52:3291–3314, 1995, [arXiv: nucl-th/9509007].

[Spie99] Spieles, C. et al.: *Dissociation of expanding c anti-c states in heavy ion collisions.* Phys.Lett., B458:137–142, 1999.

[Stei08] Steinheimer, J. et al.: *(3+1)-dimensional hydrodynamic expansion with a critical point from realistic initial conditions.* Phys.Rev., C77:034901, 2008, [arXiv: 0710.0332].

[Stei11a] Steinheimer, J. and M. Bleicher: *Core-corona separation in the UrQMD hybrid model.* Phys.Rev., C84:024905, 2011, [arXiv: 1104.3981].

[Stei11b] Steinheimer, J., S. Schramm and H. Stocker: *An Effective chiral Hadron-Quark Equation of State.* J.Phys., G38:035001, 2011, [arXiv: 1009.5239].

[Step04] Stephanov, Mikhail A.: *QCD phase diagram and the critical point.* Prog.Theor.Phys.Suppl., 153:139–156, 2004, [arXiv: hep-ph/0402115].

[Stoc99] Stock, Reinhard: *Quark Matter 99 summary: Hadronic signals.* Nucl.Phys., A661:282–299, 1999, [arXiv: hep-ph/9911408].

[Stoe80] Stoecker, Horst, J. A. Maruhn and W. Greiner: *Collective sideward flow of nuclear matter in violent high-energy heavy ion collisions.* Phys. Rev. Lett., 44:725, 1980.

[Tann06] Tannenbaum, M.J.: *Recent results in relativistic heavy ion collisions: From 'a new state of matter' to 'the perfect fluid'.* Rept.Prog.Phys., 69:2005–2060, 2006, [arXiv: nucl-ex/0603003].

[Torr05] Torrieri, Giorgio et al.: *SHARE: Statistical hadronization with resonances.* Comput. Phys. Commun., 167:229–251, 2005, [arXiv: nucl-th/0404083].

[True12] Truesdale, D. and T.J. Humanic: *Predictions from a simple hadron rescattering model for p p collisions at the LHC.* J.Phys., G39:015011, 2012.

[UrQM09] UrQMD-Collaboration: *The UrQMD user guide.* 2009, [http://urqmd.org].

[Vide95] Videbaek, F. and O. Hansen: *Baryon rapidity loss and mid-rapidity stacking in high-energy nucleus-nucleus collisions.* Phys.Rev., C52:2684–2693, 1995.

[Voge11] Vogel, Sascha, Pol Bernard Gossiaux, Klaus Werner and Joerg Aichelin: *Heavy Quark Energy Loss in High Multiplicity Proton Proton Collisions at LHC.* Phys.Rev.Lett., 107:032302, 2011, [arXiv: 1012.0764].

[Volo96] Voloshin, S.A. and W.E. Cleland: *Anisotropic transverse flow and the HBT correlation function.* Phys.Rev., C54:3212–3217, 1996, [arXiv: nucl-th/9606033].

[Volo08] Voloshin, Sergei A., Arthur M. Poskanzer and Raimond Snellings: *Collective phenomena in non-central nuclear collisions.* 2008, [arXiv: 0809.2949].

[Weig06] Weiglein, G. et al.: *Physics interplay of the LHC and the ILC.* Phys.Rept., 426:47–358, 2006, [arXiv: hep-ph/0410364].

[Well02] Wells, Randall C: *Azimuthal Dependence of Pion Interferometry in Au+Au Collisions at a Center of Mass Energy of 130AGeV.* 2002, [http://www.scientificcommons.org/8670056].

[Wern06] Werner, Klaus, Fu-Ming Liu and Tanguy Pierog: *Parton ladder splitting and the rapidity dependence of transverse momentum spectra in deuteron-gold collisions at RHIC.* Phys.Rev., C74:044902, 2006, [arXiv: hep-ph/0506232].

[Wern07] Werner, Klaus: *Core-corona separation in ultra-relativistic heavy ion collisions.* Phys.Rev.Lett., 98:152301, 2007, [arXiv: 0704.1270].

[Wern11a] Werner, K., Iu. Karpenko, T. Pierog, M. Bleicher and K. Mikhailov: *Evidence for hydrodynamic evolution in proton-proton scattering at 900 GeV.* Phys.Rev., C83:044915, 2011, [arXiv: 1010.0400].

[Wern11b] Werner, K., K. Mikhailov, Iu. Karpenko and T. Pierog: *Bose-Einstein Correlations in a Fluid Dynamical Scenario for Proton-Proton Scattering at 7 TeV.* 2011, [arXiv: 1104.2405].

[Wied98] Wiedemann, Urs Achim: *Two particle interferometry for noncentral heavy ion collisions.* Phys.Rev., C57:266–279, 1998, [arXiv: nucl-th/9707046].

[Wied99] Wiedemann, Urs Achim and Ulrich W. Heinz: *Particle interferometry for relativistic heavy ion collisions.* Phys.Rept., 319:145–230, 1999, [arXiv: nucl-th/9901094].

[Xu05] Xu, Zhe and Carsten Greiner: *Thermalization of gluons in ultrarelativistic heavy ion collisions by including three-body interactions in a parton cascade.* Phys. Rev., C71:064901, 2005, [arXiv: hep-ph/0406278].

[Zhan98] Zhang, Bin: *ZPC 1.0.1: A Parton cascade for ultrarelativistic heavy ion collisions.* Comput.Phys.Commun., 109:193–206, 1998, [arXiv: nucl-th/9709009].

[Zsch02] Zschiesche, D., S. Schramm, J. Schaffner-Bielich, Horst Stoecker and W. Greiner: *Particle ratios at RHIC: Effective hadron masses and chemical freezeout.* Phys.Lett., B547:7–14, 2002, [arXiv: nucl-th/0209022].

C. Zusammenfassung

In dieser Arbeit wird das theoretische Modell Ultrarelativistische Quanten-Molekulardynamik (UrQMD) verwendet, um Hanbury-Brown-Twiss Korrelationen in Schwerionenkollisionen zu beschreiben.

Alle für die moderne Teilchenphysik relevanten Teilchen und Wechselwirkungen werden durch das Standardmodell beschrieben. Das Standardmodell umfasst 6 Quarks und 6 Leptonen sowie ihre Antiteilchen. Diese sind in drei Familien eingeteilt, die aus nahezu identischen Teilchen, jedoch mit signifikant unterschiedlichen Massen bestehen. Außerdem umfasst das Modell die Austauschbosonen, nämlich Photonen, Gluonen, Z- und W-Bosonen. Das letzte Teilchen ist das Higgs-Boson, dass anderen Teilchen ihre Masse verleiht. Die Austauschbosonen des Standardmodells beschreiben zwei der drei fundamentalen Naturkräfte. Die dritte Kraft, die Gravitation, wird nicht im Rahmen des Standardmodells beschrieben. Sie ist allerdings so schwach, dass sie für die Teilchenphysik nur in sehr exotischen Prozessen wichtig ist.

Die elektroschwache Wechselwirkung und die Gravitation sind theoretisch recht gut beschrieben und fast alle Gleichungen sind mindestens störungstheoretisch lösbar. Die starke Wechselwirkung wird durch Gluonen vermittelt und durch die Quanten-Chromo-Dynamik (QCD) beschrieben. Die Ladung der QCD sind die Farbladungen. Leider sind die Gleichungen der QCD nur in wenigen Ausnahmefällen lösbar. Das hat zwei Gründe. Zum einen die Selbstwechselwirkung der Gluonen, die beliebig komplizierte Wechselwirkungen denkbar macht, zum anderen die große Kopplungskonstante, die dafür sorgt, dass diese komplizierten Prozesse nicht vernachlässigt werden können und störungstheoretisch kaum bis gar nicht beschreibbar sind.

Experimentell ist die QCD nur schwer zugänglich, da es in der QCD das Phänomen des Farbeinschlusses gibt. Farbeinschluss bedeutet, dass zum Trennen von farbgeladenen Teilchen so viel Energie benötigt wird, dass neue Teilchen entstehen, bevor die farbgeladenen Teilchen weiter als ungefähr 1 fm voneinander getrennt werden können. Im Zusammenspiel mit der Ladungserhaltung, die auch für Farbladungen gilt, führt dies dazu, dass auf makroskopischen Skalen nur farbneutrale Objekte vorkommen.

Um die QCD trotzdem experimentell zu erforschen, werden riesige Beschleunigeranlagen gebaut. In diesen werden Protonen und, für die Erforschung der QCD interessanter, Schwerionen auf relativistische Energien beschleunigt und zur Kollision gebracht. Dabei soll ein heißes und dichtes Medium entstehen, das Quark-Gluon-Plasma (QGP), in dem sich Quarks und Gluonen frei bewegen können. Problematisch ist nur, dass diese Kollisio-

nen auf einer Zeitskala von 10^{-23}s und in einem Bereich in der Größenordnung 10^{-15}m stattfinden. Dies verhindert jede direkte Messung. Nur die wiederum farbneutralen Fragmente der Kollision können in den Detektoren der Experimente gemessen werden, wenn die Kollision schon lange vorbei ist.

Alle Messungen, die im Detektor durchgeführt werden können, fallen in drei Kategorien: Ladungsmessung, Impulsmessung und Zählung. Mindestens ebenso interessant ist allerdings die zeitliche und räumliche Dynamik. Diese kann zwar nicht direkt gemessen werden, ist allerdings mittels Hanbury-Brown-Twiss (HBT)-Interferometrie/Korrelationen indirekt zugänglich. Auch mit Hilfe von HBT ist es jedoch nicht eindeutig möglich, Raum- und Zeit- Komponenten der Dynamik zu trennen. Dies ist nur Modell abhängig möglich.

Der Fokus dieser Arbeit liegt darauf, mit UrQMD HBT-Korrelationen in Schwerionenkollisionen zu erforschen.
In Kapitel 2 wird zuerst eine kurze Übersicht über die gängigen Modelle zur Beschreibung der Schwerionen-Daten gegeben. Dabei werden als konzeptuell unterschiedliche Modelle das Thermische Modell, das Druckwellen Modell (im Feld besser bekannt als "Blast Wave Model"), hydrodynamische Modelle und mikroskopische Modelle vorgestellt. Im Falle der mikroskopischen Modelle werden die wichtigsten Eigenschaften konkreter Modelle stichpunktartig vorgestellt. Der Schwerpunkt liegt dabei auf dem UrQMD Modell, welches die Grundlage für diese Arbeit bildet und deshalb ausführlicher beschrieben ist. UrQMD ist ein hadronisches, mikroskopisches Transportmodell. Es umfasst alle Resonanzen bis zu einer Masse von 2.3 GeV und ist in der Lage, Proton+Proton-, Kern+Kern- und Kollisionen mit allen anderen im Modell vorhanden Hadronen in einem sehr breiten Energiebereich zu beschreiben. Die elementaren Kollisionen finden entsprechend einer geometrischen Interpretation des Wirkungsquerschnittes statt. Wann immer möglich werden die gemessenen Wirkungsquerschnitte verwendet. Der Großteil der Wirkungsquerschnitte ist allerdings nicht gemessen. In diesem Fall werden die Wirkungsquerschnitte entweder über das Additive Quarkmodell oder detailliertes Gleichgewicht abgeschätzt. Teilchenproduktion findet im Modell durch Resonanzanregung, Resonanzzerfall und Stringfragmentation statt.

Kapitel 3 beschreibt den theoretischen Hintergrund zu HBT-Korrelationen. Die Korrelationsfunktion gibt das Verhältnis von Teilchenverteilungen mit Quantenkorrelationen zu solchen ohne Quantenkorrelationen an. Es werden der experimentelle und der theoretische Weg zur Korrelationsfunktion gezeigt. Experimentell ist es schwierig eine Verteilung ohne Quantenkorrelationen zu erstellen. Dazu werden Teilchen aus unterschiedlichen Kollisionen korreliert oder unterschiedliche Teilchen aus gleichen Kollisionen. Die Vor- und Nachteile beider Techniken werden in dieser Arbeit kurz diskutiert. In der Theorie wiederum ist es kompliziert Verteilungen mit Quantenkorrelationen zu erzeugen. Bislang gibt es keine Simulationen, die in der Lage sind, diese direkt zu berechnen. Deshalb werden diese Näherungsweise im Nachhinein berechnet. Die Interpretationen, der mittlerweile sehr populären Pratt-Bertsch Radien im Out-Side-Long (OSL) System, als Zusammensetzung der räumlichen Ausdehnung von Schwerionen Kollisionen und ihrer

zeitlichen Dauer werden besprochen. Außerdem wird auch auf azimutal sensitive HBT (asHBT) Analysen eingegangen. Diese sind in nicht-zentralen Kollisionen wichtig. Ihre Verbindung zur Exzentrizität und Neigungswinkel zur Strahlachse wird gezeigt. Mathematische Hintergründe hierzu sind in Appendix A zu finden.

Im Ergebnisteil der Arbeit werden zunächst die UrQMD Rapiditätsspektren für verschiedene kollidierende Systeme über einen breiten Energiebereich hinweg mit Daten verglichen. Hierbei zeigt sich, dass UrQMD in der Lage ist, diese grundlegende Observable im gesamten untersuchten Energiebereich zufriedenstellend zu beschreiben. Auf dieser Basis wird UrQMD benutzt um HBT-Korrelationen zu untersuchen.

In Kapitel 5 werden Proton+Proton-Kollisionen bei der LHC-Schwerpunktsenergie von $\sqrt{s} = 7$ TeV untersucht. Die Analyse der Multiplizitätsabhängigkeit der HBT-Radien zeigt, dass diese im Vergleich zu den Daten zu schwach ist. Dies steht mit dem Fehlen einer partonischen Wechselwirkungsphase in UrQMD im Zusammenhang. Dies ist interessant, da bei niedrigeren Energien meist davon ausgegangen wurde, dass Proton+Proton-Kollisionen zu klein sind, damit ein lokal farbgeladenes Medium entstehen kann. Gleichzeitig zeigt sich, dass die Größe der HBT-Radien signifikant von der Hadronen-Formationszeit im Modell abhängt. Die Formationszeit gibt in diesem Modell die Zeit an, die vom Beginn einer hadronischen Kollision, über die Erzeugung der Quarks im Aufbruch der Farbflussröhre, bis zur vollständigen Bildung der neuen Hadronen vergeht. Diese sonst experimentell kaum zugängliche Formationszeit τ_f kann dadurch auf einen Wert von $\tau_f < 0.8$ fm/c abgeschätzt werden.

In Kapitel 6 werden HBT-Korrelationen in zentralen ($\sigma/\sigma_T < 5\%$) Blei+Blei-Kollisionen bei der LHC-Schwerpunktsenergie von $\sqrt{s} = 2.76$ TeV mit UrQMD untersucht. Das Studium der $K_\perp$-Abhängigkeit der HBT-Radien R_O, R_S und R_L zeigt sowohl in den experimentellen Daten, als auch in den theoretischen Ergebnissen eine sehr ähnliche $K_\perp$-Abhängigkeit. Gleichzeitig werden R_O und R_L bei dieser Energie von UrQMD überschätzt, während R_S mit den experimentellen Ergebnissen kompatibel ist. Dies führt dazu, dass auch das Verhältnis von R_O/R_S überschätzt wird, dass von der Lebenszeit abhängt. Weiter Untersuchungen, in denen wir künstlich die Lebenszeit des Mediums reduziert haben zeigten, dass diese Diskrepanz aufgehoben werden kann, wenn die Lebenszeit um einen Faktor von $2-3$ reduziert wird. Wie zu erwarten wird R_L dadurch nicht beeinflusst. Auch dies steht vermutlich mit einer explosiveren Expansion des Mediums in der Realität als in UrQMD in Verbindung, die wiederum auf das Fehlen einer partonischen Wechselwirkungsphase in UrQMD zurückgeführt wird. Dies ist konsistent mit dem, was in Proton+Proton-Kollisionen gefunden wurde.

In Kapitel 7 wird die Skalierung der HBT-Radien mit der Anzahl der geladenen Teilchen pro Rapiditätsintervall $dN_{ch}/d\eta$ untersucht. Dabei werden sowohl die Zentralität und Kernspezies als auch die Schwerpunktsenergie variiert. Da die HBT-Radien die Ausdehnung der Region, die Teilchen emittiert, zum Zeitpunkt der letzten Wechselwirkung beschreiben werden die HBT-Radien mit zunehmendem $dN_{ch}/d\eta$ größer. Würde es auss-

chließlich von der Teilchendichte abhängen wann die Teilchen vom Medium entkoppeln erwartet man, dass die HBT-Radien für alle Energien und Systeme mit $(dN_{ch}/d\eta)^{1/3}$ skalieren. Es wird eine gute Skalierung der Radien mit $(dN_{ch}/d\eta)^{1/3}$ gefunden, solange die Änderung in $(dN_{ch}/d\eta)^{1/3}$ durch eine Änderung der Zentralität oder des Systems verursacht wird. Eine Erhöhung der Schwerpunktsenergie bei gleichem $(dN_{ch}/d\eta)^{1/3}$ führt zu etwas kleineren Radien. Dies liegt daran, dass sich die chemische Zusammensetzung des Systems ändert und, da verschiedene Teilchen auch verschiedene Wirkungsquerschnitte haben, auch der Ausfrierzeitpunkt ändert. Außerdem skalieren die Radien in Kern+Kern-Kollisionen anders als die in Proton+Proton-Stößen. Dies liegt an den unterschiedlichen Emissionsmechanismen (Stringfragmentation versus Resonanzdynamik).

Kapitel 8 beschäftigt sich mit Fluktuationen der HBT-Radien von Kollision zu Kollision. Diese sind am LHC, auf Grund der hohen Multiplizitäten, erstmals messbar. Trotzdem ist die geringe Zahl von Teilchenpaaren weiterhin ein Problem und führt zu einer schlechten Qualität der Korrelationsfunktionen. Deshalb ist es nötig Korrelationsfunktionen, die durch die theoretischen Kurven nicht beschrieben werden können, anhand der Fit Qualität aus zu sortieren. Durch die Messung des Volumens, der Fluktuationen des Volumens und der Temperatur lässt sich die isothermische Kompressibilität κ_T von Kernmaterie bestimmen. Wegen der geringen Statistik pro Kollision sind diese Größen mit signifikanten Unsicherheiten behaftet, was auch im Ergebnis zu großen Unsicherheiten führt. Mit dieser Methode wird κ_T im UrQMD Modell zu $\kappa_T = 1.09 \pm 0.47 \frac{\text{MeV}}{\text{fm}^3}$ in Kollisionen mit Impaktparameter $b = 0$ fm und $\kappa_T = 1.02 \pm 0.51 \frac{\text{MeV}}{\text{fm}^3}$ in Kollisionen mit Impaktparameter $b = 0 - 3.4$ fm bestimmt.

Die letzten drei Kapitel der Arbeit beschäftigen sich mit azimutal sensitivem HBT. In Kapitel 9 werden die Grundlagen erklärt um die Exzentrizität im Endzustand ϵ_f und den Neigungswinkel θ_S der teilchenemittierenden Region mit Hilfe von HBT-Korrelationen zu bestimmen. Bisher wurde dies nur in boostinvarianten Hydrodynamischen Modellen und im Druckwellen Modell, oder im Experiment gemacht. Da die Herleitung der nötigen Formeln von einer Gaußschen Form der Emissionsregion ausgeht war unklar, wie stark sich ein Abweichen von dieser Form auf die Ergebnisse auswirkt. Hierzu werden in Kapitel 9 Gold+Gold Kollisionen bei $\sqrt{s} = 3.84$ & 7.7 GeV in UrQMD berechnet. Die dabei entstehende Ausfriergeometrie unterscheidet sich von einer Gaußverteilung. ϵ_f und θ_S werden sowohl aus der Ausfriergeometrie, als auch aus den HBT-Korrelationen bestimmt. Dabei zeigt sich, dass die HBT Ergebnisse nur um etwa 30% von den tatsächlichen theoretischen Werten abweichen. Die gleichen Abweichungen wurden auch vorher in den Hydrodynamischen und Druckwellen Modellen gefunden. Für die Daten, die bereits gemessen wurden stimmen die UrQMD HBT Ergebnisse mit den experimentellen Ergebnissen überein. Das zeigt, dass die Formeln auch in der hier untersuchten komplexeren Ausfriergeometrie anwendbar sind.

Nachdem im vorhergehenden Kapitel gezeigt wurde, dass die Untersuchung von θ_s und ϵ_f mittels HBT-Korrelationen die Ausfriergeometrie tatsächlich wiedergibt, wird in Kapitel

10 die Energieabhängigkeit von ϵ_f und θ_s erforscht. Die wenigen Datenpunkte zu θ_s werden von UrQMD gut reproduziert. θ_s wird mit steigender Schwerpunktsenergie kleiner und ist über $\sqrt{s_{NN}} = 17$ GeV fast zu vernachlässigen, wird darunter jedoch zunehmend wichtiger. Dies war zu erwarten, da sich die Geometrie bei steigenden Kollisionsenergien immer mehr in die Länge zieht und dadurch immer kleinere Winkel θ_s liefert. Die experimentellen Analysen zur Energieabhängigkeit von θ_s laufen noch. Deshalb wurden bisher leider noch keine experimentellen Daten veröffentlicht um dieses Verhalten nachzuprüfen. Für ϵ_f war zum Zeitpunkt der Studie von RHIC nur ein Datenpunkt vorhanden. Dadurch sah es so aus, als gäbe es ein nicht-monotones Verhalten in der Energieabhängigkeit, das im Rahmen eines einsetzenden Phasenübergangs bei dieser Energie interpretiert werden konnte. Die im Laufe des RHIC-BES gemessenen neuen Datenpunkte liegen sehr gut auf der von UrQMD vorhergesagten Kurve, die jedoch monoton fällt. Damit liegen die neueren RHIC-Messungen im Widerspruch zu dem CERES-Datenpunkt.

Kapitel 11 ist das letzte Kapitel und beschäftigt sich mit einem skalenabhängigen θ_s. In UrQMD-Simulationen nicht-zentraler Kollisionen zeigt sich ein vom Radius in der Reaktionsebene abhängiges θ_s. Eine Parametrisierung von θ_s erlaubt es diese Abhängigkeit in der räumlichen Ausfrierverteilung zu quantifizieren. Hier zeigt sich in der Untersuchung von Blei+Blei Kollisionen bei $E_{lab} = 8$ AGeV und $b = 3.4 - 6.8$ fm, dass θ_s von einem Winkel von fast 100° in der Mitte der Verteilung bis auf einen Winkel von ca. 20° im äußeren Bereich der Verteilung abfällt. Wichtiger ist allerdings, dass es gelingt, die gleiche Abhängigkeit auch im experimentell mittels asHBT messbaren θ_s, in einer Impulsdifferenz aufgelösten Analyse, zu finden. Es wird ausgenutzt, dass Teilchenpaare mit kleiner/großer Impulsdifferenz sensitiv auf große/kleine räumliche Strukturen sind. Um die Herkunft der verdrehten Ausfriergeometrie zu bestimmen wurde im Rahmen des UrQMD Modells die zeitliche Entwicklung der Ausfrierverteilung untersucht. Zu Beginn der Kollision wird die Emission von Teilchen in Richtung der Spektatoren unterdrückt. Es entsteht eine leichte rückwärts Drehung der Ausfriergeometrie in der Reaktionsebene in der Mitte der Kollision. Dieser Effekt wird im Laufe der Kollision immer schwächer, da die Spektatoren die Kollisionszone nach einer Zeit von ungefähr 8 fm weitestgehend verlassen haben. Währenddessen dreht sich die Ausfriergeometrie, den Spektatoren hinterher, was zur Verdrehung der zeitintegrierten Verteilung führt. Gleichzeitig setzt eine bevorzugte Expansion des Mediums entlang der kurzen Achse der nahezu elliptischen Ausfrierverteilung ein. Dieser Effekt sorgt dafür, dass auch in der späten Phase noch Teilchen zum senkrecht zur z-Achse gerichteten Part der Ausfrierverteilung beitragen. Das Messen der Abhängigkeit von θ_s von der Impulsdifferenz der Teilchenpaare erlaubt also einen indirekten Blick auf die Zeitevolution während der Kollision und liefert viele wertvolle Informationen über die auftretenden Wechselwirkungsmechanismen.

In dieser Arbeit wurden die Standard-HBT-Analysen zur Bestimmung der HBT-Radien bei LHC Energien druchgeführt. Diese zeigten, dass das Medium in UrQMD bei diesen Energien, da keine partonische Phase im Modell vorhanden ist, nicht explosiv genug expandiert. Die vielversprechendsten Ergebnisse bei diesen Energien sind die Eingrenzung der Formationszeit auf $\tau_f < 0.8$ fm/c und die simulierte Messung der isothermis-

chen Kompressibilität zu $\kappa_T \approx 1 \frac{\mathrm{MeV}}{\mathrm{fm}^3}$. In den Simulationen nicht-zentraler Kollisionen wurde die Anwendbarkeit der Formel, θ_s mittels HBT zu berechnen, auch für den Fall nicht-Gaußscher Emissionsquellen mit Fluss bestätigt. Auf dieser Grundlage wurde eine Methode entwickelt und getestet, die es erlaubt, θ_s in Abhängigkeit vom Radius experimentell zu messen. Bei FAIR-Energien sollte das gemessene Signal von $\theta_s(r)$ am stärksten sein.